DESIGNING STABLE ROOM-TEMPERATURE METAL-SULFUR BATTERIES

A Dissertation

Presented to the Faculty of the Graduate School

of Cornell University

In Partial Fulfillment of the Requirements for the Degree of

Doctor of Philosophy

by
Shuya Wei
August 2017

DESIGNING STABLE ROOM-TEMPERATURE METAL-SULFUR BATTERIES

Shuya Wei, Ph. D.

Cornell University 2017

High-energy and inexpensive rechargeable battery systems based on earth-abundant materials are important for both mobile and stationary energy storage technologies. Rechargeable metal-sulfur batteries (Li-S or Na-S) that can operate stably at room temperature are among the most sought-after of these platforms because these cells take advantage of a two-electron-redox process to yield high storage capacity from inexpensive electrode materials. Realization of practical metal-sulfur batteries has been fraught with multiple stubborn problems ranging from unstable electrodeposition of metal anodes during battery recharge to rapid loss of the active cathode material by dissolution into the electrolyte. In the studies undertaken in this thesis, I aim to develop design principles for room temperature metal-S batteries that use a metal anode, a carbon-sulfur composite cathode, and a liquid electrolyte containing a functional ionic liquid/polymer as a deposition stabilizer. My work shows that the metal sulfur cells, particularly for sodium-sulfur (Na-S) cells with this configuration can cycle stably for over 100 cycles at 0.5C (1C = 1675 mAh/g) with 600 mAh/g reversible capacity and nearly 100 percent Coulombic efficiency. By means of spectroscopic, electrochemical analyses and in-situ visualization, my work demonstrates that the high stability and reversibility of the cells stem from at least two sources related both to the cathode and anode. First, the functional additives spontaneously form a Na-ion conductive film on the anode or increase the viscosity of the electrolyte without sacrificing its conductivity. This combination of features appears to stabilize deposition of sodium by reducing the electric field near the electrode and eliminate unstable electroconvection. Second, on the cathode side, carbon

materials play a key role that can constrain the electrochemical reaction between sodium ion and sulfur to the solid state, without formation of the intermediate soluble sodium polysulfide species. This combination of the electrolyte and carbon substrate are shown to provide sufficiently strong association of sulfur in the cathode and at the same time stabilize the surface of the highly reactive metal anodes to enable stable long-term cycling of the Na-S electrochemical cells.

BIOGRAPHICAL SKETCH

Shuya Wei received her B.Eng. degree in Bioengineering from Nanyang Technological University, Singapore in 2013. She obtained her Ph.D. in Chemical Engineering from Cornell University in 2017 under the supervision of Professor Lynden A. Archer. Her research focuses on nanoparticle-polymer composite materials design and their applications in electrochemical energy storage technologies. She is also interested in understanding the fundamentals of electrochemical processes in electrodes and at electrode/electrolyte interfaces.

ACKNOWLEDGEMENTS

The author would like to express her deepest gratitude to her advisor, Professor Lynden A. Archer, whose help, continuous suggestions, invaluable teachings and guidance assisted her greatly in the completion of her master's research. The author is grateful to Prof. Archer who was willing to share his research experiences, enlightened the author in this field of research. Throughout the years' project, Prof Archer's understanding, assistance and support had provided her with unconstraint learning opportunities. Moreover, Prof. Archer also ensures that works was going on well and regularly reviewed the author's research progress, enabling the author to complete her project successfully. Under his supervision, the author gained a lot of in-depth knowledge pertaining to this area of research and had decided to pursue research as her career path.

The author would also like to extend her gratefulness to her thesis committee members Professor Yong L. Joo and Professor Jin Suntivich for their assistance, teachings and valuable suggestions.

TABLE OF CONTENTS

1 INTRODUCTION

1.1 BACKGROUND

Among solid-state cathode materials under consideration for rechargeable lithium and sodium batteries, elemental sulfur offers the greatest promise for reversibly storing large amounts of electrical energy at moderate cost. As a cathode, sulfur hosts as many as two lithium (sodium) ions non-topotactically via the following redox reaction: $16Li + S_8 \leftrightarrow 8Li_2S$ ($16Na + S_8 \leftrightarrow 8Na_2S$). This reaction is attractive for electrochemical storage for several reasons. It can be used to reversibly store large amounts of electrical energy – up to 2500Wh/kg or 2800Wh/L in the lithium-sulfur battery systems (about half of the values in the sodium-sulfur battery systems) – a factor of ten or more higher than other electrochemical storage technologies (e.g. Ni-H (80Wh/kg, 120Wh/L), Li-ion (150Wh/kg, 250Wh/L), and Li-ion polymer batteries (180Wh/kg, 300Wh/L)) of contemporary interest (Figure 1) [1-5]. The reaction also occurs spontaneously, is fully reversible, and does not require intervention using catalysts or other means. Finally, the reaction can in principle occur entirely in the solid state and generates lithium (sodium)-sulfur compounds as its only products. This can be contrasted with competing energy storage solutions based on combustion of fossil fuels, which irreversibly generate even larger amounts of energy on a gravimetric or volumetric basis (e.g. commercial coal: 6.7kW·h/kg, and a commercial-grade gasoline: 12kW·h/kg, 9kW·h/L), but with the added burden of managing harmful CO_2 and other gaseous emissions. The low cost of sulfur ($0.02 per g) and its availability in regions all over the world provides an additional incentive for the development of metal-sulfur electrochemical storage technology [6, 7].

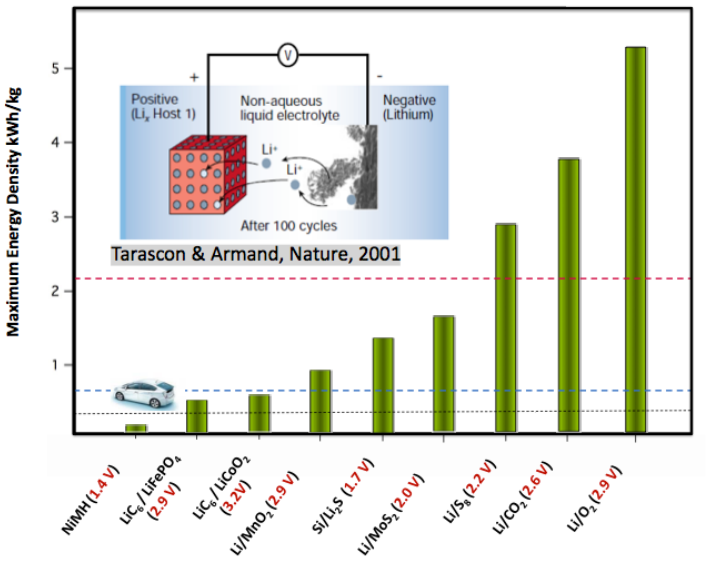

Figure 1: Comparison of the theoretical energy density and discharge voltages of different battery storage platforms. The inset illustrates the challenge with lithium dendrite growth and proliferation that limits adoption of storage technologies to the right of the plow that use metallic lithium as anodes for high overall cell energy densities. The red horizontal line represents the useful energy density of gasoline for transportation (i.e. the energy density of gasoline considering the 18% efficiency of the internal combustion engine). The dashed blue and black lines correspond to the US Advanced battery Consortium (USABC) long-term (2020) and short-term energy density targets, respectively [8].

Despite the considerable advantages offered by Li-S and Na-S storage technologies, commercial development of a practical Li-S or Na-S rechargeable battery has been limited by multiple transport and thermodynamics-related challenges. Despite the significant advances made over the last decade in improving Li-S battery performance, the actual storage delivered by even the best Li-S cells reported in the literature is still quite far away from the theoretical capacity upon which much of the promise of the Li-S battery lies. The best performing Li-S cells rarely deliver storage capacities above 60% of the theoretical value for this chemistry. This situation can be contrasted with the state of affairs in more traditional lithium ion batteries, where cell-level performance approaching 90% of theoretical capacities are common. A Li-S battery that delivers 50% of its theoretical capacity over hundreds of cycles of charge and discharge already offers superior energy

storage to the most energy-dense LIBs on a gravimetric storage basis, but substantially better performance is needed from Li-S cells to compete with LIBs for storage on a volumetric basis. The study carried out by Jie et al.[9] (Figure 2) nicely illustrates this point. The study also underscores the need for Li-S cell designs in which high sulfur loadings in the cathode is achieved. Specifically, at low sulfur loadings, the volumetric energy density for the Li-S battery is noticeably lower than that of commercial lithium ion cells, even if one could realize the theoretical capacity of sulfur. Rechargeable Li-S cells that approach the theoretical capacity of the electrodes at high sulfur loadings are obviously desired.

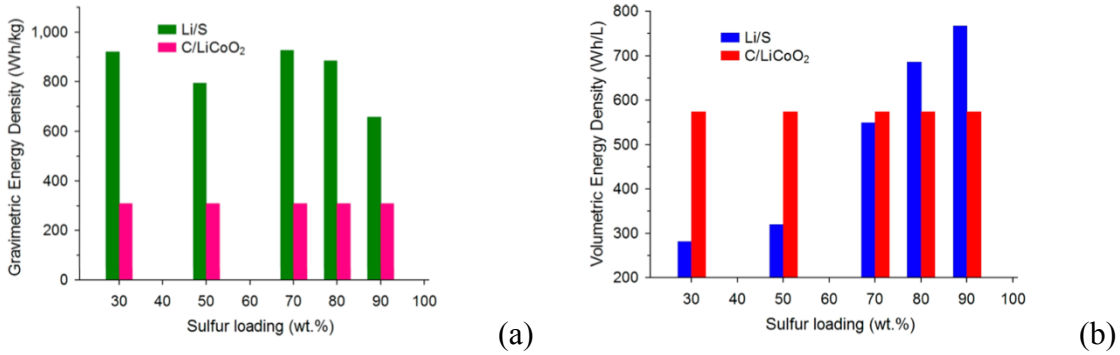

Figure 2: Gravimetric energy densities (a) and Volumetric energy densities (b) of lithium-sulfur cells with different sulfur loading percentages and their comparison to a $LiC_6/LiCoO_2$ cell[9].

In-depth understanding of the working mechanism, transport and other barriers that limit performance of Li-S and Na-S cells are needed for further progress in the field. Such understanding is also essential to guide emerging efforts aimed at rationally designing each of the components in the Li-S cell towards the goal of full materials utilization. Sulfur is infamous for its poor electrical conductivity ($5x10^{-30}$ S/cm at 25°C) and ease with which it is able to form solid allotropes (over 30 are known) [10]. The first of these traits means that a pure sulfur cathode is intrinsically insulating in nature, which limits the utilization of the active electrode material. High-surface area

carbons are typically used as conductive additives within the cathode, but better charge transport in the cell often comes at the expense of storage capacity. Additionally, the volume of sulfur increases by around 80 % (density changes from 2.03 g/cm^3 for sulfur to 1.66 g/cm^3 for Li_2S) when it is fully lithiated and increases by around 140 % when it is fully sodiated. This means that synergistic cathode designs that can accommodate the volume change without compromising electronic connections with conductive additives, which do not expand, are critical for stable, long-term cell performance. A consequence of the second trait is that the preferred redox reaction product, Li_2S, is almost always accompanied by formation of various intermediate polysulfides (LiPS = Li_2S_n, $2 \leq n \leq 8$) products taking a Li-S cell for example (see Figure 3). Depending on the value of *n*, these intermediates can be either insoluble or soluble in the electrolyte, which leads to multiple challenges in managing active materials utilization and reuse. For example, the fully reduced product, Li_2S is insoluble in most electrolytes and is both electronically and ionically insulating. Thus, once Li_2S begins to form in the sulfur cathode, it can only grow by spreading outwards to cover the exposed surface of the conductive carbon particles in the electrode. Ultimately, this growth produces an insulating film on the carbon, which prevents further electronic and ionic access to the active material in the cathode, and the cell discharge voltage drops rapidly (Figure 4). Especially troublesome, are the soluble (Li_2S_n, $2<n<8$) polysulfide discharge products, which establish an internal shuttling pathway between the lithium anode and sulfur cathode that, if unchecked, will continuously consume the active material in both electrodes. Specifically, during the first discharge, the higher order LiPS ($n>2$) dissolve into the electrolyte, depleting sulfur from the cathode. Once in the electrolyte, polysulfides diffuse freely and ultimately reach the metallic lithium anode where they undergo chemical reaction to form lower

order polysulfies, including Li_2S_{n-1} and Li_2S, which may either deposit on the Li anode or diffuse back to the sulfur cathode, where they react with sulfur to reform higher-order polysulfides.

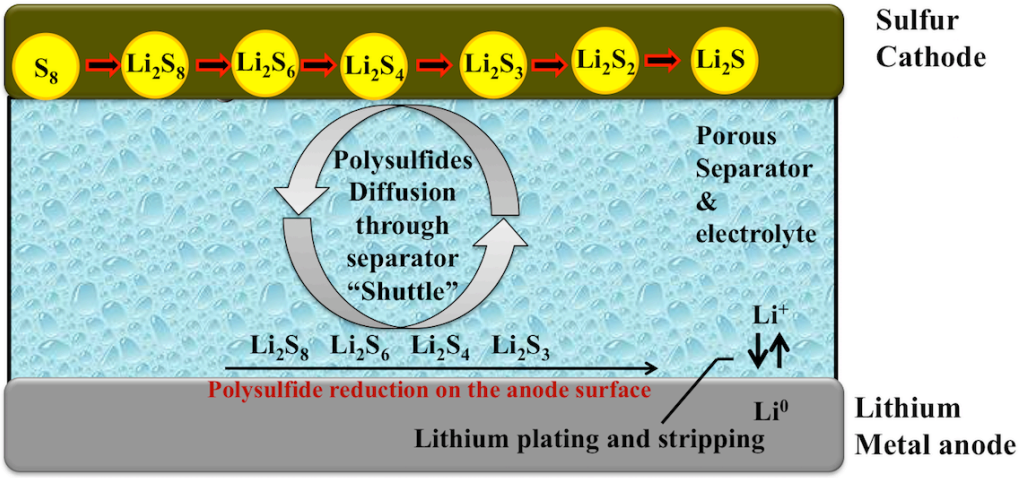

Figure 3: Illustration of polysulfides dissolution and shuttling process in a Li-S battery during the recharge process [11].

The parasitic loop or 'shuttle' illustrated in Figure 3 is free to take place repeatedly and continuously during the cell recharge and not only depletes the active electrode materials, but continuously consumes electrical energy from an external circuit. It is easily visualized by the telltale asymmetry in the discharge and charge profiles (Figure 4a) of a Li-S cell and, lowers the Coulombic efficiency of the cell. Shuttling can also occur during cell storage and leads to self-discharge, which limits the shelf life of Li-S batteries. Sequestering the sulfur in carbon nanocapsules[12-14] is one of a handful of nanomaterials approaches that have been shown to completely remove this asymmetry (Figure 4a), underscoring its fundamental connection to LiPS dissolution. As illustrated in Figure 4b, without any other intervention strategies, this method eliminates the shuttle during the first cycle of charge and discharge for a range of Li-S cell discharge/charge current densities. This example indicates the importance of cathode design for

preventing polysulfide dissolution and induced shuttling, though it is quite difficult to avoid the complexities over long-term cycling because polysulfide dissolution is a thermodynamic process in the soluble electrolyte solvent.

In addition to the intrinsically high storage capacity of sulfur, the high overall energy storage capacity of the Metal-S cell stems from the use of metallic lithium or sodium as the anode. Taking Li-S battery for example, Li is readily ionized in a variety of aprotic liquids and as such provides an efficient complement to sulfur in an electrochemical cell designed to store large amounts of electrical energy. Unfortunately, even at low current densities, Li electrodeposition is sensitive to defects at the electrode surface and is prone to various transport and morphological instabilities[15, 16] that lead to growth and proliferation of rough electrodeposits collectively termed dendrites. Nucleated at the anode, these dendrites may grow as mossy deposits that react with the electrolyte and, if unchecked, will ultimately consume it all, drying out the cell. Dendrites may also grow and proliferate in the inter electrode space, ultimately short-circuiting the cell with potentially catastrophic consequences for safety. A remarkable, though poorly studied feature of the Li-S cell is that it possesses multiple internal safety measures that prevent catastrophic failure by dendrite-induced short circuits. LiPS dissolution and shuttling in the electrolyte provides an intrinsic mechanism for passivating dendrite tips by reaction with LiPS species in the electrolyte. Specifically, the tips concentrate electric field lines and the LiPS flux in the electrolyte, which leads to the reduction of LiPS and deposition of insoluble, insulating Li_2S on the tip surface limiting/eliminating further deposition of Li. This process also provides a high intrinsic overcharge tolerance for Li-S cells. The same process related to both cathode and anode is more severe in Na-

S battery system due to the higher reactivity of sodium metal, though both electrodes are inexpensive and nature abundant.

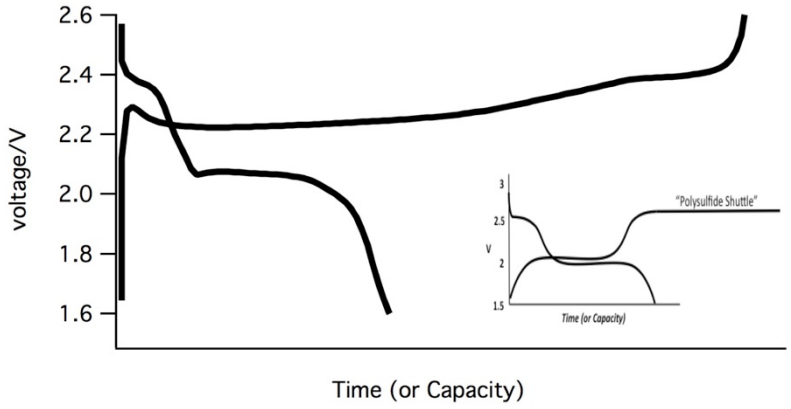

(a)

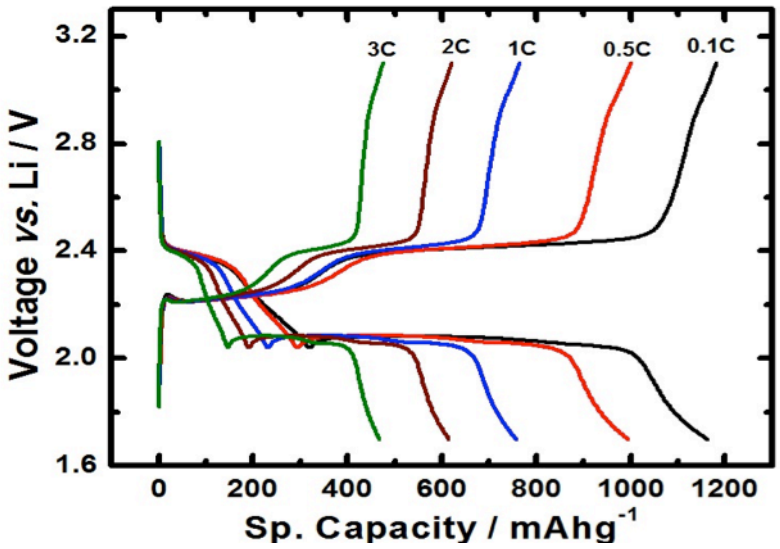

(b)

Figure 4: Discharge and Charge Profiles for Li-S cells: (a) Cell in which LiPS shuttling is dominant; inset is the drawing that shows the idea of 'polysulfide shuttling'; **(**b) Cell in which sulfur is sequestered in carbon nanocapsules in which shuttling is eliminated over a wide range of current densities (0.1 – 3C) [13].

Through systematic application of nanotechnology to each component of the Li-S cell, significant improvements have been achieved in Li-S battery technology during the last decade. Carbon nanoporous materials have been used to address the three most serious shortcomings for the sulfur cathode: poor electrical conductivity of sulfur and sulfides; polysulfide-dissolution induced shuttling; and volume expansion. They can provide shorter pathways for ions and electrons, which helps to solve the problem of poor electrical conductivity of the cathode [4, 5]. The intrinsically high surface-to-volume ratio of nanoporous carbon materials with high affinity for sulfur has also been used to advantage to simultaneously provide kinetic barriers to LiPS loss to the electrolyte and to facilitate electronic transport in the cathode. Well-designed nanostructures can also be used as cathode additives to accommodate volume changes during discharge and charge, stabilizing the cathode to achieve greater performance.

The strong interaction of sulfur with carbon and the synergetic effects the carbon brings in terms of enhancing the conductivity of the cathode has led to an upsurge in interest in cathodes based on sulfur–carbon nanocomposites. The morphology of the carbon–sulfur nanocomposite is now understood to influence everything from the cycling performance; propensity of the cells to self-discharge, and the PS shuttle. Carbonaceous materials with high porosity are widely used as conductive agents and as cathode hosts/matrices to trap the active polysulfide species and increase active material utilization in the cathode during cell operation. In addition, if the carbonaceous materials are engineered to contain sulfur in nanometer sized pores that can better accommodate volume expansion and strain they are expected to stabilize the mechanical properties of the cathode and hence enhance the Li-S cell lifetime. Except for its effect on sulfur sequestration and active material utilization, the pore size also affects other features such as the ease with which electrolyte

can infiltrate the cathode and the rate with which electrons can be transported to/from the active material. Pore size and pore volume of the nanocomposite materials can therefore affect myriad aspects of the Li-S cell performance, including the plateau voltage, active material utilization, rate capability, discharge capacity, and capacity retention.

Porous carbon is classified as microporous (pore diameter less than 2nm), mesoporous (2 to 50 nm) or macroporous (larger than 50 nm). Reports on carbon-sulfur composites with a pore size greater than 10 nm show the typical two-plateau behavior of the sulfur electrode, which is similar to cathode without mesoporous carbon. In contrast, microporous carbon-sulfur composites have a slightly different voltage profile, with one plateau between 1.5 and 1.9 V vs. Li/Li^+ [17-20]which attains most of the discharge capacity. It is likely that sulfur is no longer in the S_8 cyclical structure in these composites; instead, small sulfur is formed due to the constrained pore volume and sulfur and carbon are mixed at the atomic level proposed by Xin et al. from DFT simulation of different sulfur allotropes [20, 21]. Consequently, the corresponding Gibbs free energy of the reaction is different because higher order polyfulfide formation process is excluded in the reaction. However, the state of sulfur inside the microporous carbon has not been clearly investigated by experiment and therefore, the proposed reaction mechanism in the literature still lacks thermodynamic-related supports. Moreover, fundamental electrochemical reaction mechanism for this type of materials and why its voltage profile is different from the elemental sulfur are unclear, though microporous carbon proves to be an effective sulfur immobilizer because it has extremely small pores to constrain sulfur and reaction by strong adsorption, which can prevent the intermediate products polysulfides from outflowing into the electrolyte (Figure. 5)[22].

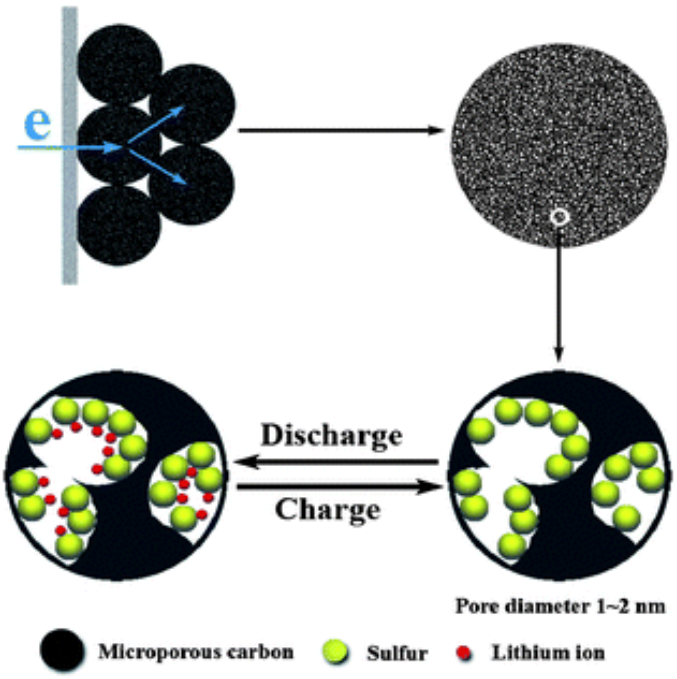

Figure 5. A scheme of the constrained electrochemical reaction process inside the micropores of the sulfur carbon sphere composite cathode[22].

Porous carbons with an increased pore volume can be used to enhance sulfur loading. For this reason, mesoporous materials have been studied extensively as hosts for sulfur[23-26]. The large pore sizes over those of microporous materials allow for easier access to sulfur by liquid electrolytes such that it can facilitate Li ion migration. Thus, lithium sulfur cells with mesoporous carbon-sulfur cathodes show an increase in voltage plateau. Early work in this area was performed by Wang et al. [27, 28], who used an activated carbon with a pore size of around 2.5 nm as the conductive matrix and achieved a reversible capacity of 400 mAh/g. After that, Ji, Lee and Nazar have reported a highly ordered mesoporous carbon-sulfur cathode exhibiting high pore volume, uniform pore diameters and interconnected porous structure by employing a well-known mesoporous carbon material CMK-3, which is synthesized from a mesoporous silica template SBA-15. Their results show that this cathode renders a highly-enhanced performance with

reversible capacities up to 1320 mAh /g. The intake of sulfur within the pores is accomplished by melt diffusion method, where sulfur and CMK-3 carbon mixture are heated together at 155 °C. The CMK-3/sulfur composite electrode was shown to exhibit a high initial discharge capacity of 1005 mAh/g, and it was improved to 1320 mAh/g by linking the carbon surface with polyethylene glycol (PEG) to further trap polysulfides. The highly porous carbon-sulfur composite reported by Lai [29] with 57 wt % sulfur loading delivers the initial high specific capacity up to 1155 mAh/g and a stable capacity of 745 mAh/g after 84 cycles at the current density of 40 mA/g. Based on the analysis of the microstructure and electrochemical performance, they confirmed that the composite could effectively prevent the shuttle behavior of the lithium-sulfur battery. Pore size greater than 50 nm seems to show no effect on preventing polysulfide dissolution due to the weak interaction between sulfur and carbon materials. Other porous material design includes one-dimensional (1-D) carbon nanostructured materials like carbon nanotubes/carbon nanofibers as well as core/shell carbon framework also offer unique features for addressing problems related to the conductivity and active material retention and utilization in a sulfur cathode with several reported works in the literature[30-33].

Carbonized polymers, especially conductive ones, can be tailored or used to modify the surface of cathodes, facilitating ion and charge transport [34]. In addition, they are soft and self-healing so that polymer-sulfur composite can accommodate volumetric expansion during discharge [35]. The studies in polymer-sulfur composites have revealed two general approaches that can enhance the electrochemical performance of polymer-sulfur composites. First, the sulfur size should be small in nanometers to achieve homogeneous interaction between sulfur and polymer. The second approach is based on the belief that simple physical confinement on the electrode surface is not

sufficient for retarding polysulfide dissolution and thus not effective in achieving a long cycle life. Certain atoms such as N, S, O and some functional groups on the polymer can form stronger chemical bonds towards sulfur such that they can better trap intermediate products and thus superior cycling life[28, 36-40]. For examples, Fu et al. [41] have developed a polypyrrole/sulfur composite with the core/shell structure, which displays a high initial capacity of 1050 mAh/g and exhibits a high capacity upon 50 cycles at 835 mA/g. Despite this advantage, it only has 67% capacity retention after 50 cycles. Similar results can be found in other reports with the same-engineered polypyrrole/sulfur composition and structures [26, 36, 41-43]. Xiao et al. [35] have proposed a facile and environmental friendly synthesis process with self-assembling polyaniline nanotubes (PANI-NT) for sulfur encapsulation. This polymer framework offers strong chemical confinement to sulfur-based components, alleviating the loss of active materials greatly. Additionally, the soft polymer matrix and nanostructured sulfur components have provided cushioning for volume changes during electrochemical reactions. Other polymer/sulfur nanocomposites such as PVP-encapsulated hollow S nanospheres [39], poly(pyrrole-co-aniline) (PPyA) copolymer nanofibers[44], core/shell structured polythiophene[37], Sulfur/Poly(acrylonitrile) composite[38], poly(3,4-(ethylenedioxy)thiophene) (PEDOT) /poly(styrenesulfonate) (PSS)-based conductive polymers [40] were also studied extensively by other researchers.

Nanoporous carbon–sulfur composites represent a clever method to improve the performance of the sulfur cathode, as shown in the examples above. The work by Ji and Nazar published in Nature Materials in 2009 has been cited by over 2400 times[45], indicating the broader interest in the realization of room-temperature Li-S or Na-S batteries in practice by using porous carbon-sulfur

nanocomposites. However, none of the above-mentioned methods seem to be able to commercialize the metal-S battery, showing that more efforts including the fundamental understanding of the reaction mechanism or innovative design in the cathode materials are in urgent need. Moreover, none of the above mention method can work properly in a Na-S battery system at room-temperature. Due to the highly reactive nature of sodium and polysulfide, polysulfide once formed in the electrolyte can react with the sodium metal anode internally and immediately, making it unable to recharge. Even though high-temperature Na-S batteries operated at 300 $^{\circ}$C to 350 $^{\circ}$C has been commercialized as stationary energy storage applications. This type of battery has a high-energy density of 760 Wh/kg and high efficiency of charge/discharge (89 % - 92 %) and long cycle life[46]. The battery utilizes a solid electrolyte membrane, beta-alumina solid electrolyte, between the liquid sodium anode and sulfur cathode with good sodium ion conductivity at high temperature. Considering the corrosive nature of sodium polysulfides at high temperature that may fracture the beta-alumina separator and an on-site fire accident of the Na-S plant in Japan, it would be more promising if the Na-S battery can operate stably and safely at room-temperature[47].

Given the tremendous potential of porous materials in metal-S battery applications, it will be highly beneficial if the kinetics associated to ion migration inside the nanoporous materials during the electrochemical reaction can be studied in more detail. It is also equally important to construct optimized porous materials that could eliminate polysulfide formation in both Li-S and Na-S batteries and operate stably at room-temperature.

1.2 OBJECTIVE

Much interest has been aroused in the field of porous carbon materials owing to their beneficial attributes and widespread application in metal-sulfur batteries with some success. However, the polysulfide dissolution is driven by thermodynamic force which is unable to eliminate once formed. The conventional wisdom believes that one must form soluble polysulfides to achieve electrochemical activity. This barrier blocks researchers to discover and investigate the unstable electrodeposition problems related to metal anode in the metal sulfur battery technologies. If sulfur molecular has good contact with a conductive agent like smaller sulfur covalently bonded to conjugated carbons or sulfur infused in extremely small microporous conductive carbon, it perhaps can reduce to solid sulfide species directly without the help of a soluble electrolyte. In such case, one can eliminate polysulfide dissolution and induced shuttling issues completely. The chief objective here is to synthesize carbon-sulfur composites as sulfur cathode materials for the application metal-sulfur batteries that can avoid the formation of soluble polysulfides in the electrolytes and achieve a solid-state reaction. More efforts were devoted to fundamentally and systematically understand the chemistry and electrochemistry of these composites during cell cycling. In addition, unstable electrodeposition associated with metal anodes especially for lithium and sodium were identified and investigated as well. Electrolyte stabilizers like functional ionic liquids and high molecular weight polymers were employed in the electrolyte to stabilize the electrodeposition during the charging process for the metal-sulfur batteries and their working mechanisms were studied as well. The in-situ optical cells were developed to allow the observation of electrodeposition in real time under a light microscope, which greatly helps understand the

dendrite formation mechanism. This objective had been successfully achieved and problems were identified and solved in the following chapters.

The complexity of the metal-sulfur batteries originates from both cathode and anode. On the cathode side, even though various approaches in designing nanoporous carbon materials were devoted as discussed in the previous section to prevent polysulfide dissolution and increase the cycle life of the batteries, the fundamental issue of the polysulfide dissolution in the ether-based electrolytes has never been solved completely. This thermodynamic related process can never be eliminated once involving the salutation based-chemistry for the polysulfides. I want to use an alternative approach that by using a special design of cathode materials, an electrolyte solvent that is non-solvent for polysulfide is compatible with the system to achieve electrochemical activity for the sulfur cathode.

In the following chapters, I investigated the chemistry and reaction mechanism associated with sulfur-polyacrylonitrile (SPAN) nanocomposite cathode in the carbonate-based electrolytes that are non-solvent for polysulfide in both Li-S and Na-S batteries systems. I found that sulfur in the composite exists as S_2 or S_3 that is covalently bonded to carbon backbone that can be reduced to solid sulfide species directly. The conjugation between N and C in the carbon backbone allows fast electron transfer between sulfur and carbon so that sulfides can recombine in the carbon backbone during the recharge process. The solid-state reaction mechanism of the composite was clearly investigated and the origin of the good cyclability were demonstrated in the Chapter 2. To increase sulfur loading in the composite materials and achieve optimal performance in the Na-S batteries at room temperature, I looked for an alternative cathode material, sulfur-microporous carbon composite, with the strongest physical confinement (shown in Chapter 3). I showed that

this material also allow sulfur to be reduced directly to the sulfide species in the solid-state and the combination of the cathode with an electrolyte that is a non-solvent for polysulfide even allow Na-S battery to operate stably at room temperature under a low current density (0.1 C). Though previous works have involved sulfur-microporous carbon composites for metal sulfur battery cathode already[48, 49], the working mechanism and the state of sulfur inside the microporous carbon have not been studied yet. It is important to understand the state of sulfur inside the microporous carbon to correctly interpret the electrochemical reactions. I took efforts in understanding the sulfur species existing inside the microspore by using spectroscopy and the principle reaction mechanism by looking at reaction products and ion diffusivity during the electrochemical reaction process. More careful investigation was taken for the recharge process of the Na-S battery at a higher current density (0.5 C). A noisy charging plateau indicates unstable electrodeposition/dendrite formation was discovered, requesting solutions for stabilizing the electrodeposition for the metal-sulfur batteries.

Dendrite formation and uncontrolled interfacial reaction for high energy secondary metal anodes (Li, Na, Ma and Al) exist as major hurdles to the commercial application of metal anodes. The problems received various attentions that is comparable or even more than sulfur cathode. However, it seems that in most metal-sulfur battey researches, people tend to ignore the issues related to the metal anodes, probably due to the reason of taking endless efforts to avoid polysulfide dissolution and the interaction between polysulfides and the anode. Since the solid-state reaction mechanism in the designed sulfur cathode can eliminate polysulfide dissolution completely in both Li-S and Na-S batteries, I can move forward to look at the anode problems. I employed the ionic liquid 1-methyl-3-propylimidazolium-chlorate tethered to SiO_2 nanoparticles as deposition

stabilizers in the Na-S batteries. Previous works show that the particle can increase cycling life for lithium metal batteries by serving as the supporting electrolytes and providing anions near the electrode surface, I have shown for the first time that the particles form a sodium-ion conductive film on the anode that can protect the reactive metal and stabilize deposition of sodium (Chapter 3).

Since the polysulfie dissolution can be eliminated under the proposed solid-state reaction, I am more interested in stabilizing the charging process. This unstable process is either due to the reactive nature of metal anodes or hydrodynamic-related instable electroconvection in the electrolyte. Both working mechanism were studied by the visualization experiment to fully understand how to stabilize the electrodeposition process. An optical electrochemical cell was build that allow us to visualize the electrodeposition in real time under a light microscope. This contemporary technique allows us to understand the fundamental reaction mechanism deeply. If the unstable electrodeposition is due to the reactive nature the metals, we can protect the metal anode by an ion-rich polymeric membrane which is formed by in situ electropolymerization of functional imidazolium-type ionic liquid monomers (Chapter 4). If the unstable electrodeposition is due to electroconvection at higher current densities that is above diffusion limiting, viscoelastic liquid electrolytes composed of ultrahigh molecular weight polymer solutions can be applied to stabilize electrodeposition of metals. The viscoelastic electrolytes can suppress overlimiting conductance and slow down unstable flow motions in the electrolyte without sacrificing the ion transport properties at the electrode interface. The detailed working mechanism will be discussed in detail in Chapter 5.

1.3 RATIONALE

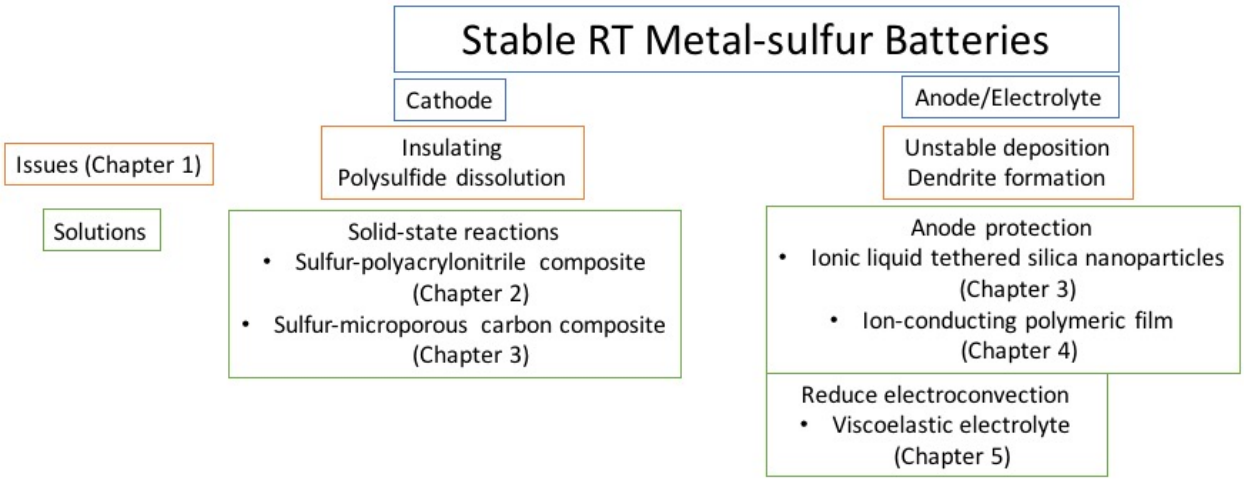

The chart above summarizes the scope of the thesis with the emphasis on designing stable room-temperature metal-sulfur batteries. Starting with the issues facing room-temperature metals sulfur batteries. The author applied an alternative approach to eliminate polysulfide dissolution by employing solid-state reactions. After undercovering the unstable electrodeposition on the anode for the metal-sulfur batteries. More efforts were taken to investigate the problems related to the metal anode. After taking care of all the issues carefully and upstanding the fundamentals behind each problem. The author can design stable room-temperature Li-S and Na-S batteries that can operate with high capacity, coulombic efficiency and long cycle life.

2 METAL-SULFUR BATTERY CATHODES BASED ON PAN-SULFUR COMPOSITES

2.1 INTRODUCTION

Various approaches for sequestering LiPS by affinity particles/molecules/ functional porous carbon nanomaterials in the sulfur cathode have also been studied with varying degrees of success. Graphene oxide[50-52], metal oxides (SiO_2, TiO_2, V_2O_5, Al_2O_3) particles[53-55], nitrogen-doped polymers such as polypyrrole, polyaniline and polyacrylonitrile (PAN) [38, 50, 51, 56, 57] have for instance all been used as additives or protective coating layers, where the high binding energy between LiPS and O, N containing molecules are thought to be beneficial. Guo et al., have provided the most direct evidence in support of this concept by showing that addition of soluble LiPS to stable PAN/dimethylformamide (DMF) solutions lead to rapid gel formation, in which PAN chains swollen by DMF are cross-linked by LiPS[58]. The strong affinity between LiPS and nitrile-containing molecules has also recently been confirmed both by density functional theory and diffusion experiments[58, 59]. An important result from the study by Guo et al. is that sulfur species associated with nitrile groups in the cross-linked polymer solutions remain well dispersed in carbon materials derived from the PAN component, by first removing the DMF solvent and pyrrolizing the PAN in an inert environment. A key conclusion from this study is that when proper attention is given to removing physically adsorbed S_8, a similar process leads to the spontaneous formation of S_2 and S_3 species linked to a conductive, PAN-derived carbon framework.

Sulfurized polymer composites have attracted recent interest as cathode materials for Li-S batteries due to the opportunities they appear to offer for employing both of chemical and physical interaction discussed in previous chapter. In 2002, Wang and co-workers appear to be the first to report that sulfur-polyacrylonitrile (SPAN) composites, which was synthesized by carbonizing a

mixture of sulfur and polyacrylonitrile, possess good-enough charge and ion transport properties to be used as cathodes in rechargeable lithium batteries[50]. Although the composite cathode exhibited good stability in electrochemical cycling studies, no evidence of C-S bonds was observed from FTIR studies, suggesting that sulfur exists mainly in elemental form. Fanous et al. used TOF-SIMS to characterize SPAN composites subjected to different thermal synthesis protocols and report CNS-fragments in the materials treated at elevated temperature[38]. Hwang et al. recently reported that these SPAN composites processed in a fiber morphology exhibit good electrochemical stability when employed as cathodes for sodium-sulfur cells[60]. There have been numerous follow-on type studies of electrochemical properties of this composite, however the electrochemical lithiation and delithiation process are still largely unknown[51, 52, 56, 57, 61-65]. The details of how sulfur interacts with the conductive polymeric host material during charging and discharging are understood to be important, but so far scarcely studied.

1. Ball Milling of PAN and Sulfur;

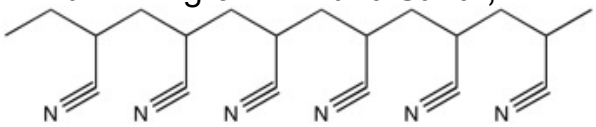

+ S_8

2. Dehydrogenation with S as oxidant and cyclization;

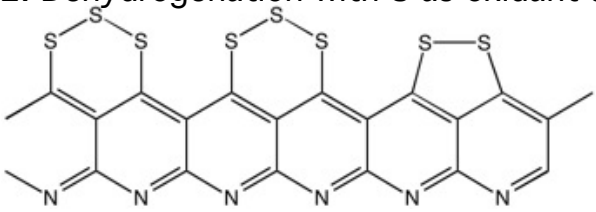

+ H_2S

3. Carbonization to form honeycomb C structure (partial N removal)

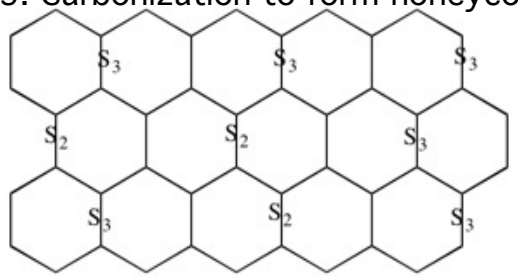

Scheme 1. Proposed synthesis route for creating sulfur-polyacrylonitrile (SPAN) nanocomposite cathode materials.

Herein we report a facile synthesis scheme and on chemistry and electrochemical properties of a family of sulfur/polyacrylonitrile (SPAN) composites that utilize specific interactions with nitrile groups on the polymer backbone and S_8 to destabilize PAN and to promote dehydrogenation and ring formation (Scheme 1). Thermal treatment of the material is shown to lead to metastable, covalently bound sulfur species S_x (x = 2-3) that are integrated throughout the composite. The approach builds on the two most successful strategies – physical confinement and chemical sequestration reported for improving electrochemical activity of sulfur in Li-S cells. Cathodes based on porous carbonaceous materials have, for example, been proposed previously for physically trapping LiPS and improving electronic transport. Of these approaches, microporous carbon materials are thought to provide the strongest physical confinement/immobilization of

sulfur and its reduction products due to extremely small pore sizes. Notably, cyclic voltammetry analysis of cells based on this cathode design have been reported to exhibit an absence of the higher (2.35 V) reduction process associated with formation of high-order LiPS by reaction of Li^+ and S_8, and subsequent loss of LiPS to the electrolyte. This implies that in such cathodes sulfur may exist in other forms than S_8. Xin, for example, has argued in favor of *smaller* S_x (x = 2-4) molecules that upon reduction with Li^+ cannot form soluble high-order LiPS[49]. Although this argument is a reasonable interpretation of the electrochemistry data, support from thermodynamic analysis of the electrode has so far been lacking.

Various approaches for chemically sequestering LiPS, by affinity particles/molecules/functional groups incorporated as additives in the sulfur cathode, have also been studied with differing degrees of success. Graphene oxide[63, 66-70], metal oxides (SiO_2, TiO_2, V_2O_5, Al_2O_3, TiS_2) particles[71], nitrogen-doped polymers such as polypyrrole, polyaniline and polyacrylonitrile (PAN) have for instance all been used as additives or protective coating layers, where the high binding energy between LiPS and O, N containing molecules are thought to be beneficial. Guo et al., have provided the most direct evidence in support of this concept by showing that addition of soluble LiPS to stable PAN/dimethylformamide (DMF) solutions lead to rapid gel formation, in which PAN chains swollen by DMF are cross-linked by LiPS[72]. The strong affinity between LiPS and nitrile-containing molecules has also recently been confirmed both by density functional theory and diffusion experiments. An important result from the study by Guo et al. is that sulfur species associated with nitrile groups in the cross-linked polymer solutions remain well dispersed in carbon materials derived from the PAN component, by first removing the DMF solvent and pyrrolizing the PAN in an inert environment. A key conclusion from this study is that when proper

attention is given to removing physically adsorbed S_8, a similar process leads to the spontaneous formation of S_2 and S_3 species linked to a conductive, PAN-derived carbon framework.

In this work, we report on the thermal synthesis of sulfur/PAN nanocomposites and employ electrochemical and spectroscopic tools to evaluate various hypotheses (Scheme 2) for lithiation and delithiation processes in these materials. Reaction 1 and 2 assume that S-S linkages that covalently bond to organic polymer materials can reversibly cleave and reform by analogous redox chemistry as reported for thiolates (RS^-). It is known that these reactions involve one-electron transfer per sulfur atom, which gives a theoretical specific capacity of 837 mAh/g_S. In Reactions 3 and 4, the R-S bond completely breaks during the lithiation process, resulting in the formation of Li_2S as the only sulfur-containing lithiation product. This reaction involves two-electron transfers per sulfur atom, yielding a theoretical capacity of 1675 mAh/g_S.

Reaction 1:	$RSSR+2Li^+ \leftrightarrow 2RSLi$
Reaction 2:	$RSSSR+4Li^+ \leftrightarrow 2RSLi+Li_2S$
Reaction 3:	$RSSR+4Li^+ \leftrightarrow 2R+2Li_2S$
Reaction 4:	$RSSSR+6Li^+ \leftrightarrow 2R+3Li_2S$

RSSR, RSSSR: Organosulfur-based materials

Scheme 2. Proposed lithiation mechanisms for SPAN nanocomposite.

2.2 RESULTS AND DISCUSSION

The specific synthesis route used in the study is shown in Scheme 1 and detailed in the experimental section. Briefly, to prepare SPAN, a simple one-step procedure involving thermal treatment of physical PAN/sulfur blends at a low temperature ramp rate of 5 ^{o}C/min and under continuous nitrogen gas flow. In the following sections, materials prepared using thermal treatment of the blends at 250, 350, 450 and 600 °C are denoted as SPAN2, SPAN3, SPAN4 and SPAN6, respectively. As a control, PAN without sulfur was heat-treated at 450 °C and denoted as PANC. It is believed that cyclization of the polymer backbone carbons is facilitated by sulfur coordination with and subsequent cleaving of the CN triple bonds. It is further hypothesized that cyclic sulfur (S_8) is in the process cleaved into smaller chain sulfur radicals, which are able to react with and covalently bond to the PAN carbon backbone and dehydrogenate the material to form H_2S. A similar scheme for the dehydrogenation and cyclization of PAN in the presence of sulfur has been reported previously[51, 56, 57, 61, 62, 65]. At high temperature, PAN may further carbonize to produce pyridinic-N carbon ring structures encapsulating sulfur species.

Figure 6a and c report typical STEM images for the as-synthesized SPAN4. The figures indicate that the material exists in a nanosphere morphology with average diameters between 100 nm and 150 nm. To determine the distribution of S, N and C in SPAN4, energy dispersive X-ray (EDX) maps based on the area shown in the annular dark field (ADF) image (Figure 6c) reveals that SPAN4 contains 45.6% sulfur. This composition is higher than previous literature reports, and we attribute it to the low thermal ramp rates used in the pyrolysis step. The sulfur and carbon maps in Figure 1d and e match the result shown in the ADF image (Figure 6c), indicating that carbon and sulfur are homogeneously distributed throughout the materials. The nitrogen map (Figure 6f)

shows that SPAN4 contains 8.59 % N, indicating only partial removal of N atoms during heat treatment. Electron energy loss spectroscopy (EELS) was performed on the composite to investigate the distribution of elements along the line shown in Figure 6a. Figure 6b reports the normalized EELS intensities with respect to position for the S-, C-K, and N-K edges. The results show more sulfur intensity along the middle of the line, indicating that the sulfur is most probably encapsulated by carbon rings.

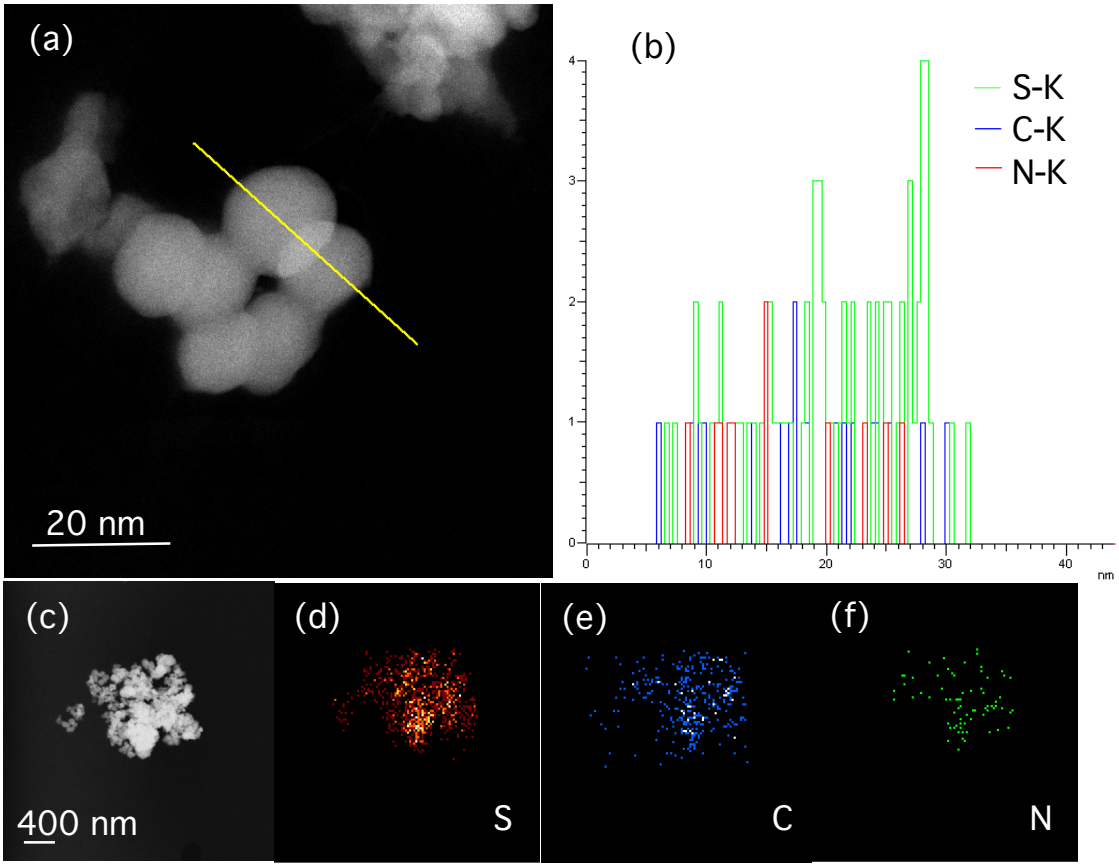

Figure 6: STEM (a and c) images of the SPAN4 composite; EDX sulfur (d), carbon (e) and nitrogen (f) maps based on the area shown in (c); and (b) normalized EELS intensity along the line in (a).

The thermal stability of the various SPAN materials, PANC, and PAN is accessed by thermal gravimetric analysis (TGA) in the temperature range from 25 to 1000 °C (Figure 7). SPAN2

exhibits a significant weight loss of 42 % in the range 200 and 400 °C, which is ascribed to sublimation of unreacted elemental sulfur. For the other SPAN materials, more significant and distinctive weight loss is observed at much higher temperature, beyond 500 °C. It reflects the strong bonding between carbon and sulfur, and is consistent with the higher dissociation energy of the C-S (272 kJ/mol) bond, compared to the S-S bond (251 kJ/mol). XRD analysis (Figure 8) reveal that sulfur in orthorhombic S_8 state only exists in SPAN2, the material synthesized at the lowest temperature; no sulfur peaks can be observed in any of the other SPAN materials, suggesting that the sulfur embedded at higher temperatures loses all crystallinity. A broad diffraction peak at $2\theta = 26.5°$ corresponding to the graphitic (002) plane is also apparent in the SPAN materials, verifying the carbonization of PAN. A signature peak at $2\theta = 17°$, corresponding to the (110) plane of the PAN crystal, completely disappears after carbonization with sulfur. To analyze the chemical structure of the SPANs, Raman (Figure 9) and FTIR (Figure 10) spectra for composites were performed, with PANC, PAN and sulfur as controls. Specific peak assignments are summarized in SI. Based on the information, the structure of the SPAN can be confirmed as turbostratic carbon configuration via dehydrogenation and efficient π-π stacking, and with sulfur covalently bonded to the carbon backbone.

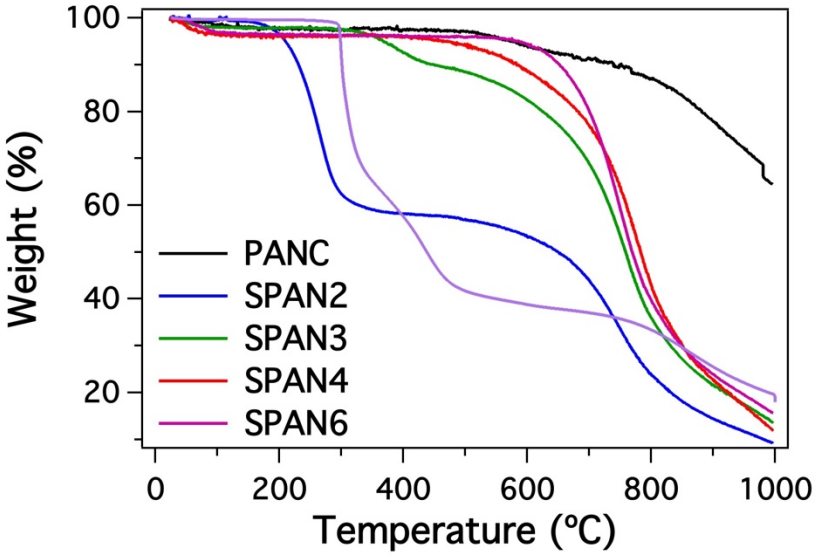

Figure 7: TGA profiles for SPANs, PAN and PANC from 25 to 1000 °C at a rate of 5 °C/min.

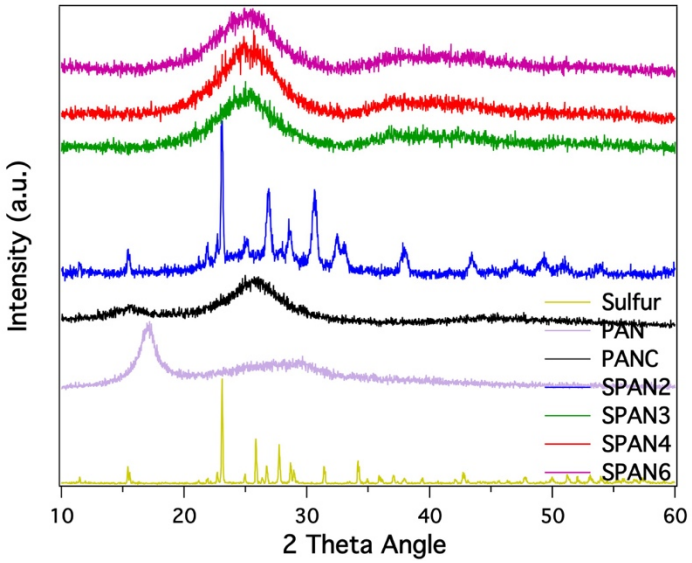

Figure 8: XRD patterns of PANSs, PANC, PAN, and elemental sulfur.

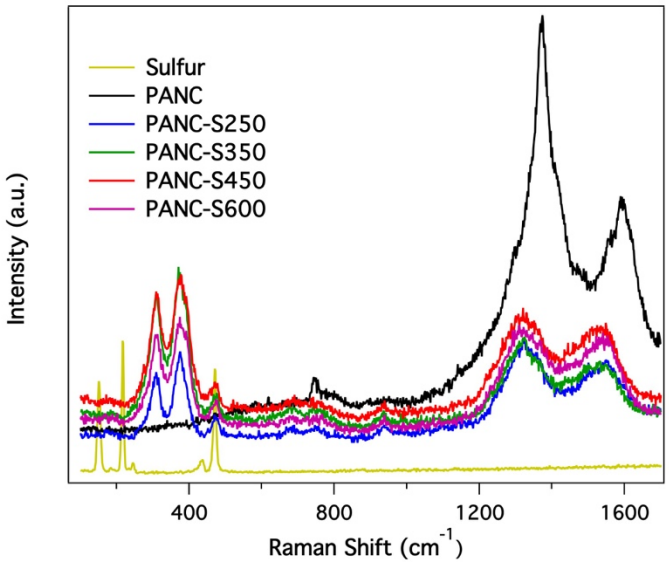

Figure 9: Raman Spectra of PANSs, PANC, and elemental sulfur.

Table 1. Raman shifts (cm^{-1}) and assignments for SPAN and sulfur.

SPAN	Sulfur	Assignments
	150	Characteristic peak of S8
176		C-S
	219	Characteristic peak of S8
298		C-S in plane bending
370		C-S Deformation
	471	Characteristic peak of S8
460		S-S
926		Ring (containing S-S bond) Stretch
1143		Ring (containing S-S bond) Stretch
1360		D Band
1577		G Band

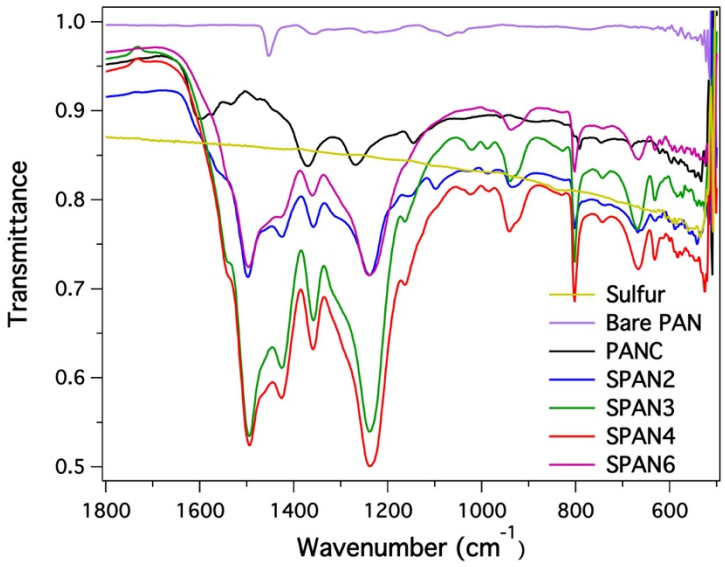

Figure 10: FTIR spectra of SPANs, PANC, PAN and sulfur.

Table 2. FTIR wavenumbers (cm^{-1}) and assignments for SPANs.

SPAN	Assignments
1549	C=C Asymmetric Stretch
1502	C=C Symmetric Stretch
1431	C=N Asymmetric Stretch
1363	C-C Deformation
1250	C=N Symmetric Stretch
943	Ring Breath (Side-chain Containing S-S)
804	Ring Breath (Main-chain Hexahydric-ring)
671	C-S Stretch
513	S-S Stretch

Electrochemical characteristics of the SPAN composites were characterized in 2032 coin cells with

the composite as the active cathode material and lithium foil as the counter electrode. We studied SPAN4 in detail as it exhibited superior electrochemical properties among all the SPAN materials, as well as acceptable sulfur content. To illustrate, the first discharge voltage profile for different SPAN-based cathodes in Figure 11. It is seen that discharge voltage plateau decreases with an increase in the preparation temperature for the SPANs. However, the sulfur content in the materials generally decreases as the temperature increases, thus there is a clear trade-off between sulfur content and binding strength between S and C atoms, with optimal results for both features of the materials found in SPAN4. Two types of electrolytes, 1M $LiPF_6$ in EC/DEC and 1M LiTFSI in DOL/DME with $LiNO_3$ as additive were used in the study to assess the electrodes. This assessment revealed unexpected results that appear critical for understanding the chemistry of the SPAN4 material and the exceptional electrochemical properties of sulfur cathodes based on this material. Figure 12a reports the galvanostatic charge/discharge profile in a cell cycled in the former electrolyte. Comparison of the discharge profiles between the 2^{nd} and 200^{th} cycle reveal negligible changes in both the shape and specific capacity. Figure 12b shows that the material exhibits exceptionally stable cycling stability for over 1000 cycles at 0.4 C (1 C= 1675 mA/g) based on sulfur. The capacity degradation/fade upon repeated cycles of discharge and charge is only 0.027 % per cycle from the 2^{nd} to 1000^{th} cycle. The figure shows that SPAN4 delivers a capacity of over 1000 mAh/g even after 1000 cycles, the highest reported for a Li-S cell cycled at moderate high rate.

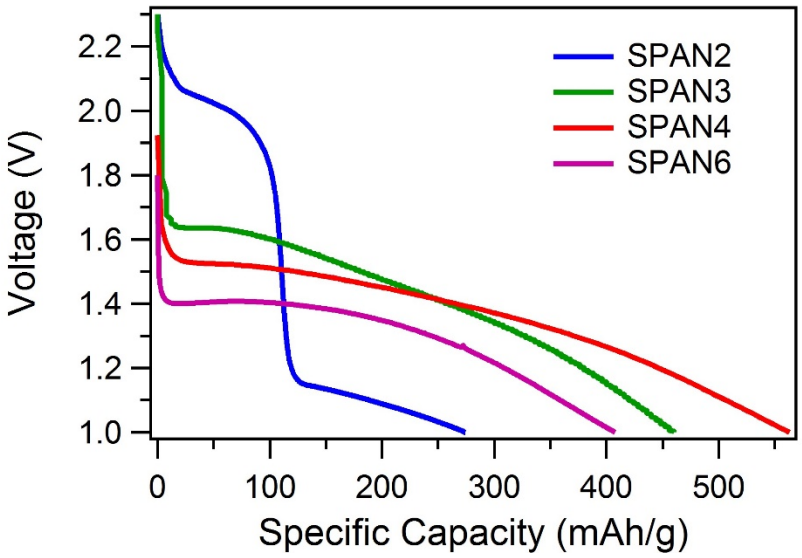

Figure 11: First discharge profiles of different SPANs at 200 mAh/g in 1M $LiPF_6$ in EC/DEC (capacity based on whole cathode weight).

Figure 12a shows that the voltage plateau during the first discharge cycle (~1.5 V) is lower than the values observed in subsequent cycles. This implies that the reduction reaction and transport in the cathode involves different processes, probably cleavage of S-S bonds in the composite, compared to the subsequent cycles. The capacity (1843 mAh/g_{sulfur}) estimated for the initial discharge is higher than the theoretical capacity of sulfur. This means that the π-conjugated pyridinic carbon framework likely makes a contribution, probably a combination of Faradic processes in forming the solid-electrolyte interlayer (SEI) on carbon during the first cycle and a non-Faradic pseudocapacitance that may persist over many cycles. During the following cycles of discharge, the voltage plateau increases and remains stable between 1.6 V and 2.1 V over hundreds of cycles of charge and discharge. This observation is evidently distinct from what is typically found in Li-S cells where a two-step discharge plateau is observed. In the first step at (~2.35 V), the plateau is associated with the reaction of Li^+ and S_8 to form LiPS. The second plateau at (~2.1

V) is attributed to reversible reactions between smaller sulfur species (e.g. LiS_3 and Li_2S_3)[73]. The fact that only the latter of these two voltage plateaus is observed in electrodes based on SPAN4 is significant because it means that in the material sulfur exists in a form that prevents it from achieving its bulk thermodynamically favored form S_8, even when the Li-S cells are in the fully charged state. The result is also significant because it means that LiPS cannot form in these cells, which eliminates complications such as shuttling associated with formation and dissolution of LiPS in the electrolyte. The plausibility of this conclusion will be supported more fully in the sections to follow, however the high coulombic efficiencies evident in Figure 12(b) over extended cycling of the cells, without any of the usual $LiNO_3$ additive in the electrolyte, provides additional proof that shuttling has been arrested in this cathode design. Figures 12c and d report the effect of current density on performance of Li-S cells that utilize a SPAN4 cathode. Current densities from 0.08 mA/cm^2 (=0.2 C) to 0.63 mA/cm^2 (=1.6 C) were investigated. In each cycle, the rates were the same for both charge and discharge. The similarity of the charge and discharge profiles, irrespective of rate, is clearly apparent from the figures. As illustrated in Figure 12d, the SPAN4 cell also shows high capacity retention at different C rates with only an average of 4.13 % capacity decay through high C rate (1.6 C) to low C rate (0.4 C). Importantly, once the C rate is reduced to the original value of 0.2 C, the capacity recovers to its previous steady value.

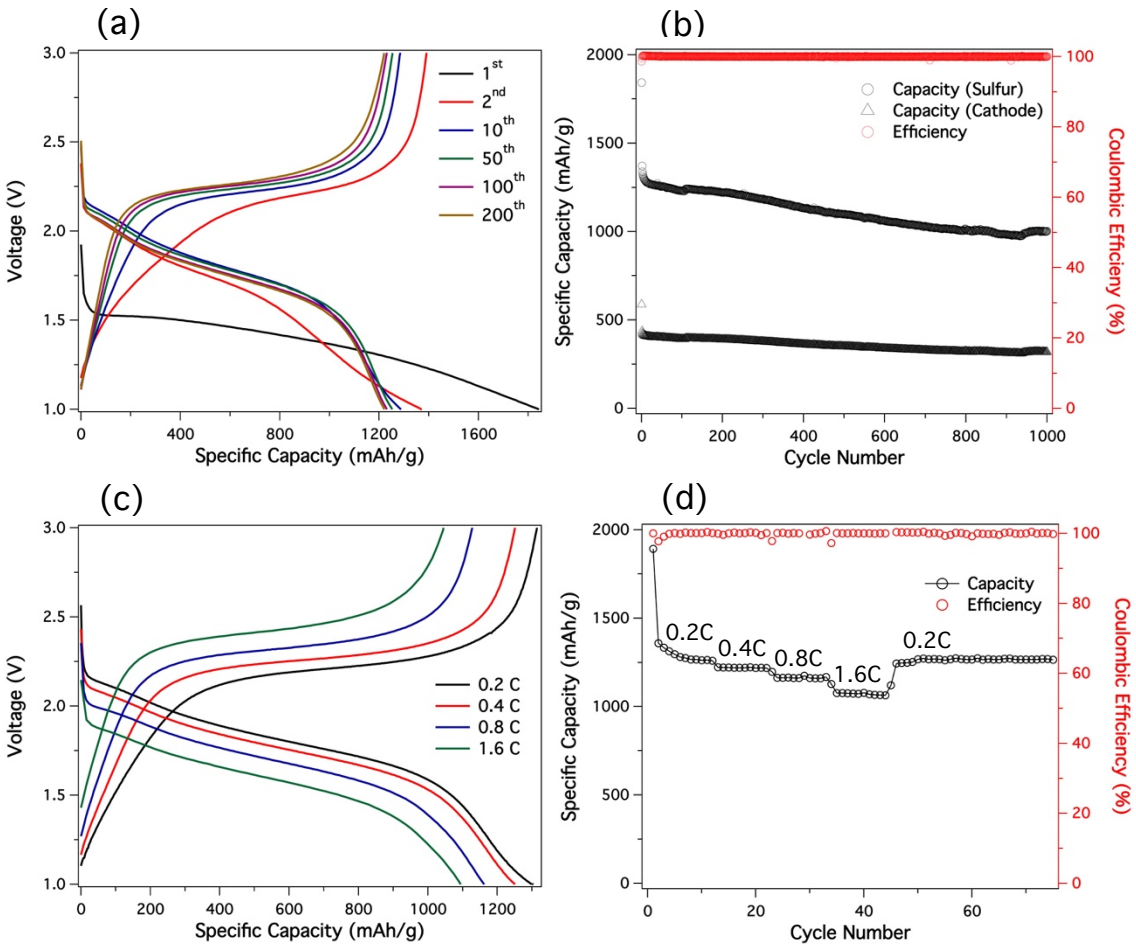

Figure 12: (a) Electrochemical discharge and charge curves of SPAN4 at various cycles. The tests were performed at 0.4 C for both charge and discharge in the potential range of 1–3 V vs Li/Li^+. (b) Capacity and Coulombic efficiencies versus cycle number for PANS4. The black circles report capacities relative to the weight of the active sulfur species in the cathode, whereas the data represented by black triangles are the corresponding capacities based on the overall cathode mass. (c and d) Rate performances of the SPANS measured at various C-rates. The C-rates were same for both charge and discharge in each cycle.

Reaction of sulfur with PAN at high temperature is expected to produce S_x cross-links covalently linked to the carbon rings. After the initial discharge, however, the S-S bond may be expected to break and, upon cell recharge, any sulfur species present in the cathode may spontaneously transform into high order LiPS and S_8, which would remove the benefits of covalently linking the sulfur to carbon in the cathode. The absence of the characteristic 2.35V discharge plateau after

hundreds of discharge cycles of the SPAN4 cathode is somehow able to avoid this fate. Moreover, the charge profile and discharge profile are more symmetric compared to Li-S cells made with elemental sulfur as cathodes, which again indicates that there is excellent utilization of sulfur in the cathode and very little if any losses to the electrolyte.

The inability of unbound smaller sulfur species produced in the cathode after the first recharge to transform to S_8 and, in the subsequent discharge, to LiPS, implies that the smaller sulfur species are perhaps isolated/encapsulated in the cathode. To understand the nature of the interactions that hold the smaller sulfur species in the cathode, we compared the electrochemical behavior of cells in which the commonly used 1M LiTFSI in DOL/DME with $LiNO_3$ (See Figure 13) electrolyte is substituted for the 1M $LiPF_6$ in EC/DEC electrolyte used in the studies reported in Figure 12. It is apparent that this change has dramatic and negative consequences on cell performance. Specifically, while the discharge profile and specific capacity for the first discharge cycle are comparable for SPAN4 cycled in the two electrolytes, it is clear that by the second cycle a two-step discharge profile, analogous to what is seen in a conventional Li-S cell, is observed and that this is accompanied by shuttling and significant deterioration in cell performance upon charging. Even if Guo et al.[72] used solid Li_2S encapsulated in PAN as cathode, a two-step discharge plateau is still observed in a LiPS-soluble tetraethylene glycol dimethyl ether electrolyte. It is evident then that the electrolyte plays a large role, as well as that the smaller sulfur species trapped in the cathode are likely held in place by physical interactions with the carbon host.

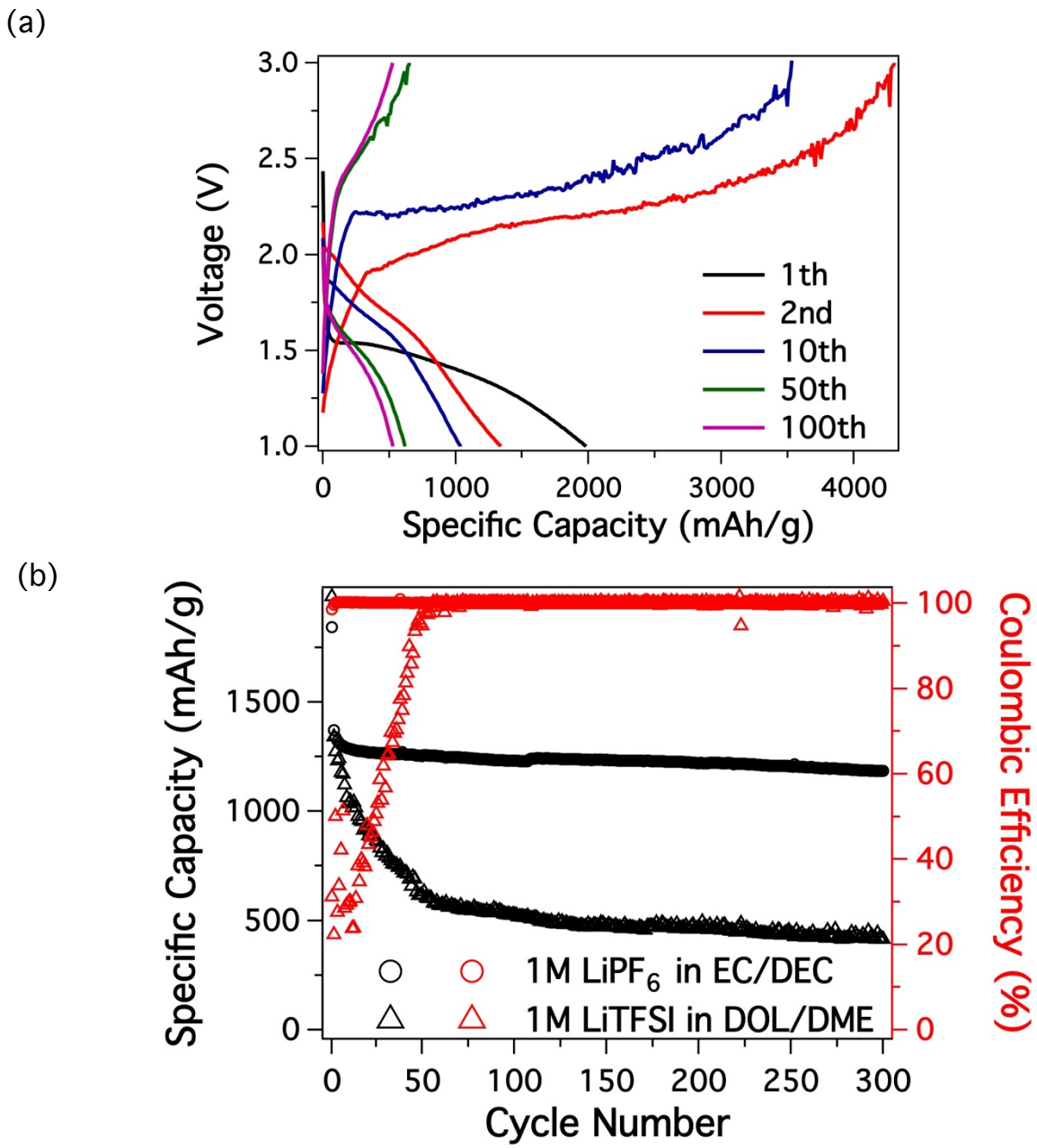

Figure 13: (a) Electrochemical discharge and charge curves of SPAN4 at various cycles in 1M LiTFSI in DOL/DME with $LiNO_3$. The tests were performed at 0.4C for both charge and discharge in the potential range of 1–3 V vs Li/Li^+. (b) Capacity retention and Coulombic efficiencies of PANS4 in two types of electrolytes.

Carbonate-based electrolytes are broadly considered incompatible with Li-S batteries because of the nucleophilic addition reaction between LiPS and the electrolyte, which irreversibly consumes

the active sulfur in the cathode and electrolyte solvent. Our finding that Li-S cells based on SPAN cathode materials cycle more stably in a carbonate-based electrolyte than in electrolytes based on DOL/DME provides additional confirmation that LiPS and its deleterious effects on carbonate electrolytes are somehow avoided when SPAN materials are used as cathodes for Li-S cells. Three hypotheses can be applied to explain these observations: 1) After the first recharge cycle, sulfur exists mainly as S_2 or S_3 in the composite, and cannot form larger S_8 or reactive LiPS species in electrolyte solvents in which the smaller sulfur species or Li_2S have poor/no solubility. This would mean that Li_2S would be the only discharge product in a fully discharged cathode. 2) In the 1-3V voltage window used $LiNO_3$ decomposes and is irreversibly reduced on the cathode surface when the cell is discharged below 1.7 V, the minor plateau in Figure 13a would be the evidence. 3) The higher solubility of LiPSs in DOL/DME promotes recombination and loss of high-order polysulfides to the electrolyte during recharge process. If correct this would confirm common, but heretofore largely untested wisdom, that an electrolyte based on a non-solvent for LiPS with high ionic conductivity would be an ideal choice to confine sulfur in the cathode and ensure electrochemical reaction in the cathode occur all in solid state.

Quantitative experiments were carried out to assess each of these hypotheses. Li_2S was either mixed with elemental sulfur or pristine SPAN4 in desired stoichiometric ratios to form a polysulfide with formula Li_2S_8. EC/DEC and DOL/DME based electrolytes were added to the LiPS species to evaluate their solubility and physical properties. Sulfur concentrations in the resultant four solutions were recorded as a function of time using ICP-AES (Figure 14a) and UV-vis spectra of the solutions recorded after 10 days, are shown in Figure 14b. It can be clearly seen that whereas sulfur is undetectable in the carbonate-based electrolyte it is readily observed in

DOL/DME. What's more, none of the characteristic UV-vis absorption peaks associated with LiPS can be identified in the carbonate electrolyte and no color change is noticed. In contrast, in DOL/DME, irrespective of the source of sulfur, the sulfur concentration in the electrolyte increases with time and a color change from yellow to dark brown can be observed, which are consistent with UV-vis absorption for LiPS. In the case of elemental sulfur, both sulfur concentration and LiPS absorption in UV-vis spectra are much higher than SPAN4, even at comparable sulfur loadings. It means that in the pristine SPAN, electrolyte access to sulfur is limited and that SPAN4 is an effective material for sequestering LiPS. An even broader inference from these observations is that whether the source of sulfur is SPAN or elemental sulfur, the expected polysulfide with lithium sulfide is not formed in the carbonate electrolyte solvent.

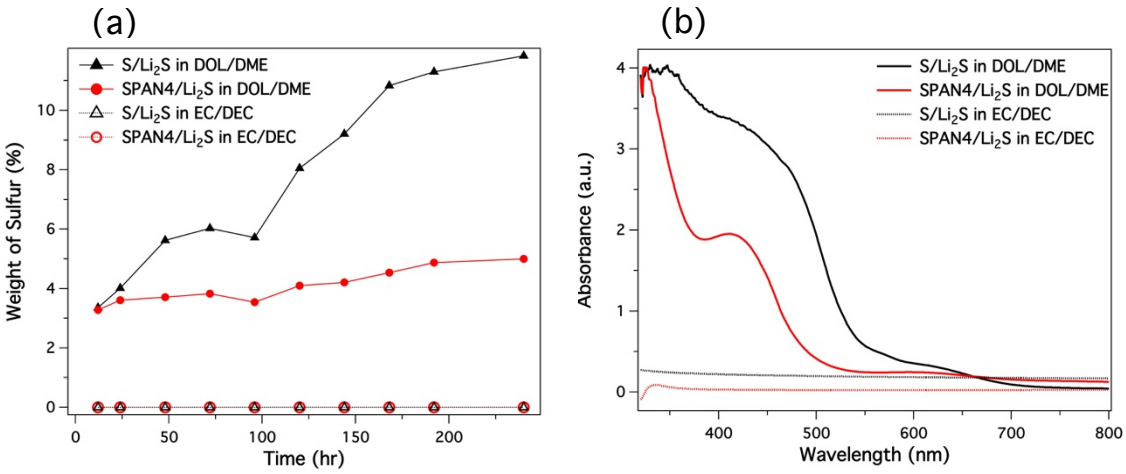

Figure 14: (a) Sulfur content in the electrolyte for four different cases; (b) UV-vis spectra of the solutions for the four samples after 10 days, which are equally diluted with the corresponding electrolyte.

The capability of SPAN4 to hold sulfur can be indirectly assessed in a simple electrochemical measurement that reports the open-circuit potential (OCP) and self-discharge behavior for PAN4 and sulfur in DOL/DME (Figure 15). The OCP for cell based on elemental sulfur as the cathode

is seen to gradually decrease during the two-week time duration of the experiments. The drop in the OCP is accompanied by the LiPS dissolution and a large decrease (~53%) in capacity after two weeks. However, the OCP for the two cells employing cathodes based on SPAN4 show only slight initial decreases followed by a slow stabilization towards the OCP of SPAN after two weeks. It suggests that the cells may need longer time for electrolyte to penetrate the separator and wet the cathode to reach interfacial equilibrium caused by surface tension and strain. The relatively small initial decrease in capacity again suggests that even in the DOL/DME-based electrolyte, SPAN4 has strong ability to hold sulfur and prevent LiPS formation and dissolution in the electrolyte. The decrease in capacity (~25%) is less than half compared to the elemental sulfur cathode after two weeks.

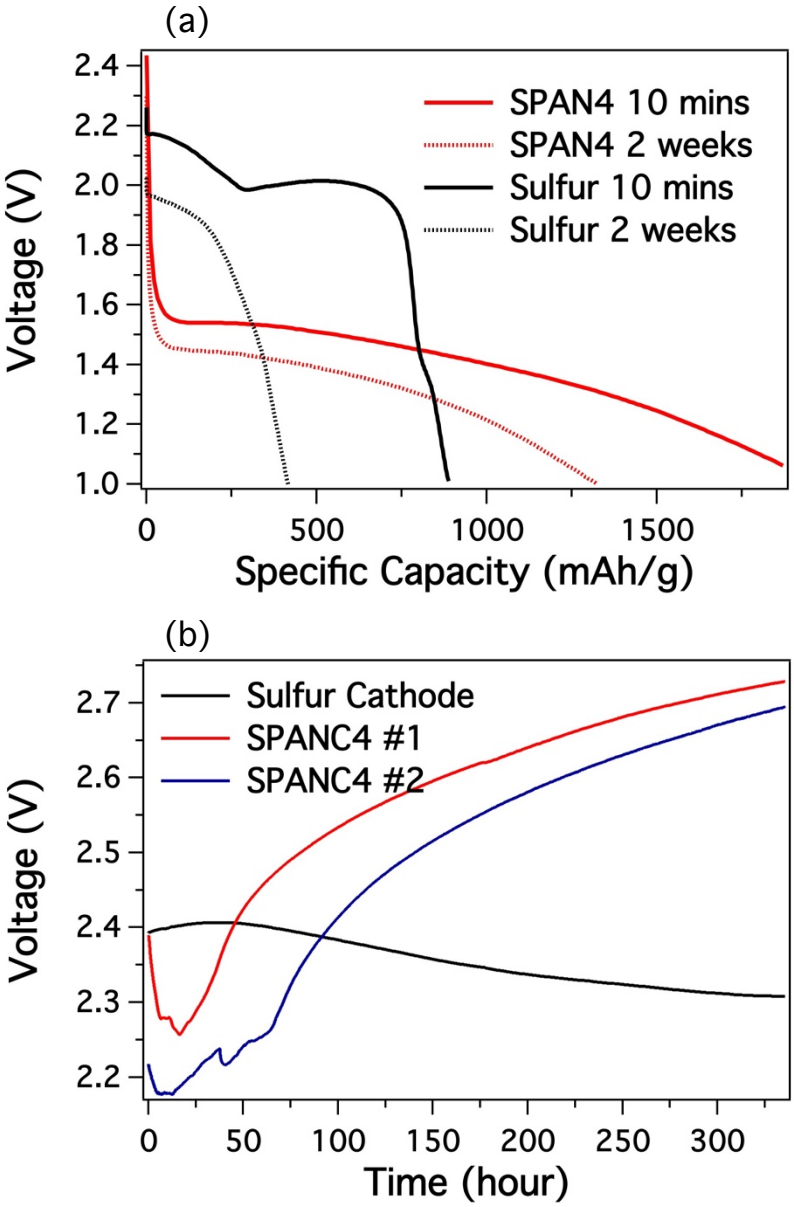

Figure 15: (a) Discharge plateaus of SPAN4 and pristine sulfur cathodes with different resting times in 1M LiTFSI in DOL/DME with $LiNO_3$; (b) Change in open-circuit potential of Li-S and Li-SPAN4 cells with storage time.

In order to better understand the electrochemical reactions in SPAN4 cathodes with carbonate electrolytes, the materials were studied during and post electrochemical cycling using nuclear

magnetic resonance (NMR), X-ray photoelectron spectrum (XPS), Raman spectroscopy, scanning electron microscope (SEM), and energy dispersive spectroscopy (EDS). It is known that the intermediate reaction species in Li-S cells, LiPS, are able to exist in a variety of allotrope forms due to the low energy barriers for recombination and disproportion reactions that transform higher order LiPS to lower order LiPS and vice versa (eg. $Li_2S_6 \leftrightarrow 2LiS_3$). Moreover, due to their atmospheric sensitivity, it is difficult to interrogate these materials using some of the most powerful chemical characterization techniques. Here, we employ an organic conversation method, wherein chemical reaction of LiPS with benzyl chloride is used to transform pure or mixed LiPS into their more stable benzyl polysulfide (BzPS) analogs, without changing the order of the LiPS. High nucleophilicity of thiolate anion makes it possible to achieve nearly 100% conversion of LiPS to BzPS. Systematic application of the method coupled with NMR analysis has been used to characterize the NMR spectra of different BzPS, allowing peak assignments for different BzPS. Figure 16a and b are the NMR spectra obtained by reacting a mixture of DME and benzyl chloride with Li_2S powder, Li_2S_3 solution, and the cycled SPAN4 cathodes; respectively. Distinctive peak assignments for Bz_2S_3 Bz_2S_4 Bz_2S_5 at 4.02 ppm, 4.15 ppm and 4.20 ppm can be found from the spectra, which are in accordance with previous literature. A single Bz_2S peak at 3.60 ppm can be found, for example, in the Li_2S case. On the other hand, the spectrum for Li_2S_3 (obtained by reacting Li_2S and S_8 in a 4:1 molar ratio) clearly shows that this material is a mixture of multiple species. Based on the reference spectra, we conclude that Bz_2S is the only BzPS species that exist in the discharged SPAN4 cathode. This clearly means that Li_2S is the only or the dominant discharge product in the cell. Significantly, once the cell is charged to 3 V, the chemical shift for Bz_2S disappeared and a broadened curve arises between 3.80 and 4.0 ppm, consistent with

expectations for sulfur interacting/bonded to a polymeric species. After the 10th cycle of discharge, the peak for Bz_2S is seen to still exist. NMR spectra of the cathodes cycled at intermediate stages of discharge and charge are shown in Figure S10 with Bz_2S signal detected only. Our results therefore lend support to the hypothesis that the improved sulfur utilization of the SPAN4 cathodes is a result of the fact that elemental sulfur is fully reduced to Li_2S upon discharging. As no intermediate LiPS are found in the spectrum, it is also apparent that higher order sulfur species do not exist in the SPAN4 composite cathode.

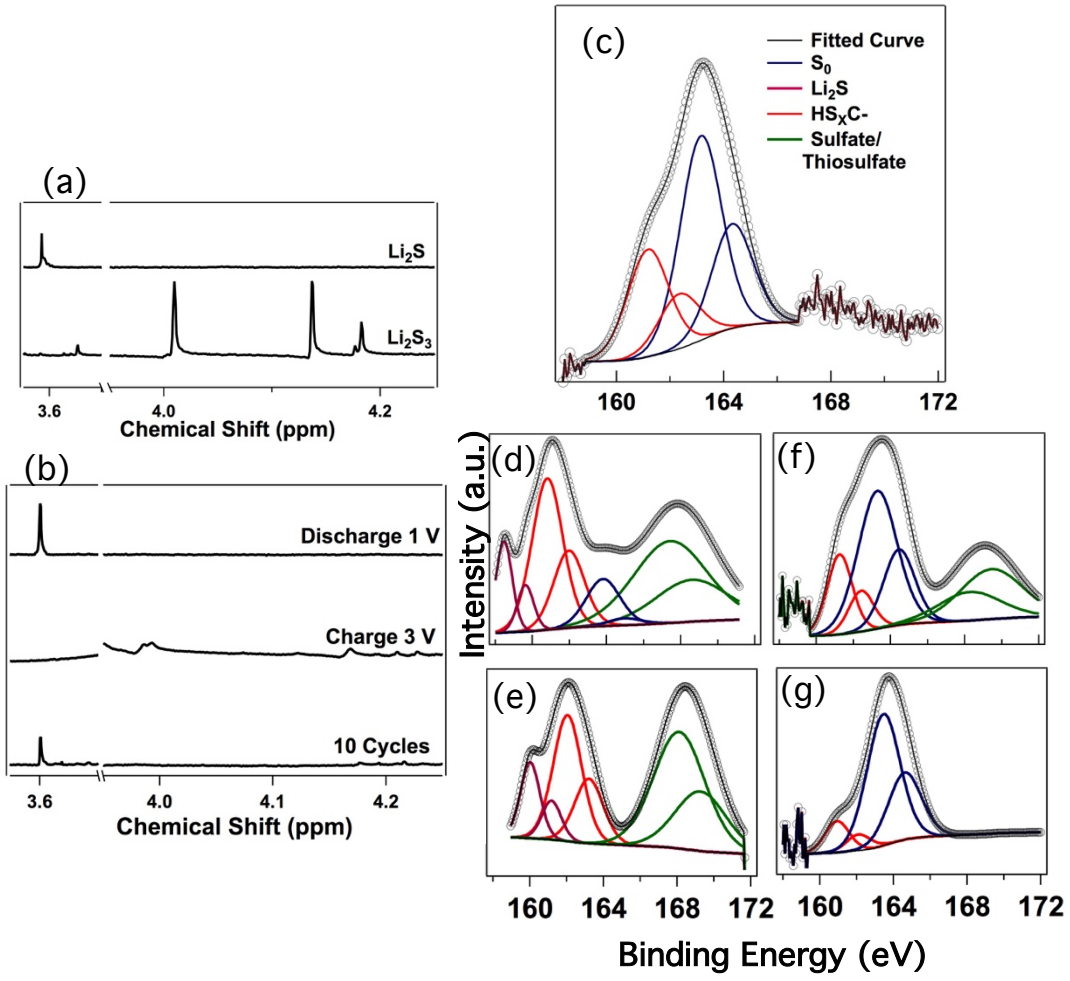

Figure 16: ^1H NMR spectra of the converted BzPS from (a) Li_2S powder and Li_2S_3 solution and

(b) SPAN4s at different cycling states; Ex situ XPS spectra of S 2p in SPAN4s at (c) pristine and different cycling states (Cell was discharged to (d)1.25 V and (e) 1V and cell was recharged to (f) 2.25 V and (g) 3 V at the first cycle respectively).

XPS analysis of SPAN cathodes evaluated at different states of discharge and charge provide additional insights into the electrochemical mechanisms through which these cathodes are able to achieve their exceptional cycling performance. XPS spectra in the C 1s region (Figure 17a) for the pristine SPAN4 reveal that C1s band can be split into three peaks. The main peak at 284.6 eV corresponds to the sp^2 type C-C component. The peak at 286.4 eV can be partially ascribed to C-S or C-N bond. The minor peak at 289.3 eV represents extended delocalized electrons in the composite, resulting in a satellite structure. Figure 4c to g presents S 2p spectra for the pristine SPAN and cathode at different galvanostatic cycling states. S 2p spectra for pristine cathode show an overlapped band with two shoulder bands. The main S2p 3/2 peak at 163.4 eV (Figure 16c), slightly lower than binding energy of elemental sulfur (164.0 eV) is consistent with the presence of C–S bonds in the composite. Another S2p 3/2 peak at 161.2 eV can be attributed to adsorbed HS_xC- byproduct generated in the sulfurization reaction on the surface of the composite.[12] Upon discharging (Figure 16d and e), the peaks for elemental sulfur are seen to disappear and new peaks at 168.2 eV arise from the sulfate/thiosulfate complex species most likely formed by the oxidation of Li_2S when processing the cathode for XPS characterization. As the peak attributed to Li_2S around 160 eV appears when discharging and disappears during charging, and no other LiPS could be found, we attribute that Li_2S is the final discharge product in the cathode, which is consistent with our earlier study. We also found that peaks represent delocalized electrons in C 1s spectra increased dramatically upon discharging (Figure 17b), suggesting sulfur interacts with conjugated carbon backbone during lithiation. When the cell is charged (Figure 16f and g), the oxidized sulfur

peaks gradually disappear, and peaks for elemental sulfur reappear, suggesting sulfur recovers to elemental state. Based on the fact from XPS C 1s spectra and Raman spectra (Figure 18) that S-C bond recovers upon charging, we conclude that carbon in SPAN is able to reform strong bond with sulfur.

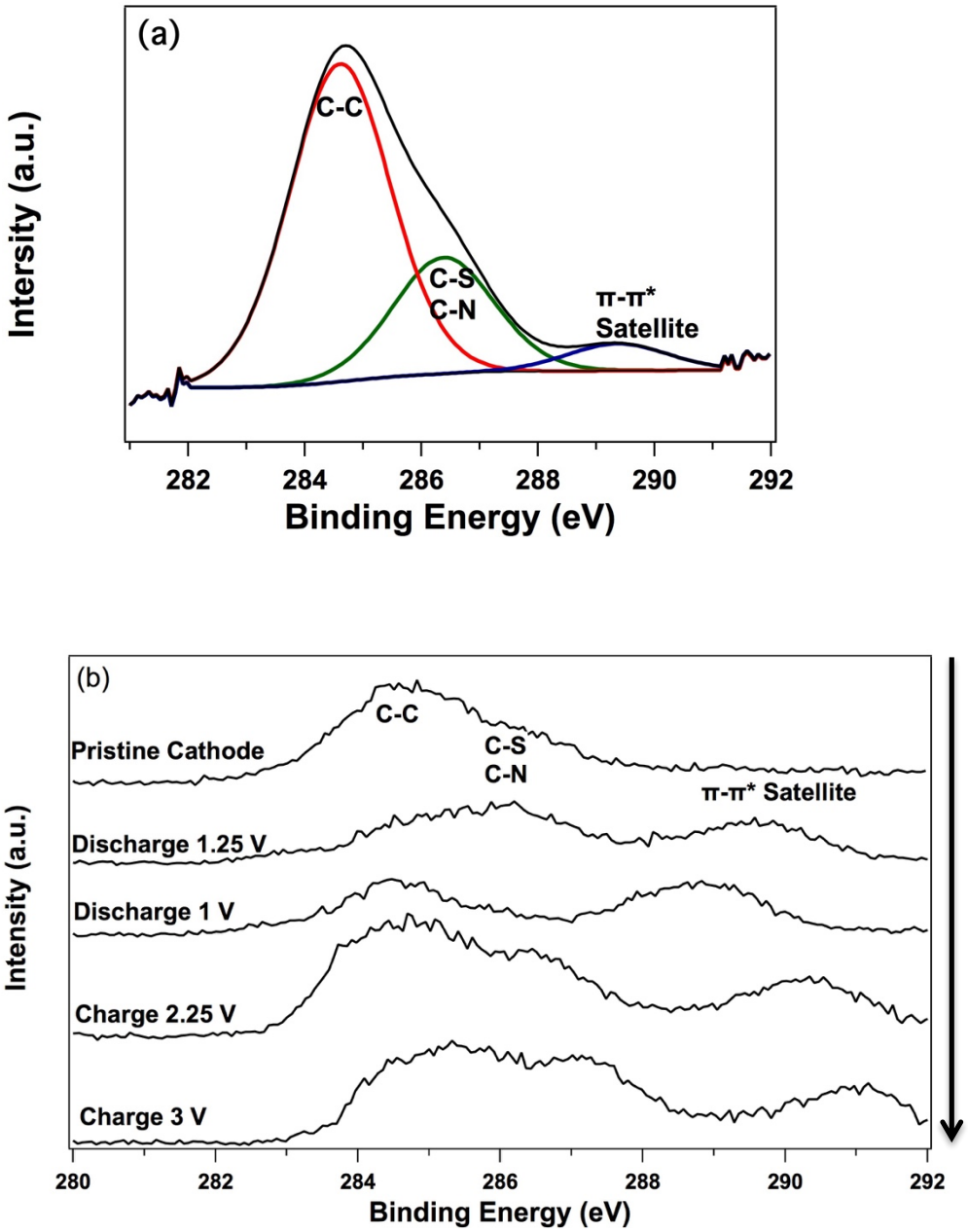

Figure 17: Ex situ XPS spectra of C 1s in SPAN4s at (a) pristine state (Black lines are the fitted

curves) and (b) different cycling states (cell was discharged to 1.25 V and 1V, then cell was recharged to 2.25 V and 3 V at the first cycle respectively).

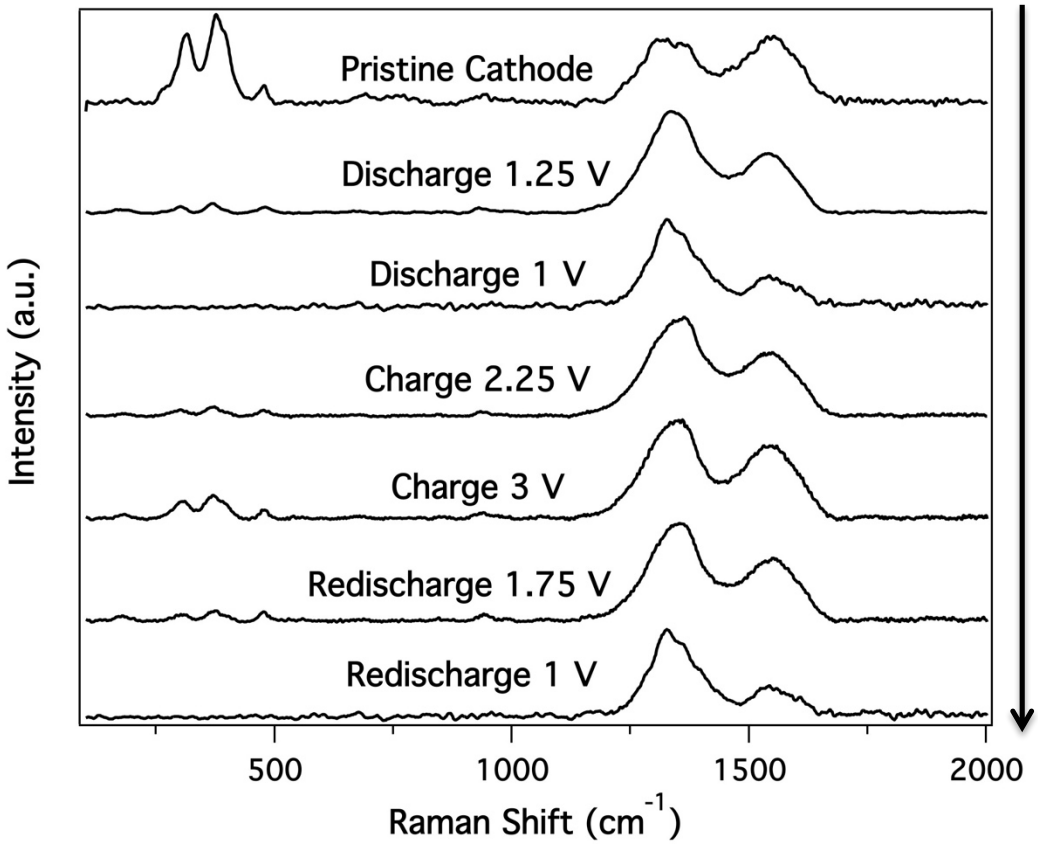

Figure 18: Ex-situ Raman spectra in the range of 100–2000 cm-1 during the first two cycles of SPAN4s.

Additional insights about the electrochemical characteristics of the SPAN4 cathodes can be deduced from cyclic voltammetry (CV). In particular, by using CV to interrogate behaviors in multiple electrochemically active sulfur compounds containing sulfur species similar to what we hypothesize to exist in the SPAN4 cells, it is possible to confirm that sulfur in the form of S_2 and S_3 are the dominant species in the cathode. In particular, Li_2S_3 cross-linked to PAN (obtained

using the method reported by Guo et al.[72]) (Figure 19b); tetramethylthiuram disulfide (TMTD) (Figure 29c); bis(p-tolylsulfonyl) trisulfide (BPTT) (Figure 19d); dipentamethylenethiuram tetrasulfide (DPMTT) (Figure 19e) containing oligosulfides covalently linked to organic molecules were each employed as cathode vs. lithium and their electrochemical behaviors compared with those for SPAN4 (Figure 19a). CV curves for SPAN4 for multiple redox cycles are shown in the graph. It displays a lower plateau for the first reduction process, which agrees well with the voltage profile deduced from galvanostatic cycling studies shown previously.

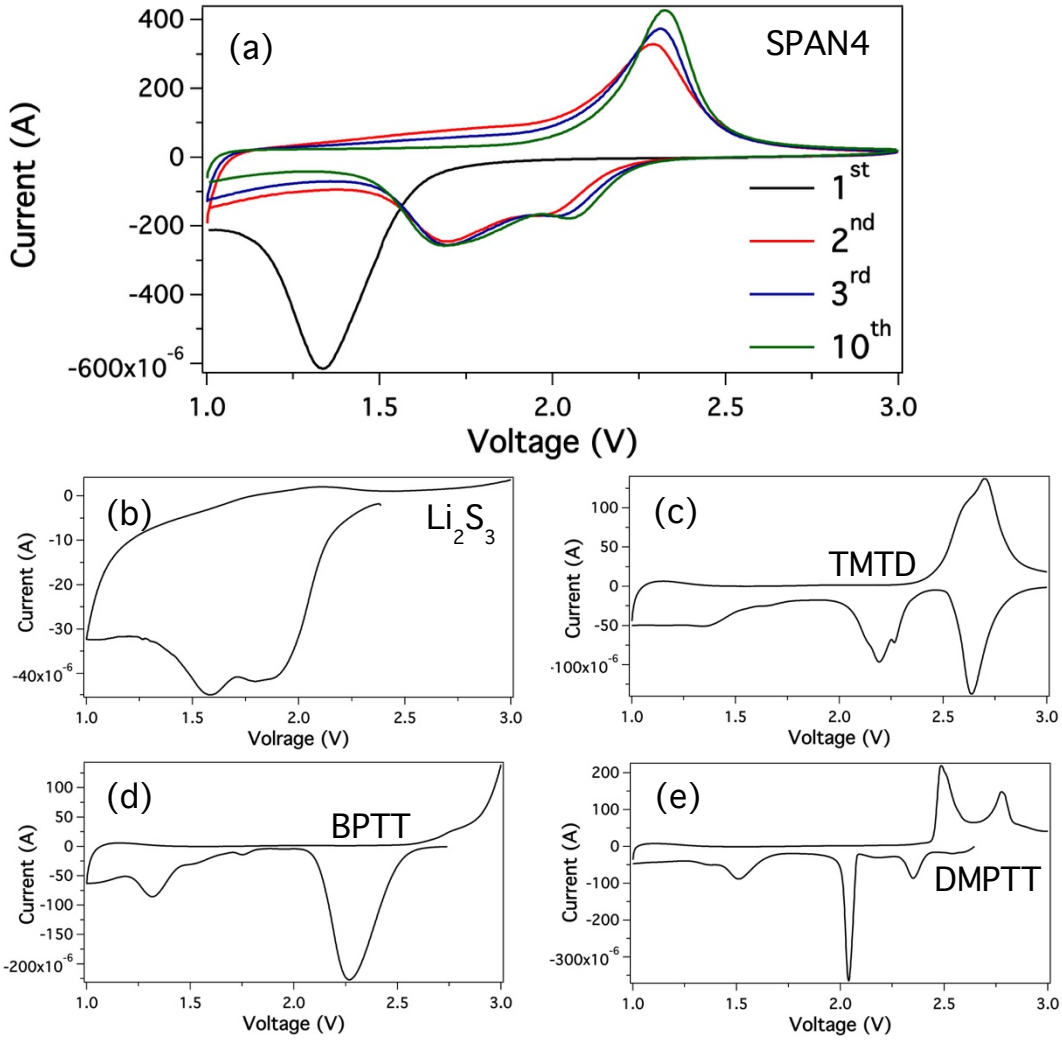

Figure 19: Cyclic voltammograms of the (a) as-prepared SPAN4 composite cathode; (b) Li_2S_3 cross-linked to PAN cathode; (c) tetramethylthiuram disulfide (TMTD) cathode; (d) bis(p-tolylsulfonyl) trisulfide (BPTT) cathode; (e) dipentamethylenethiuram tetrasulfide (DPMTT) cathode at a scan rate of 0.1 mV/s.

It is known that organosulfur-based polymer materials with S-S linkages are capable of reversibly cleaving and reforming based on the redox chemistry of thiolates (RS^-), which can be oxidized to the corresponding radical (RS) and in turn, couple to form disulfides (RSSR). This process involves one electron transfer such that the capacity is not high compared to elemental sulfur. As these molecules contain other functional groups like thiuram and sulfonyl terminals, the reduction peaks at higher voltage can be ignored, as they are probably related to the reduction of these complex functional groups that are not related to the bond cleavage in sulfides. The reduction peaks at voltages below 2.1 V are thought to arise from S-S bond breakage. And, there is a clear relation between the number of peaks in this section of the CV spectrum and the number of S-S bonds in the materials. TMTD for example shows one broad reduction peaks at ~1.3 V, like the initial reduction peak for SPAN. This suggests that during the first discharge, the S-S bond that adjacent to carbon ring breaks in SPAN4 composite and it requires higher energy input.

During following cycles of discharge, CV profile for SPAN shows similarity with Li_2S_3, these can be explained that sulfur that detached from the carbon ring maintains its two-electron transfer properties. A two-electron process is also consistent with the high specific capacity of this material. The absence of a similar sharp reduction peak for SPAN4 compared to DMPTT at 2.05 V, is thought to provide additional evidence that during the first discharge, the S-S bond adjacent to carbon ring breaks in the SPAN4 composite and requires higher energy input. Thus, based on these organic sulfide compound analogues, we propose that in SPAN4, electrochemically active sulfur exists principally as S_3 or S_2 attached to the adjacent carbon backbone. The complete reduction of

either species is achieved in a two-electron transfer process, which is likely responsible for the high specific capacity of the material.

We close by considering the effect of a SPAN-based cathode in the Li-S cell on the metallic lithium anode. As discussed earlier, carbonate electrolytes exhibit minimum solubility for LiPS and Li-S cells based on SPAN cathodes exhibit high coulombic efficiency and no evidence of shuttling. We examined the morphology of lithium anodes for the Li-SPAN4 cells after 500 cycles of galvanostatic charge and discharge in both EC/DEC and DOL/DME electrolytes. Figure 20a shows the SEM image and EDS mapping of the lithium anode in carbonate electrolyte. A very dense and uniform SEI layer can be observed on the anode for cells cycled in EC/DEC electrolyte. The time-dependent growth of the SEI can explain the increase in interfacial resistance in impedance spectra (Figure 21) of the cell upon cycling, as the diffusion length is longer. This SEI can protect lithium and probably minimize lithium dendrite formation, enable stable cycling capability. Remarkably, EDS mapping of the SEI shows no evidence of sulfur, meaning that shuttling can be eliminated when using a non-solvent electrolyte for LiPS in the cell. Thus, complete sequestration of electrochemically active sulfur in the cathode not only facilitates complete reduction and high specific capacity, but also provides a well-protected anode, which contributes the cycling stability for the Li-SPAN4 cell. The morphology of cathode after cycling is well maintained and no obvious change can be identified from SEM images (Figure 22). However, when the cell was cycled in DOL/DME, a loose and cracked SEI was observed on lithium anode with abundant sulfur signal being detected shown in Figure 20b, explaining the shuttling phenomena where LiPS attack lithium metal and result in the loss of active cathode mass.

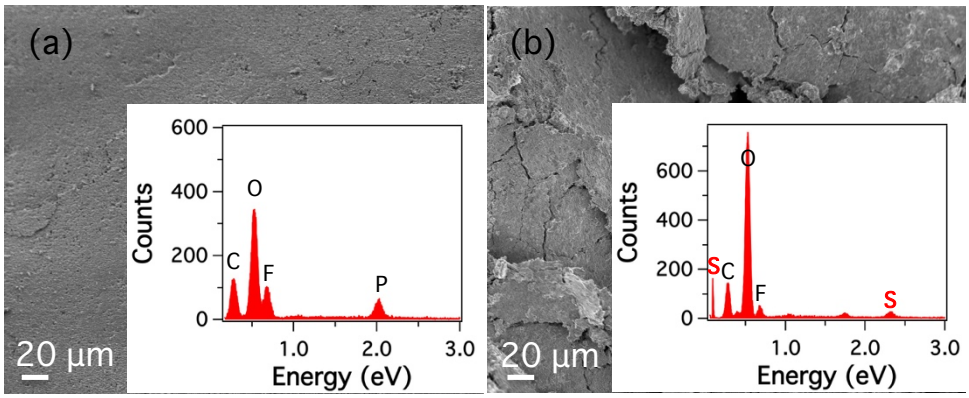

Figure 20: SEM images and EDS mapping of the lithium anode after 500 cycles in (a) EC/DEC; (b) DOL/DME based electrolyte.

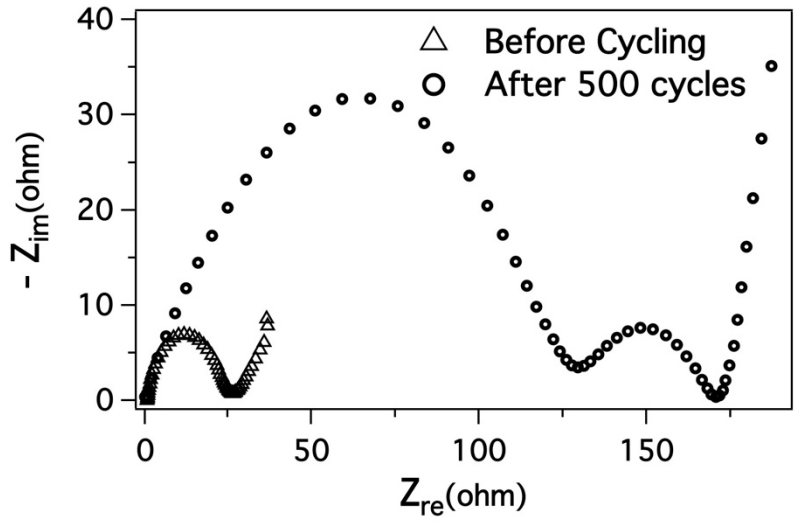

Figure 21: Nyquist plots of the Li-SPAN cells before and after 500 cycles.

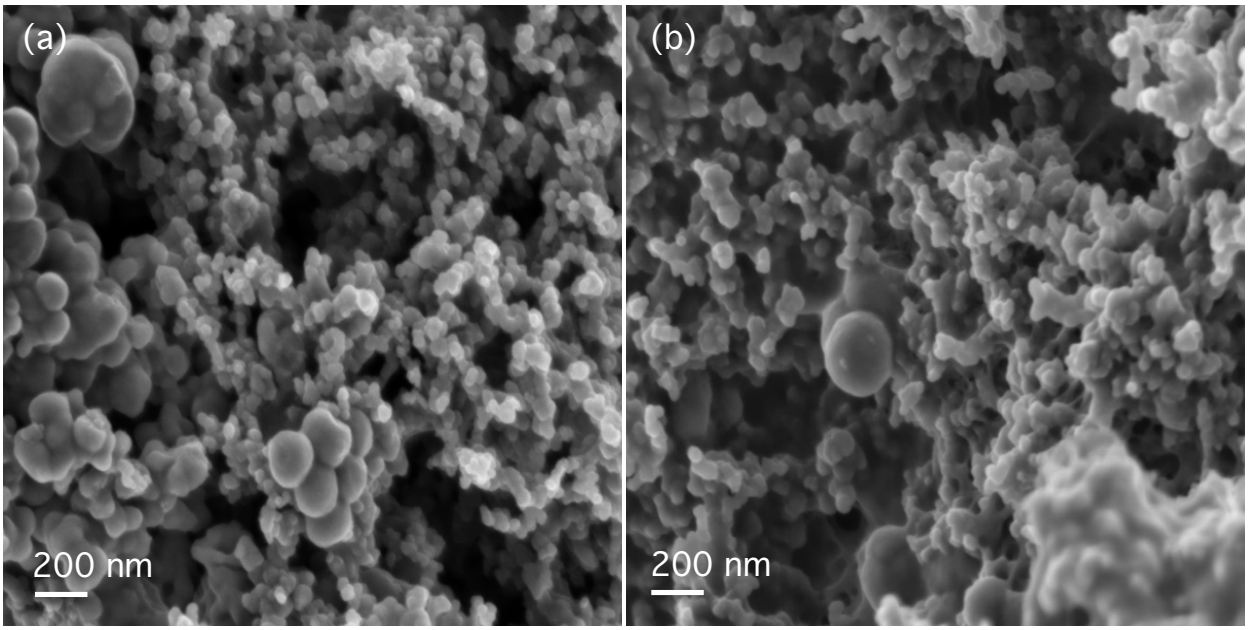

Figure 22. SEM image of the SPAN4 cathode before and after 500 cycles.

2.3 CONCLUSION

We have used a straightforward thermal synthesis process to create sulfur/PAN (SPAN) nanocomposites in which sulfur is so strongly linked to a conductive polymer host that its solution state electrochemistry is different from that of bulk S_8. By means of spectroscopic and electrochemical methods, we deduce that in these SPAN composites sulfur exists as S_3/S_2 units covalently attached to a carbon backbone containing pyridinic-N units. When used as cathodes in lithium-sulfur cells, the SPAN nanocomposites exhibit high active materials utilization, exceptional stability in extended cycling, and none of the shuttling behaviors characteristic of cathodes based on elemental sulfur. We show that the beneficial electrochemical attributes of the materials are not only a consequence of the strong interactions between sulfur and its conductive host, but is also a consequence of the host's ability to prevent formation of S_8 after complete oxidation during the cell recharge.

The most impressive electrochemical performance of the SPAN nanocomposite cathodes is achieved in carbonate electrolytes with minimum solubility for high-order lithium polysulfide (LiPS). In Li-SPAN cells containing these electrolytes and none of the usual salt additives (eg. $LiNO_3$) required to stabilize the anode in conventional Li-S cells, we find no evidence of such reactions or of LiPS shuttling. We find instead that the electrochemical reactions between elemental sulfur in the cathode and Li ions in solution occur fully and with high efficiencies, yielding Li_2S in the solid state as the only discharge product. In contrast, Li-SPAN cells based on electrolytes containing DOL/DME solvent exhibit poor cycling, LiPS shuttling, and low efficiencies. Although more work is needed to fundamentally understand the structure evolution of sulfur in PAN during redox processes in the cathodes, our results support our hypothesis that sulfur exists stably as smaller S_2/S_3 species in the SPAN nanocomposites even after the materials are subjected to galvanostatic cycling for hundreds of cycles.

2.4 EXPERIMENTAL SECTION

2.4.1 Synthesis

All chemicals were purchased from Sigma-Aldrich unless otherwise specified and used without purification. To synthesis SPANs, polyacrylonitrile (PAN, M_w=150,000) was mixed with sulfur powder in a mass ration of 1:4 and ball milled for one hour to ensure homogeneous mixing. The mixed samples were heated in a nitrogen-filled furnace at 250 °C, 350 °C, 450 °C, 600 °C for 6 hours with a ramping rate of 5 °C/min to carbonize PAN and to yield final products respectively. A control sample PANC was created by the same process but without mixing with sulfur powder and heated to 450 °C.

2.4.2 Characterization

The morphologies of SPAN4 were studied using FEI Tecnai G2 T12 Spirit Transmission Electron Microscope (120kV) and elemental mapping (EDX and EELS) was performed using FEI Tecnai F20 Transmission Electron Microscope (200kV). Thermogravimetric analysis was performed using TA Instruments Q5000 IR Thermogravimetric Analyzer. The crystal structures of the products were characterized using Scintag Theta-theta X-Ray Diffractometer (Cu Kα, λ=1.5406 Å). Raman spectra were collected using a Renishaw InVia Confocal Raman Microscope (laser wavelength = 488nm). Fourier Transform Infrared Spectra were taken using a Bruker Optics Vertex80v Infrared Spectrometer. Inductively coupled plasma atomic emission spectroscopy (ICP-AES) was used to quantify sulfur content in the electrolytes as a function of time. UV-vis spectra were collected by Shimadzu UV-Vis-NIR Spectrometer. ^{1}H NMR spectra were taken by Inova-400 Spectrometer. X-ray photoelectron spectroscopy (XPS) measurements were performed with a Surface Science SSX-100 spectrometer using a monochromatic Al Kα source (1486.6 eV). Non-linear least squares curve fitting was applied to high-resolution spectra, using CasaXPS software. A LEO 1550 high resolution scanning electron microscopy (HRSEM) with elemental mapping (EDS) was employed to characterize the morphology of the composite electrodes.

The lithium polysulfide dissolution experiments were carried out in the following: Due to the sensitivity of LiPS to air, all the following procedures were performed in an argon-filled glovebox (MBraun Labmaster). Li_2S and S with a molar ratio of 1:7 (49.5 and 224 mg) were mixed and added in 2 ml of the two electrolytes (1M $LiPF_6$ in EC/DEC and 1M LiTFSI in DOL/DME with $LiNO_3$ as additive). Li_2S and SPAN4 were done in the similar method with equal sulfur content in the mixture. 10 μL solution from the four samples was timely collected and subjected to ICP-AES test to quantify sulfur content in the electrolyte. Sulfur contribution from LiTFSI was excluded.

Organic conversion experiments were performed by the following: To convert lithium sulfide (Li_2S) to benzyl sulfide (Bz_2S), 5 mg Li_2S was added in 1 mL mixture of benzyl chloride and 1, 2-dimethoxyethane (BzCl/DME) (v:v = 1:1) and allowed to sit for four days for the conversion to complete. To convert LiPS solution to BzPS, 20 μL 1 M Li_2S_3 in DME (synthesized by mixing Li_2S and S with stoichiometric ratio of 2 : 3 between Li and S in DME) was added in 1 ml mixture of BzCl/DME and allowed to sit for three hours. The LiPS solution becomes transparent and colorless immediately after mixing with BzCl/DME, suggesting quick conversion from LiPS to BzPS. To convert the intermediate species in the cathode, the Li-SPAN4 cells cycled at different stages were opened and the cathodes were soak in the mixture of BzCl/DME and sonicated for 3 hr and kept in the solution for 4 days as more time is needed to convert Li_2S to Bz_2S than LiPS to BzPS.[1] After that, solvents could evaporate from the samples. The samples were then mixed with chloroform-d and filtered out of impurities (mainly carbon black on the cathode). They were then transferred to NMR tube and subjected to NMR test.

2.4.3 Electrochemical Characterization

Electrochemical characterization of the SPAN nanocomposites as cathode materials in rechargeable lithium batteries was performed at room temperature in 2032 coin-type cells. The working electrode consisted of 70 wt% of the active material, 15 wt% of carbon black (Super-P Li from TIMCAL) as a conductivity aid, and 15 wt% of polymer binder (PVDF, polyvinylidene fluoride, Aldrich). A carbon-coated aluminum foil (0.004 in thick, Alfa Aesar) was used as the current collector. Typical thickness of the active material film is ~0.02 mm and mass per unit area is ~0.85 mg SPAN/cm^2. Lithium foil (0.03 in thick, Alfa Aesar) was used as the counter and reference electrode. Celgard 2500 polypropylene membranes were used as the separator. 40 μL

1M Lithium hexafluorophosphate in a mixture ethylene carbonate (EC) and diethyl carbonate (DEC) (v:v = 1 :1) or 1 M lithium bis(trifluoromethanesulfone) imide (LiTFSI) and 0.2 M $LiNO_3$ in 1, 3-dioxolane and 1, 2-dimethoxyethane (DME) (v:v 1:1) were used as electrolyte for the cells. Cell assembly was carried out in an argon-filled glove-box (MBraun Labmaster). The room-temperature cycling characteristics of the cells were evaluated under galvanostatic conditions using Neware CT-3008 battery testers and electrochemical processes in the cells were studied by cyclic voltammetry using a CHI600D potentiostat. Electrochemical impedance Spectroscopy tests were conducted by using a Solartron Cell Test System model 1470E potentiostat / galvanostat.

3 A STABLE ROOM-TEMPERATURE SODIUM SULFUR BATTERY

3.1 INTRODUCTION

Advance in rechargeable lithium batteries has successfully dominated portable electronics and electric vehicles as energy storage systems since their discovery[2, 3, 74, 75]. Various efforts on developing lithium-sulfur (Li-S) batteries are being devoted due to the high theoretical energy density (2500 W h kg^{-1}), the nature abundance as well as the environmental benignity of sulfur electrode, with great progress being achieved during the past decade[45, 58, 70, 73, 76-78]. However, the cost and feasibility of lithium anode hinder the implementation of lithium-based technology for large-scale storage such as automotive transportation and grid-related application. In such way, new chemistry is needed[79-81], and sodium, the second lightest and smallest alkali metal with much less cost and unlimited everywhere resources, is one of the most appealing alternatives for lithium[82, 83].

Quite surprisingly, although the commercialized stationary energy storage systems - high temperature sodium-sulfur (Na-S) batteries operated at > 300 °C with molten electrodes suggest a large scale and feasible rechargeable battery based on sodium metal[46, 47], room temperature (RT) Na-S batteries, the analogues of Li-S batteries, seem to be hardly understood and investigated. This indicates more obstacles related to RT Na-S batteries need to be solved and different cell chemistries between Li and Na based batteries. The differences are probably related to the larger size of the sodium ion that affects the phase stability, the solubility, the transport properties and the interphase formation as well as the less reducing nature of Na ions compared to Li ions[83]. In addition to more severed challenges facing Li-S batteries such as insulating nature of sulfur and discharge product lithium sulfide (Li_2S), intermediate soluble lithium polysulfides

(LiPS) induced shuttling, and volume expansion upon discharging on the sulfur cathode side of RT Na-S batteries[73, 84-86], sodium metal is seen to less likely form a stable solid-electrolyte interphase (SEI), which easily causes defects on the surface and parasite dendrites at higher current densities, resulting in cell instability during Na electrodeposition. The phenomena have been observed in Na-O_2 batteries[87] and even in Na metal anode when operated at molten state in high temperature Na-S batteries[47], leading to instable charging and low Coulombic efficiency. Therefore, to construct a stable cycling RT Na-S battery, solutions on both sulfur and sodium electrodes sides are necessary.

Generally, to construct a performing RT Na–S battery, the utilization of active cathode material is directly dependent on the accommodation ability of the conductive cathode host due to the insulating nature of both fully charged and discharged products (S and Na_2S) and the soluble nature of the intermediate sodium polysulfides (NaPS) produced during cycling[88]. In this regard, sulfur infused in microporous carbon materials with high surface area for chemical and electrochemical reaction and strongest physical confinement for polysulfides with nonpolar interaction between carbon host and sulfur are preferred[19, 48, 49]. These types of sulfur cathodes are compatible with carbonate electrolytes, which has been demonstrated to react with soluble high-order polysulfides (PS) in traditional Li-S batteries[89]. This indicates a solid-state reaction directly from sulfur to solid sulfur species in the cathode without forming reacting and soluble PS, which can diffuse and dissociate in electrolyte and subsequently induce shuttling. On the anode side, techniques for preventing dendrite formation in lithium metal batteries should necessarily be involved. Some of the successful methods in Li batteries, for examples, adding hybrid silica particles[90, 91] or LiF in electrolyte[92] or coating a protective hollow carbon sphere layer[23]

on lithium metal, to allow stable Li deposition and prevent dendrite formation could perhaps work in Na battery system.

We herein construct a stable cycling RT Na-S battery in coin cell (Figure 23a), using an Na metal anode, a microporous carbon polyhedron-sulfur composite cathode (MCPS) by infusing sulfur into microporous carbon which is derived from metal-organic framework (MOF), and a liquid electrolyte made by dissolving $NaClO_4$ salt in carbonate electrolyte with hybrid ionic liquid silica nanoparticle (SiO_2-IL-ClO_4) additives as stabilizing agent. The large difference in size between Na atom and Na ion and less reducing nature of Na ion results in non-even electrodeposition upon charging in Na-metal batteries. This phenomenon, which is seen to be independent of cell discharge and related to higher current density, however remains unsolved, and as a result, leads to very low Coulombic efficiency and cell failure. Therefore, unlike Li-S batteries, where Coulombic efficiency plays a critical role to evaluate cell performance, research on Na-S batteries rarely reports Coulombic efficiency.

By adding IL nanoparticles, our cell can achieve excellent cycling performance with nearly 100 % Coulombic efficiency at higher current density and with higher sulfur loadings, suggesting stable Na deposition. In addition, by applying the composite cathode, we could get a reversible capacity of over 860 mAh/g at 0.1C (1C=1675 mA/g) and 600 mAh/g at 0.5C based on active sulfur mass. The battery is able to cycle stably for over 100 cycles at 0.5C with 0.31 % capacity decay per cycle. The electrochemical properties on sodiation and desodiation of the constructed Na-S cell were investigated based on spectroscopic tools and analysis. Moreover, the low diffusivity of Na^+ into the composite cathode calculated from electrochemical data suggests a solid-state diffusion, indicating a different reaction mechanism compared to traditional metal-sulfur batteries, as no

soluble PS species are formed when using microporous carbon-sulfur composite, which also contributes to the stability and high capacity retention upon cycling.

3.2 RESULTS AND DISCUSSION

We start by looking at the effect of particle additives on electrochemical stability of the cell. An electrochemical floating test was performed in the potential range from 3.0 V to 5.0 V. As shown in Figure 33b, electrolytes without particles start to show an increase of current as the potential increases and exhibit an unstable time-dependent current response when the potential reaches 4 V. In contrast, electrolytes containing particles exhibit much lower current response and display attractive stability at least up to 4.5 V. It suggests that, higher leak current caused by higher potential leads to instable charging, while particle additives have beneficial effects on stable sodium electrodeposition, as well as enhances the potential limit of the electrolyte, which can lead to the improved cycling performance. Ionic conductivity (Figure 23c) of the cell with different amount of particle additives is presented as a function of temperature. It can be noticed that temperature-dependent ionic conductivities are found in electrolytes with particles, where local segmental motion, chain relaxation, and crystallinity probably play important roles that increase the stability of the cells. Cell with 10 vol % particles in electrolyte can maintain this feature just below the melting point of Na metal (97.72 °C), which could also indicate the enhanced stability of the cell. However, cells with no particle additives show irregular increased conductivity with temperature, suggesting less stability of the cells. Based on both analysis, we proposed that SiO_2-IL-ClO_4 additive may probably play two roles to stabilize the cell: ionic liquid helps chemically form a stable SEI layer by decomposing on the surface of sodium metal[90], while silica particle can physically reduce electric field by increasing the length scale of the electric field to the size of

the particle and the viscosity of the electrolyte which is indicated by the increase in interfacial resistance of the cell.

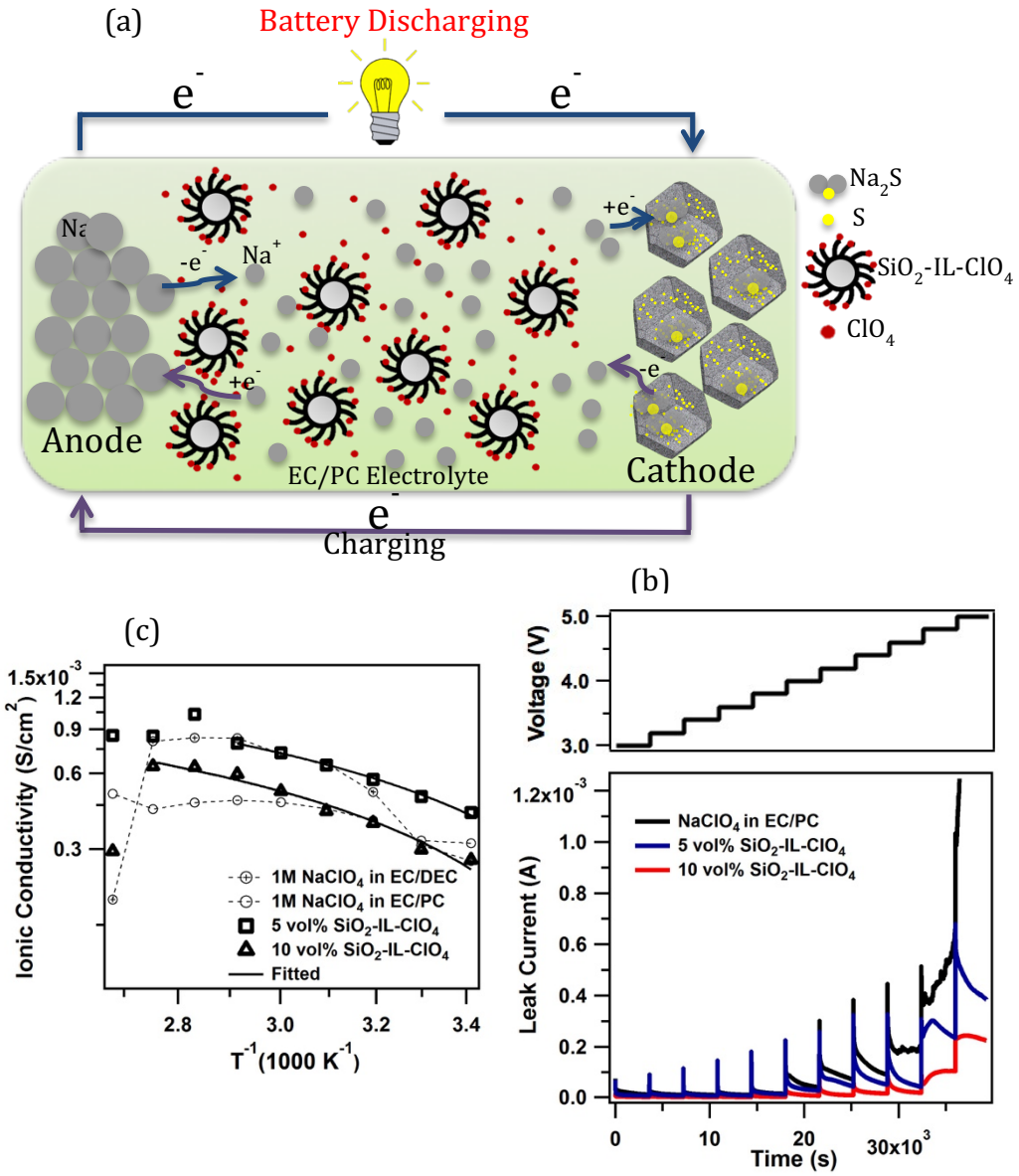

Figure 23: a, Schematic drawing of the Na-S cell during galvanostatic cycling, using SiO_2-IL-ClO_4 as additive in 1M $NaClO_4$ in a mixture of ethylene carbonate and propylene carbonate (EC/PC) (v:v = 1:1). On the anode side, sodium atom loses electron to form sodium ion during discharge. Sodium ion diffuses inside the microporous carbon-sulfur composite (MCPS) and reacts with sulfur to form sodium sulfide (Na_2S) on the cathode side, and the reverse reaction took place during charging, where SiO_2-IL-ClO_4 helps stabilize sodium anode. b, constant voltage-charge

profile of the Na-S cells with different volume fraction of SiO_2-IL-ClO_4 in the electrolyte maintained at 3.0, 3.2, 3.4…5.0 V for 1 h at room temperature. c, Ionic conductivity of the Na-S cells with different volume fraction of SiO_2-IL-ClO_4 in the electrolyte as a function of temperature. EC/DEC represents a mixture of ethylene carbonate and diethyl carbonate (v:v = 1:1). The solid lines are linear Vogel–Fulcher–Tammann fits for the temperature-dependent ionic conductivity.

In metal-sulfur batteries, cathode design plays an important role in improving the cycling performance of the cell. Due to the highly reactive nature of sodium, reaction between sodium and sulfur would be stronger compared to lithium and sulfur, indicating that cathode materials having stronger interaction with sulfur to hold PS species should be applied in Na-S cathode. Microporous carbon materials are thought to provide the strongest physical confinement/immobilization for sulfur and its reduction products due to their extremely small pore sizes. This material has been successfully applied in Na-S cathode with lower sulfur loadings (32 %)[48]. Increasing sulfur loading in microporous carbon need special design in porous carbon host, such as homogeneous pore size distribution and increased pore volumes[93]. We applied a facile synthesis of microporous carbon polyhedrons (MCPs) using unique chemically and thermally robust and highly porous zeolite-type MOF (ZIF-8) rhombic dodecahedra as both the template and precursor, and use them as host to incorporate sulfur for Na-S battery cathode. The as-prepared MCPs show very high surface area and uniform microporosity, which can facilitate Na^+ transport and immobilize sulfur inside the pores homogeneously.

The composite MCPSs are prepared based on the reported method[19, 94]. Figure 24a shows the STEM and TEM images of the MCPs, indicating a uniform microporous spongy like texture. The abundant micropores give rise to a high Brunauer–Emmett–Teller (BET) surface area of 833 m^2/g calculated from the N_2 adsorption-desorption isotherm of the MCPs (Figure 24b and Table 3), which also give rise to a 708.5 m^2/g microporous surface area and pore size distribution ranging

from 0.4 nm to 1.8 nm. Different amount of sulfur is infused in MCPs and the composites are denoted as MCPS1 and MCPS2 with 47 % and 65 % sulfur loading respectively (verified by TGA curve Figure 25). The weight loss for MCPS1 due to the evaporation of sulfur occurs in a wide temperature range up to 450 °C, indicating strong nonpolar interaction between sulfur and carbon matrix, while MCPS2 shows a two-step weight loss, representing sulfur vapor outside and inside the MCPs respectively. SEM image (Figure 24c) of the as-synthesized MCPS suggests well-maintained rhombic dodecahedra morphology from ZIF-8 after carbonization and after sulfur infusion process, most of sulfur is trapped inside the micropores. Raman spectra (Figure 24d) of MCPs and MCPSs indicate carbonization of ZIF-8 and good dispersion of sulfur in micropores in MCPS1 as no crystalline sulfur peaks can be observed.

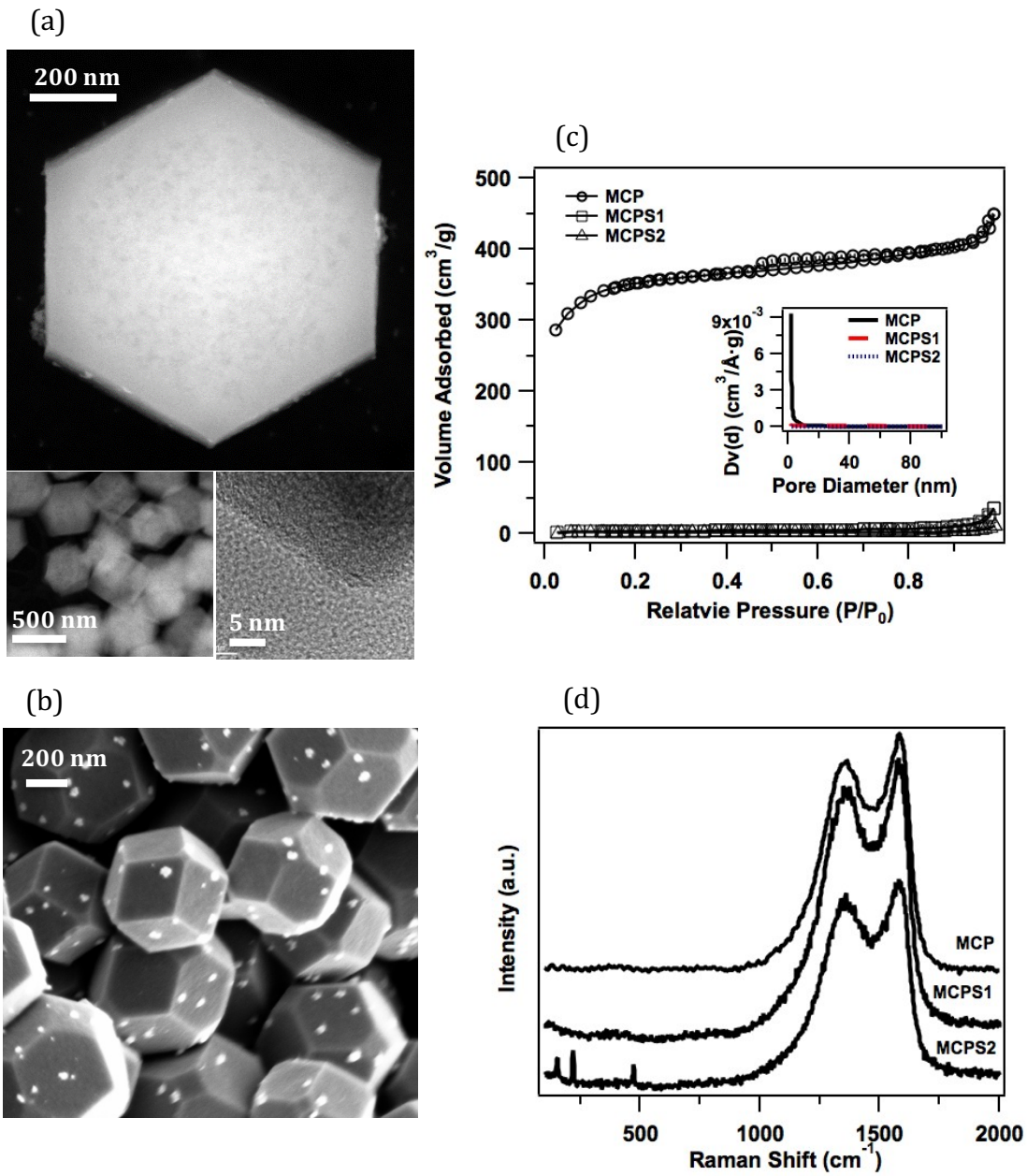

Figure 24: a, Scanning transmission electron microscopy (STEM) and transmission electron microscopy (TEM) images of MCP. The right bottom TEM image shows the edge of the MCP, indicating uniform porous structure of the MCP. b, Scanning electron microscopy (SEM) image of MCPS1. The small dots on the surface of the MCPS1 are trace amount of sulfur. c, N_2 adsorption–desorption isotherm and the corresponding BET pore size distribution (inset) of MCP and MCPS composites. d, Raman Spectra of the MCP and MCPS composites.

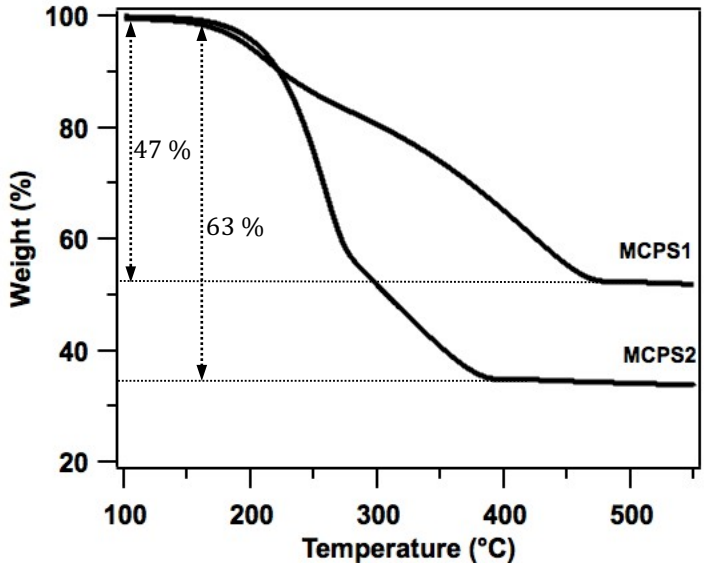

Figure 25: Thermogravimetric analysis (TGA) of the MCPSs with different sulfur loadings under N_2 flow.

Table 3: Physical characteristics of the MCP and MCPS composite. DFT: Density function theory method used to determine microspores. I_g/I_d is the ratio used to determine the amount of graphitic carbon verse disordered carbon in the composite, which are the normalized peak ratio of G band to D band in Raman Spectra.

Samples	BET Total Surface Area (m^2/g)	Pore Volume (cm^3/g)	Micropore Surface Area (m^2/g)	DFT Pore Size Distribution (nm)	Conductivity (S/cm)	I_g/I_d
MCP	833.3781	0.695505	708.4812	0.4~1.8	$9.66*10^{-3}$	1.14
MCPS1	11.5262	0.054189	2.3499	n.a.	$6.13*10^{-3}$	1.14
MCPS2	3.2628	0.017352	1.1322	n.a.	$5.22*10^{-3}$	1.08

Galvanostatic cycling performance of the cell by using a MCPS1 as cathode, a Na metal foil as anode and a carbonate electrolyte is shown in Figure 26a. The cell exhibits a high initial discharge

capacity of 1614 mAh/g at a current density of 0.1C (1C = 1675 mAh/g). The dimple and the lower voltage plateau at the beginning of discharge compared to the following cycles indicates that Na ions need to go through a barrier which is probably related to desolvation or solvation shell distortion[95, 96] to accommodate extremely small pore size in order to diffuse inside the micropores. This higher irreversible capacity is partially attributed to initial SEI formation and electrolyte decomposition. The reversible discharge plateau in the following cycles ranges from 1.6 V to 1 V. The lower voltage suggests formation of Na_2S/Na_2S_2 directly without intermediate soluble PSs species, while higher order NaPSs may formed and react with carbonate electrolyte when MCPS2 is used as cathode (Figure. 27). A reversible discharge capacity of 800 mAh/g is stably achieved for 50 cycles (Figure 26b). For comparison, a TEGDME electrolyte, which has high solubility for NaPS is applied and shuttling is observed by post mortem study (Figure 28 and 29). To investigate reduction and oxidation mechanism, cyclic voltammgram at various scan rates are conducted and shown in Figure 26c. Two reduction peaks are observed, indicating a two-electron reduction. The reduction peaks shift towards a more negative value and oxidation peak shift towards a more positive value with increasing scan rate, indicating a mixed kinetics of charge transfer process and diffusion of electro-active species control[97]. The peak current is found to increase with scan rate as well, which shows a linear growth with square root of scan rate (Figure 26d), suggesting a diffusion process. Furthermore, the almost the same cathodic and anodic peak currents indicates good reversibility and similar reaction mechanism occurring during charge and discharge.

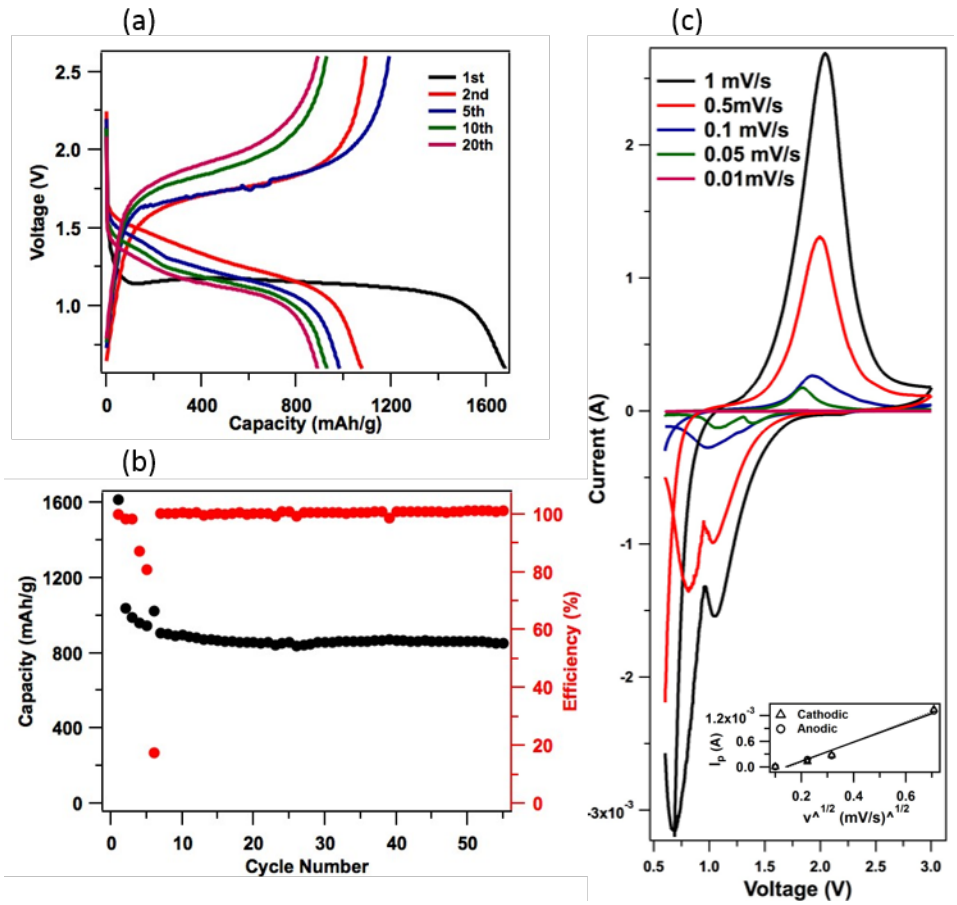

Figure 26: a, Electrochemical discharge and charge curves of the cell at various cycles. The tests were performed at 0.1 C for both charge and discharge in the potential range of 0.6–2.6 V vs Na/Na^+. b, Capacity and Coulombic efficiencies versus cycle number for the cell. c, Cyclic voltammograms (CV) of the Na-S cells at various scan rates. d, Relation between peak cathodic and anodic currents verse square root of scan rate derived from c.

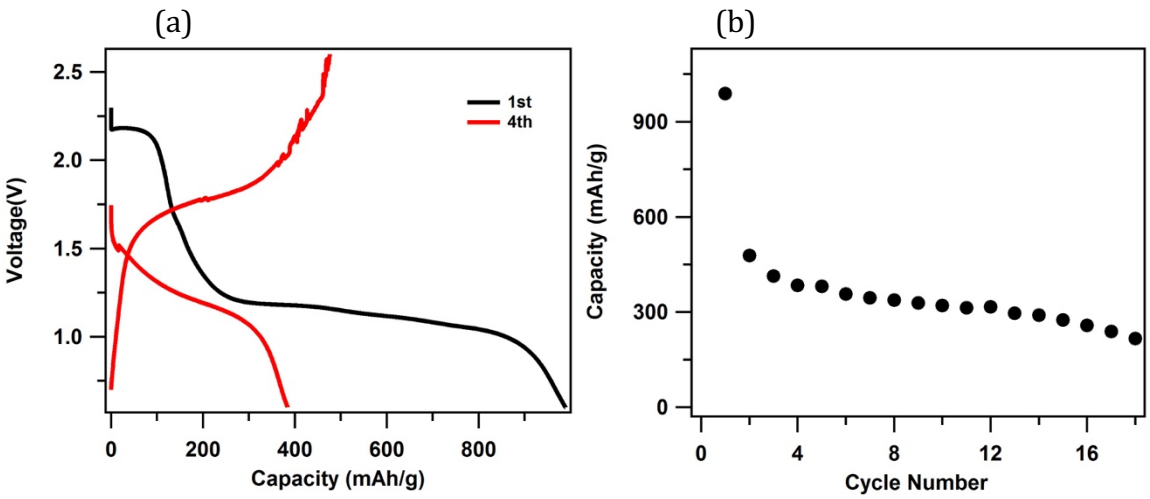

Figure 27: a, Electrochemical discharge and charge curves of the cell at 0.1C. The two-discharge plateau in the first cycles indicates sulfur outside and inside the MCP. The disappearance of the higher discharge voltage plateau suggests that the elemental sulfur outside MCP reacts irreversibly with carbonate electrolyte. b, Capacity verses cycle number by using MCPS2 as the cathode.

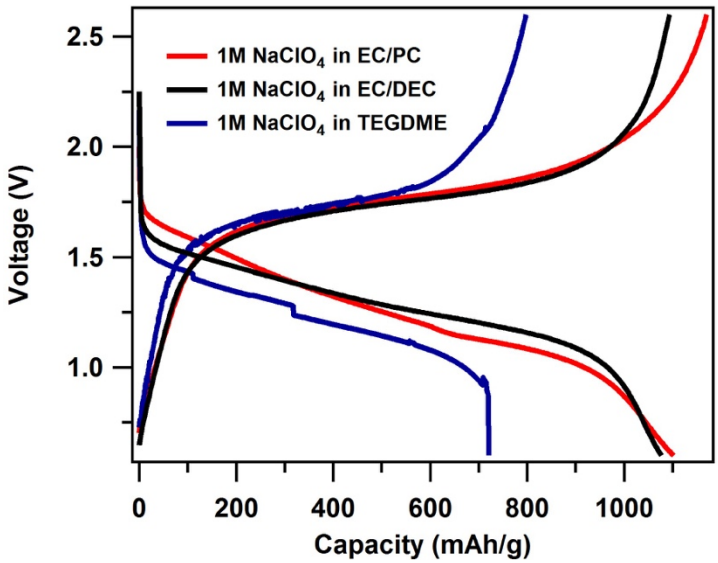

Figure 28: Tetraethylene glycol dimethyl ether (TEGDME) is a commonly used ether-based electrolyte in Li-S batteries due to its higher solubility to LiPS, however, carbonate electrolytes are suggested to be non-solubility to PS. The cathode is MCPS1. When usin MCPS2 as cathode in TEGDME electrolyte, server shuttling is observed during charging. The current density is 0.1C for both charge and discharge.

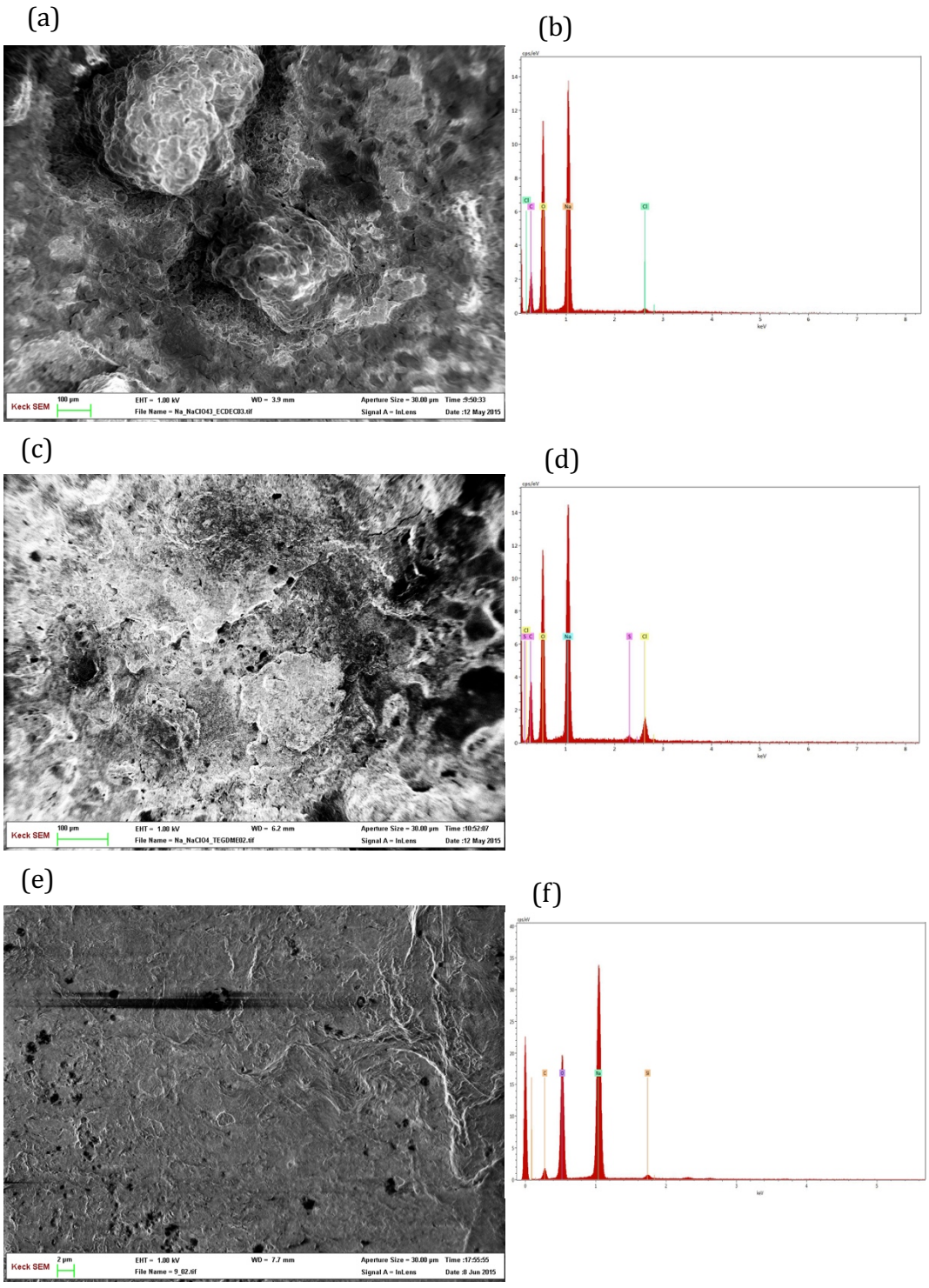

Figure 29: Scanning electron microscopy (SEM) image and energy dispersive spectra (EDS) maps of the sodium anodes after 10 cycles. a and b, SEM image and EDS maps of the sodium anode in

80 μL 1M NaClO4 in EC/DEC electrolyte. c and d are in 80 μL 1M NaClO4 in TEGDME electrolyte. e and f are in 1M NaClO4 in EC/PC electrolyte with 10 vol% SiO_2-IL-ClO_4. The cells were dissembled after 10 cycles of charge and discharge at 0.1C in an argon filled glovebox and the anodes were washed with electrolyte solvent before characterization.

However, we found that, although the battery can cycle stably in the above-mentioned system, instable charging is noticed at the sixth cycle and even worse at higher current density. This may cause dendrite problem, short circuit induced safety issues, low material utilization and electrolyte decomposition, eventually the cell failure. Therefore, a stabilizer in the electrolyte is necessary for the cell. We applied SiO_2-IL-ClO_4 nanoparticles as additives to stabilize the electrolyte and protect sodium metal as indicated in electrolyte stability analysis previously.

We next add either 5 vol% or 10 vol% of the SiO_2-IL-ClO_4 in the electrolyte as a stabilizer and performed the galvanostatic test at 0.5 C. As expected, even as little as 5 vol% additives could stabilize charging to a large extent. Figure 30a and b show the voltage profile and cycling stability of the cell. The first discharge is performed at 0.1 C to fully activate the electrode. A discharge capacity of around 750 mAh/g is achieved initially and maintained to 600 mAh/g at the 100^{th} cycle, indicating a small capacity decay of 0.31 % per cycle, which is comparable to current Li-S batteries at the same C rate. The Coulombic efficiencies for the batteries with and without SiO_2-IL-ClO_4 are compared in Figure 30c and e to evaluate the stability of the systems. We have seen that, the cell without SiO_2-IL-ClO_4 show diverged Coulombic efficiency from 10^{th} to 60^{th} cycle, while cells with only small amount of SiO_2-IL-ClO_4 can improve the Coulombic efficiency to over 90 % each cycle, which is enhanced with increasing SiO_2-IL-ClO_4 amount. This improved stability can also improve the cycling discharge capacity as shown in Figure 30d because less side like electrolyte decomposition reaction is occurring.

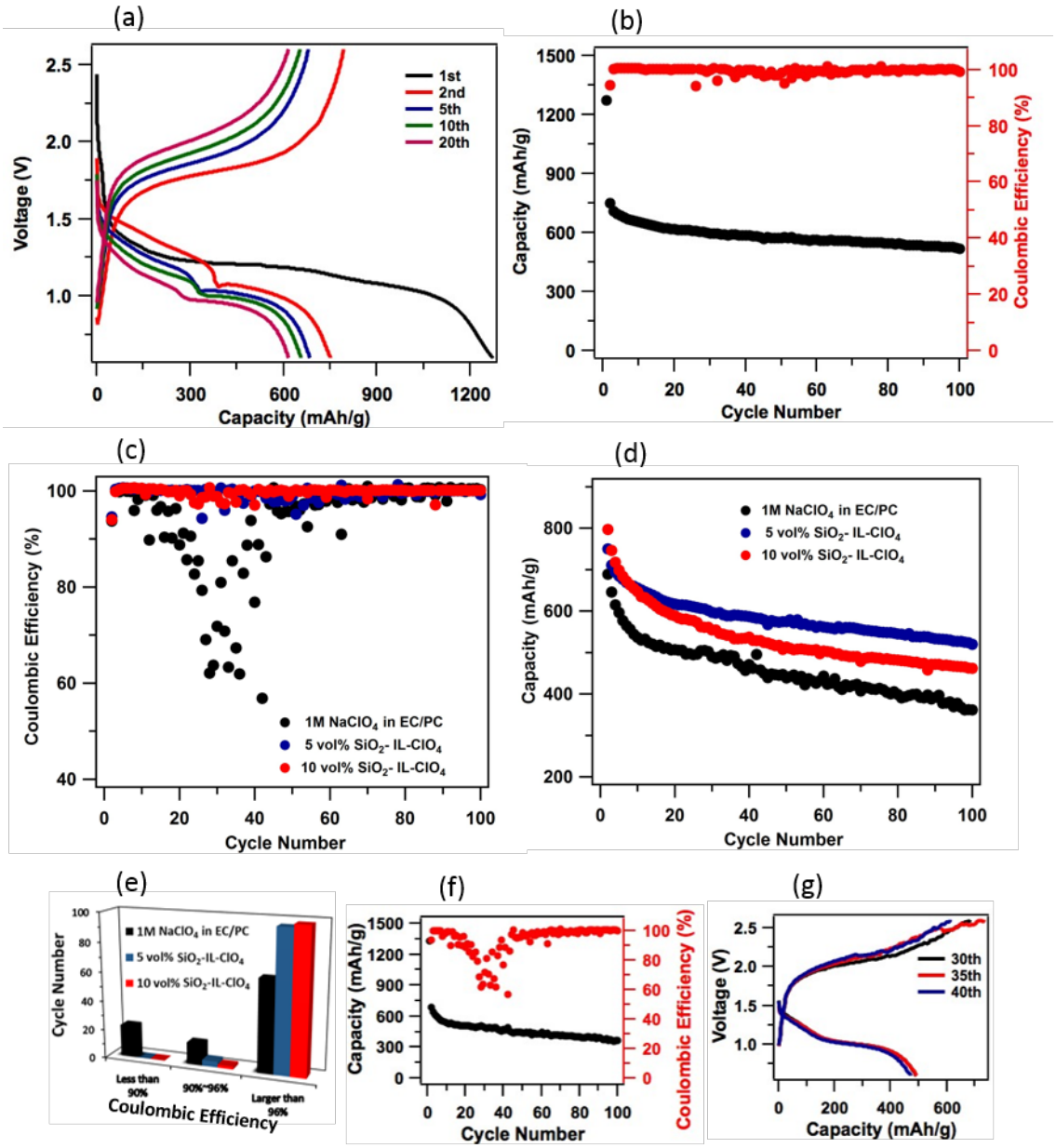

Figure 30: Galvanostatic cycling performance of the Na-S cell in a carbonate electrolyte with different amount of SiO_2-IL-ClO_4. a, Electrochemical discharge and charge curves of the cell at various cycles with 5 vol% of SiO_2-IL-ClO_4 in the electrolyte. The tests were performed at 0.1 C for the first discharge and 0.5C for the following cycles in the potential range of 0.6–2.6 V vs Na/Na^+. b, Capacity and Coulombic efficiencies versus cycle number for the cell in a. c and d, Coulombic efficiency and capacity versus cycle number for the cell with different amount of SiO_2-IL-ClO_4 in the electrolyte respectively at 0.5C. e, Electrolyte stability analysis for the three cases in c in term of Coulombic efficiency. f and g, cycling stability and voltage profile of the cell

without SiO_2-IL-ClO_4 in the electrolyte at 0.5C.

To investigate the discharge reaction mechanism, X-ray photoelectron spectroscopy (XPS) is applied on the cathode side after galvanostatic cycling at different stages study the species formed at each stage (Figure 31a). The pristine cathode exhibits an elemental-state sulfur doublelet with S2p 2/3 at 164 eV. When cell is discharged below 1 V, S2p 2/3 peaks at 162.1 eV and 160 eV representing Na_2S_2 and Na_2S rise. The peak beyond 166 eV is probably due to thiosulfate/sulfate complex species originating from oxidized sulfide species[98]. Upon fully discharge, elemental sulfur peak disappeared; only the sulfide peaks remain, suggesting the final discharge product of Na_2S. This can explain why the higher capacity is achieved compared to high temperature Na-S batteries, where the final discharge product is Na_2S_x ($x \geq 3$) because of the phase limitation[47]. To further understand the reaction mechanism, the energy dispersive X-ray (EDX) analysis of cathode after full discharge was performed (Figure 31b), the atomic ratio between Na and S is about 2: 1, indicating almost fully reduction from S to Na_2S. UV-vis spectra of a dilute Na_2S_6 solution, battery cathode cycled in TEGDME and carbonate electrolyte soaked in TEGDME are shown in Figure 31c. In carbonate electrolyte, there are only insoluble S_2^{2-} or S^{2-} formed, while high order soluble PSs are formed when the cell are cycled in TEGDME. This again confirms that MCPS cathode coupled with carbonate electrolyte undergoes solid-state reaction with no soluble intermediated soluble polysulfide formed in Na-S batteries.

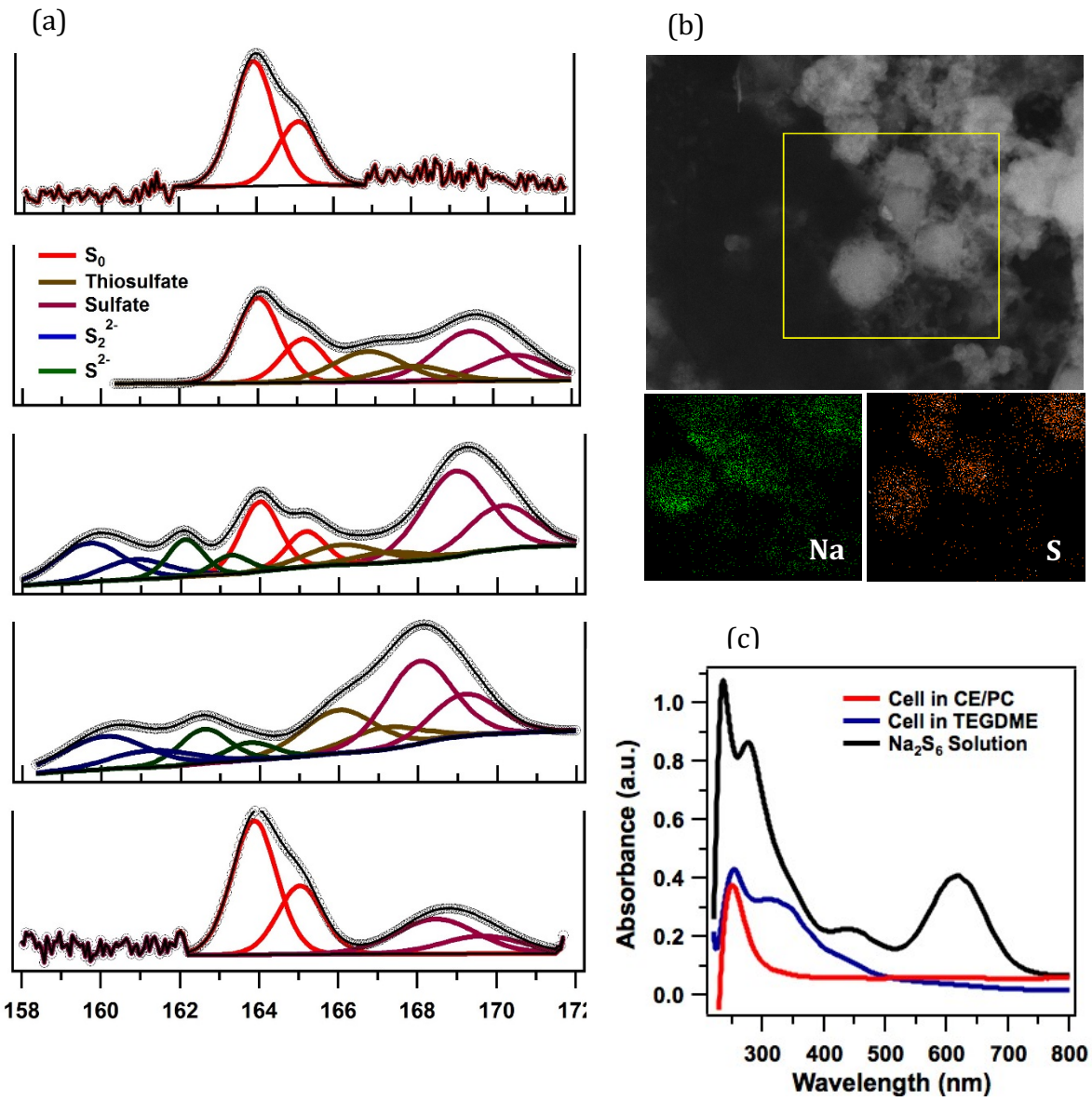

Figure 31: Post mortem characterization of the MCPS1 cathodes in carbonate electrolytes. a, Ex situ XPS spectra of S 2p in MCPS cathodes at pristine and different cycling states in a carbonate electrolyte. (From top to bottom: pristine cathode, cell was discharged to1.4 V, 1 V and 0.6 V and was recharged to 2.6 V at the first cycle respectively). Cathodes were disassembled in an argon filled grove-box and washed with electrolyte solvent before characterization. b, STEM image and EDX maps of the MCPS1 cathode after first discharge. The cathode was washed with electrolyte solvent and sonicated to form a homogeneous suspension in a sealed vial and then transferred to a Cu grid sample holder. c, UV-vis spectra of the cathodes solutions cycled in different electrolytes after 10 cycles at 0.1C. The MCP cathodes cycled in different electrolytes were all soaked in 2 mL TEGDME for 4 days to extract PS species. For the Na_2S_6 solution, 1M Na_2S_6, which is synthesized by mixing Na_2S and sulfur in a stoichiometric ratio of 2:6 in TEDME. It was diluted 200 times and

subjected to test. Peak assignment: S^{2-} ,S_2^{2-}: 260 nm, S_6^{2-}: 340 nm and 450 nm, S_3^{2-}: 330 nm, $S_3^{\cdot-}$: 610 nm[99].

Based on the spectroscopic study above, we suspect that the electrochemistry on cathode side is occurred inside the MCPS only, indicating a solid-state reaction. To verify this, we approximate Na^+ diffusivity into the cathode based on electrochemical data. A galvanostatic intermittent titration technique (GITT) was performed by discharging the cell for 30 minutes at 0.1C followed by a 10-hour relaxation (Figure 32a). The diffusion coefficient (Figure 32b) during reversible charging and discharging can be calculated by the equation developed by Weppner and Huggins[100], which is in the range of solid-state diffusion. It is found to be the lowest at the plateau region, indicating a kinetics-controlled mechanism is simultaneously occurring. In addition, the equilibrium potential determined at the end of each titration step changes very slightly and all below 2 V, suggesting the formation of Na_2S_x ($x \leq 2$). This can also be verified by deriving diffusivity from Warburg element of a fitted equivalent circuit from the electrochemical impedance spectra (Figure 33). The calculated diffusivity shows the similar order of magnitude compared to that derived from GITT. The reason that in solid-state reaction occurs only in microporous carbons with extremely small pore size but no other carbon materials is probably due to that interaction between sulfur/sulfur species in the carbon is much stronger than the strength for sulfur/sulfur species solvation due to their poor solubility in carbonate electrolytes[101] and space confinement in carbon.

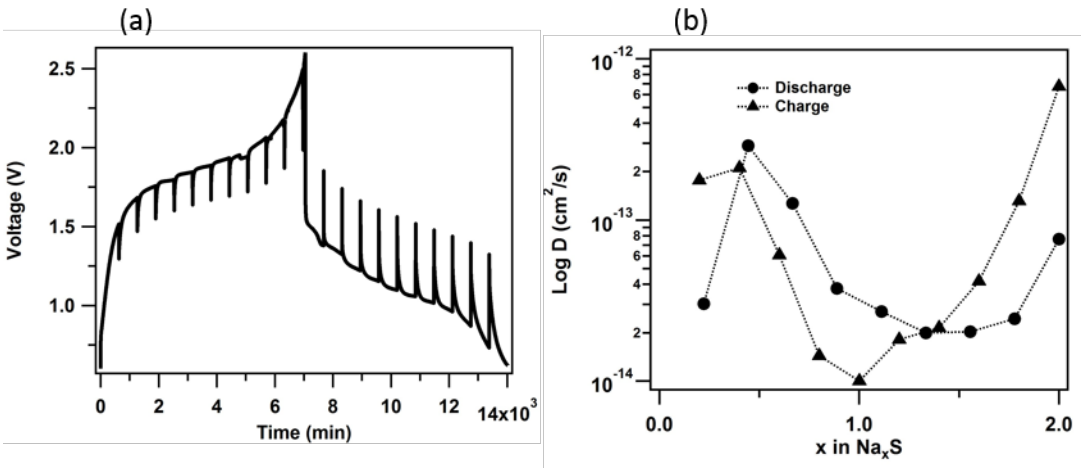

Figure 32: Diffusivity analysis of the Na-S cell. a, GITT curves of MCPS1 in EC/PC electrolyte and b, Diffusion coefficients derived from a.

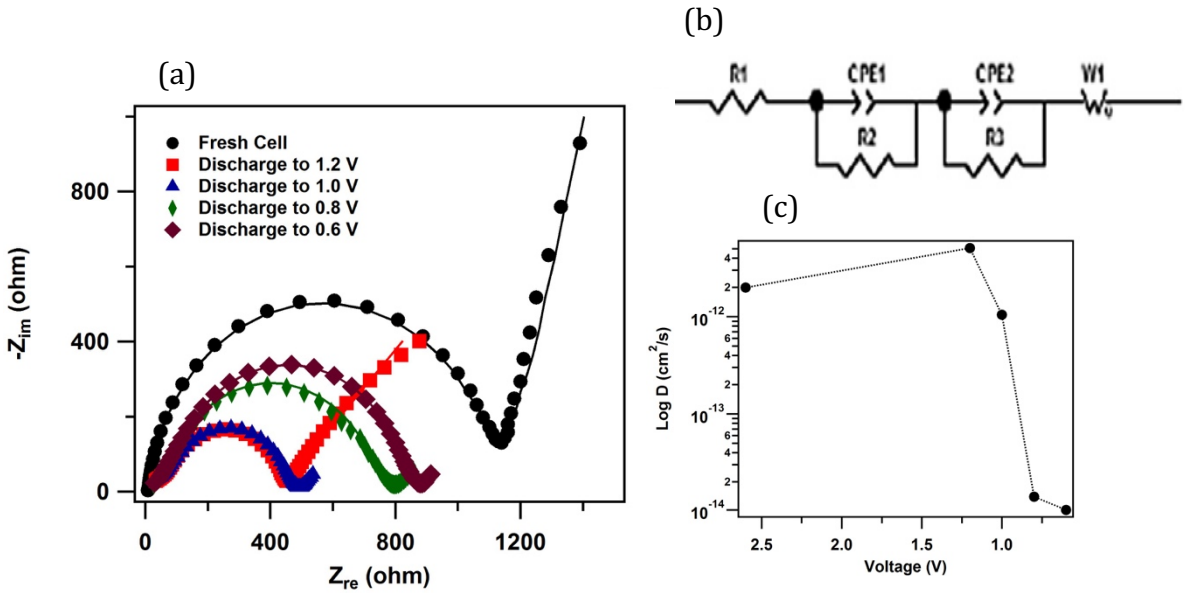

Figure 33: Impedance spectra a and derived diffusivity c of the MCPS1 cathode at pristine and different stages of discharge. b, equivalent circuit used to fit impedance spectra and to get Warburg element. The black like in a is the fitted impedance spectra by applying the circuit in b.

3.3 CONCLUSION

In conclusion, we constructed a stable cycling room temperature Na-S battery. The micoporous carbon sulfur composite provides strong physical confinement to ensure reaction to happen in all-solid state when coupled with non-solvent electrolyte for PSs. The unique small porous carbon shows strong affinity towards sulfur and can probably direct sulfur to exist in an unusual phase and avoid formation of high order PS during discharge. We use both spectroscopic and analytical tools to verify that the reaction occurs all inside the microporous carbon composite. The cell can cycle stably for over 100 cycles when adding SiO_2-IL-ClO_4 particles at a relatively high current density (0.5C), where the particle additives is seen to serve as a stabilizer to protect sodium metal and prevent dendrite formation through chemically deposition of a stable SEI layer as well as physically reducing electrical field by increasing the length scale to the size of particle and increase viscosity of the electrolyte. Our finding underscores the benefits of micorporous carbon-sulfur composite and nanoparticles for gridding new material designs for inexpensive rechargeable metal-sulfur batteries. Further investigations are needed to fully understand the effect and interaction of microporous carbon and sulfur species as well as the functionality of SiO_2-IL-ClO_4 on metal anode protection.

3.4 METHODS

Materials Synthesis: MCPS and SiO_2-IL-ClO_4 electrolyte were synthesized according to the previous methods with modifications[19, 102]. Briefly, the synthesis of MCPS is the same except the final sulfur infusion step. A sealed Pyrex tube was used to hold samples and a ramp rate of 1 ºC/min was used for both heating and cooling. The final mass fraction of sulfur in the composites was determined by TGA (Q5000 IR Thermogravimetric Analyzer). The synthesis of SiO_2-IL-ClO_4

was the same as well except the anion exchange step. In this work, $NaClO_4$ was used to as anion exchange source.

Material Characterization: The morphology and elemental mappings of the materials were studied using a FEI Tecnai F20 Transmission Electron Microscope and A LEO 1550 high resolution scanning electron microscopy. The nitrogen adsorption-desorption isotherms of the MCP and MCPS were obtained with a Brunauer-Emmett-Teller (Micromeritics ASAP2020). Raman spectra were collected using a Renishaw InVia Confocal Raman Microscope (λ= 488nm). UV-vis spectra were collected by Shimadzu UV-Vis-NIR Spectrometer. X-ray photoelectron spectroscopy (XPS) measurements were performed with a Surface Science SSX-100 spectrometer using a monochromatic Al Kα source (1486.6 eV). Non-linear least squares curve fitting was applied to high-resolution spectra, using CasaXPS software.

Electrochemical Measurements: The cathodes were prepared with MCPS1 or MCPS2, carbon black (Super-P, TIMCAL), and polymer binder (poly (vinylidene difluoride), PVDF, Aldrich) in a weight ratio of 8:1:1. A carbon-coated aluminum foil (0.004 in thick, MTI Corp.) was used as the current collector. The typical thickness of the active material film is ~20 μm. Sodium foil (Alfa Aesar) was used as the counter and reference electrode. A glass fiber filter paper (Watchman 934-AH) was used as separator. 80 μL 1M Sodium perchlorate in a mixture ethylene carbonate (EC) and diethyl carbonate (DEC) (v:v = 1 :1) or in tetraethylene glycol dimethyl ether (TEGDME) or in a mixture of EC and propylene carbonate (PC) (v:v = 1 :1) with different amount of SiO_2-IL-ClO_4 were used as electrolyte for the cells. Cell assembly was carried out in an argon-filled glove-box (MBraun Labmaster) by using coin cell 2032 type. The room-temperature cycling characteristics of the cells were evaluated under galvanostatic conditions using Neware CT-3008

battery testers and electrochemical processes in the cells were studied by cyclic voltammetry using a CHI600D potentiostat. Electrochemical impedance and floating tests were conducted by using a Solartron Cell Test System model 1470E potentiostat/galvanostat. Ionic conductivities were measured using a Novocontrol N40 broadband dielectric spectrometer.

For post-mortem studies, cells were disassembled in an argon-filled glove-box and the electrodes were harvested and rinsed thoroughly with the electrolyte solvent before analysis.

4 HIGHLY STABLE SODIUM BATTERIES ENABLED BY FUNCTIONAL IONIC POLYMER MEMBRANES

4.1 INTRODUCTION

Secondary sodium-ion and sodium-metal batteries offer multiple advantages over the lithium counterparts for portable storage in electric vehicles and locomotives as well as for stationary storage in power stations.[103-107] Motivation for current research interest in this technology comes from multiple sources, including the lower cost and high natural abundance of sodium, the high theoretical capacity (1166 mAh/g) and moderate redox potential (-2.71 V versus the standard hydrogen potential) of the sodium anode, and the fact that high-temperature sodium-sulfur (Na-S) and Na-metal chloride ($Na/MeCl_2$) batteries have already been demonstrated to be commercially viable technologies for grid storage and for electrification of transportation. On-field accidents and difficult maintenance of these batteries due to their high operating temperature are a concern for broader deployment in portable devices, robotics, and electric vehicles.[2, 47] Room-temperature sodium batteries based on high-voltage intercalation cathodes[106, 107] or energetic conversion cathodes (e.g. Na-S or $Na-O_2/CO_2$ cells[82, 83, 104, 108, 109]) have already been reported to overcome some of these difficulties, [106] however the intense focus on improvements afforded by ambient-temperature operation, typically gloss over fundamental challenges associated with long term stability of a sodium metal anode in liquid electrolytes .

Recharge of any battery utilizing a sodium metal anode requires repetitive stripping and platting of the metal surface. The size difference between sodium ions and sodium atoms subjects the anode to large volumetric and morphological changes during normally battery cycling, which makes the batteries unstable to failure by multiple processes.[83, 92] First, because of its high reactivity,

metallic sodium rarely forms stable solid electrolyte interphases (SEIs), rather it is corroded continuously by aprotic liquid electrolytes upon cycling, which lowers Coulombic efficiency (CE) and lifetime of the cells.[110] Second, because of the uncontrolled nature of the SEI formation reactions, significant spatial variations in conductivity of the SEI exist, which drive spatial variations in Na deposition rate during battery recharge making the metal particularly unstable towards the morphological instability known as dendritic electrodeposition.[111] Finally, because of the metal's softness and low melting point, dendrite induced short circuits either end in thermal run-away events or in sodium dendrites breaking away from the metal electrode to become electrochemically disconnected from the metal substrate, creating sections of inactive/orphaned sodium, which shorten the lifetime of the cell.

We herein report on the synthesis, chemistry and interfacial properties of ionic liquid membranes created as SEI films formed directly on metallic sodium by electropolymerizing functional ionic liquid monomers in liquid electrolytes. It is found that such membranes markedly increase the stability of sodium anodes to failure. We also find that unlike Li anodes which can fail by any of the three processes discussed above, Na anodes almost always fail as result of electrolyte degradation. Our focus on artificial SEI membranes based on ionic liquids (ILs) is motivated by several considerations, including the large number of previous works which show that some IL chemistries exhibit exceptional chemical and electrochemical stability in contact with reactive metals.[90, 91, 104, 111-113] Additional motivation comes from recent studies which report that electrolytes in which ILs are used as additives in conventional aprotic liquid electrolytes are able to stabilize lithium metal anodes against dendrite formation, in some cases producing ten-fold or higher increases in cell lifetime. [6-7] Theoretical work by the Archer group suggest that the tethered

anions in an IL can improve the stability of Li plating during the battery recharge by acting as a supporting electrolyte.[114, 115] This theory has been verified by the experimental studies which show that dendrite free electrodeposition can be achieved by uniforming ion distribution by contacting lithium to functional glass fiber or solid polymer electrolyte.[116-118] The IL additive is thought to reduce the magnitude of destabilizing electric fields near the anode[114, 115, 119] by providing a localized supply of anions able to support a high cation flux at the electrode. Recent works from the same group show that the effect is not limited to Li. Carbonate based electrolyte containing around 5 to 10 vol% 1-methyl-3-propylimidazolium-chlorate tethered to SiO_2 nanoparticles were shown to enhance the stability and cycle life for both Na-S and Na-O_2/CO_2 cells.[104, 108] Here we employ an in-situ electropolymerization able to create thin-film membranes of oligomeric ILs from functional imidazolium based ionic liquids containing allyl or vinyl groups.

4.2 RESULTS AND DISCUSSION

4.2.1 Polymeric ionic liquid film formation and characterization

Electrochemical polymerization of reactive monomers on metallic surfaces is a well-established method to fabricate functional polymer thin films for protecting metals [10] and electronic devices, including sensors.[120]] The approach offers several advantages over other polymerization techniques that may also be used to create coatings on metals: (i) It combine polymer synthesis with thin film formation; (ii) It eliminates the need for exogenous oxidants to initiate the polymerization; and (iii) important properties of the membrane, including its thickness, morphology, and porosity are controlled by transport processes in the film itself [121]. Although the method has not been previously studied to protect reactive alkali metals for battery applications, it is well suited to this application because the transport processes that controll film

thickness and morphology are related to those that controll access of ions to/from the metal surface during charge/discharge processes in a battery. Figure 34A is a schematic representation of the process, showing how it can be used to create an ionic polymer membrane on the surface of a sodium anode. The polymerization reaction is believed to progress via the usual steps (initiation, propagation, and termination) that govern free radical polymerization processes. Initiation occurs during charging, wherein the unsaturated ionic liquid monomers accept electrons to form reactive radical species. These species react with monomers to increase the size of the radicals, propagating the polymerization process and creating a thin, porous film in conformal contact with the electrode. Termination requires collision of two growing radicals or collision between a radical species and solvent molecule; here we eliminate the latter possibility by performing the reaction in the pure liquid IL monomer.

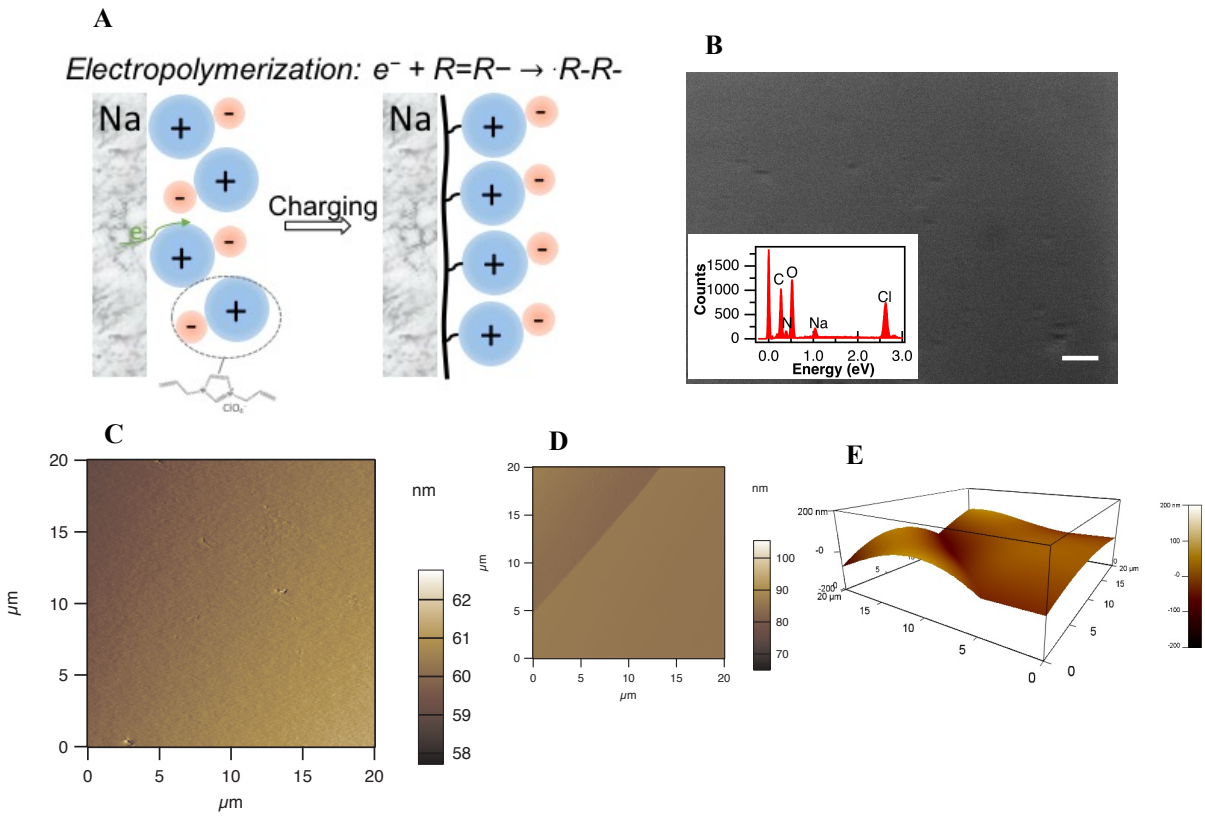

Figure 34: Formation of polymeric ionic liquid film. A. A schematic drawing of the polymeric ionic liquid film formation on the electrode. The cations bearing unsaturated compound accept electrons from the electrode during charging and form free radicals. These radicals will initiate and propagate the polymerization process and form polymer film on the electrode surface. B. SEM, EDS mapping and C. AFM height image of the stainless-steel electrode covered by the polymeric film formed by 1,3-diallyl imidazolium perchlorate (DAIM) under constant current of 1 mA/cm^2 (Scale bar: 20 μm). D, E, Amplitude and the relevant 3-D height AFM images of the same film covered on the stainless-steel electrode in B and C.

The molecular structure of the IL monomer was found to be an important factor in regulating the structure and morphology of the electrodeposited polymer membrane as well as the degree of polymerization achieved.[122, 123] This opens opportunities for development of new task-specific IL monomers for the intended purpose. Ohno has argued that polymerization of IL molecules may result in degradation of properties of the monomers, including ionic conductivity, due to elevation

of the glass transition temperature and reduced number of mobile ions after covalent bonding of the component ions.[124, 125] In order to achieve optimized adhesion and ionic conductivity, different functional imidazolium cation- based ionic liquid monomers bearing allyl or vinyl group and perchlorate anion, namely 1-allyl-3-methylimidazolium perchlorate (AMIM), 1,3-diallyl imidazolium perchlorate (DAIM), 1-allyl-3-vinyl imidazolium perchlorate (AVIM) were synthesized, and their electroinitiated polymerization process on the electrode surface was investigated. To characterize the polymeric film formed on the electrode, the monomers were dropped on a polypropylene separator sandwiched by two stainless steel electrodes in a coin cell. A constant current of 1 mA/cm^2 was applied to the cells to initiate polymerization until the voltage goes diverging with no current passing through the cell (see Figure. 35), at which point the electrodes are probably covered by the films and completely insulated. The morphology of the polymer film was examined by scanning electron microscopy (SEM) as shown in Figure 34B and Figure 36. Both DAIM and AVIM monomers are able to be polymerized by charges with good adhesion and contact to the stainless-steel electrode, while AMIM barely forms a film on the surface dues to limited unsaturated components. A uniform thin, membrane was found to cover the rough and scratched surface of the stainless-steel electrode by polymerizing DAIM monomer. The surface topography of the film formed by DAIM was further characterized by atomic force microscopy (AFM) in tapping mode. Figure 34C represents a smooth and uniform height/topography image of the DAIM film on the stainless steel, which is comparable with the SEM image. To assess the thickness of the film formed on the electrode, a scratch was made to expose the stainless steel and allow measurement of the height from the stainless steel surface to

the upper polymer, giving a thickness of ~80 nm (Fig 34D and Fig 37).[126]

Figure 35: Voltage (A) and Current (B) -time profile during the electroinitiated polymerization process for the neat ionic liquid monomer in a coin cell with stainless steel electrode.

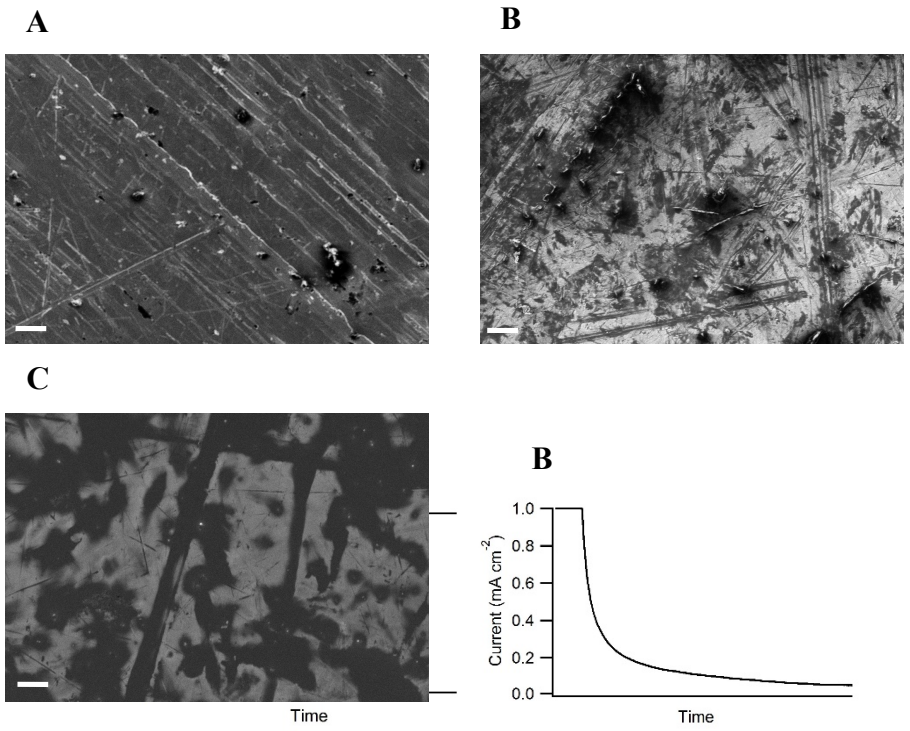

Figure 36: SEM images of the A neat stainless steel electrode, B, stainless steel electrode covered by polymerizing 1-allyl-3-methylimidazolium perchlorate (AMIM), C, stainless steel electrode covered by the polymeric film formed by 1-allyl-3-vinyl imidazolium perchlorate (AVIM) under a constant current of 1 mA/cm^2 (scale bar: 20 μm).

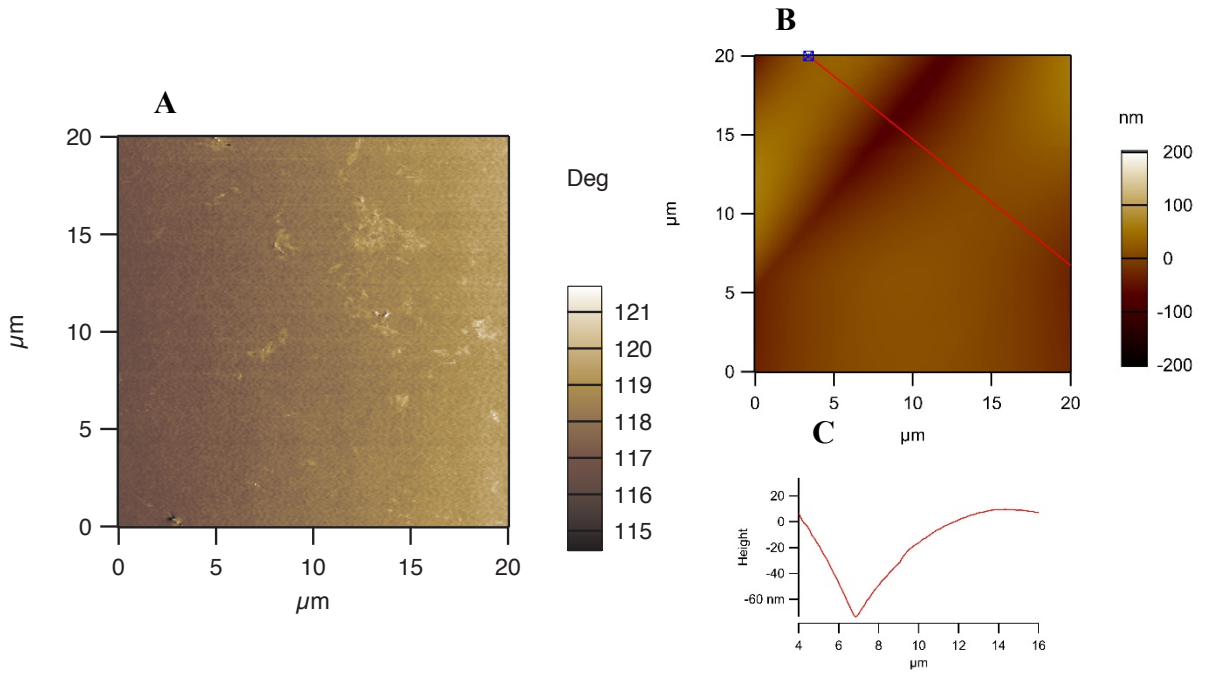

Figure 37: A. AFM phase image of stainless steel electrode covered by the polymeric film formed by 1,3-diallyl imidazolium perchlorate (DAIM). B AFM height image and the corresponding height profile (C) along the red line of the same material in A.

The molecular weight (M_w) and polydispersity index (PDI) of the electropolymerized IL films were determined by means of gel permeation chromatography (GPC) and the results are reported in Table 4. Under the conditions studied here, AMIM forms oligomers (possibly due to the limited unsaturated double bonds), while DAIM and AVIM monomers were capable of forming large molecular weight polymer films, consistent with the film morphologies characterized by SEM. Due to the existence of sp^2 hybridized vinyl group in AVIM, this monomer is very reactive and self-polymeriable in the presence an initiating moiety,[127] leading to much larger M_w, denser memebrane films than produced by electropolymerization of DAIM. Thus, while membranes formed by DAIM are rubber-like with softer consistency and more open morphologies, those based on AVIM have molecular weight about twice as large and less open morphologies. Based on the

morphology and stability of the film formed, DAIM was selected for more indept studies. To create membranes suitable for electrochemical studies, DAIM monomer was used as additives in liquid electrolytes to form optimized passivation membranes in a variety of configurations on sodium metal anodes. For brevity, we here focus on membranes created in-situ on metallic sodium using 20 wt% of the IL monomer as an additive in an electrolyte comprised of 1 M sodium perchlorate in ethylene carbonate/properlynee carbonate (EC/PC-$NaClO_4$). The effect of the resultant coatings on stability of sodium metal metal anode is discussed in detail in the following sections of the paper.

Table 4: Molecular weight and polydispersity index of the electroinitiated polymer IL film analyzed by Gel permeation chromatography (GPC) in dimethylformamide.

Ionic Liquid Monomer	M_w [g/mol]	PDI
AMIM	896	1.024
DAIM	58540	1.546
AVIM	122100	1.248

4.2.2 Sodium metal stability

To evaluate the stability of the sodium metal anodes passivated with artificial SEI layers created by our functionalized IL membranes, the Coulombic efficiency (CE) of sodium stripping and platting processes was determined from galvanostatic experiments in a Na/stainless steel cell. Initially, a large amount of sodium (1 mAh/cm^2) was plated on the stainless-steel electrode at a constant current of 1 mA/cm^2. In the following cycle, a fraction (1/6) of the sodium was striped

and plated from the stainless steel repeatedly at the same current density (Figure 38A). Under these conditions, the CE can be calculated based on the simple formula proposed by Aurbach.[128] Control cells that do not contain IL monomer in the electrolyte, or which contain the unpolymerizable IL monomer 1-methyl-3-propylimidizolium chlorate (MPIM), were evaluated in the same manner and found to yield very low CE values around 16.7% and to fail within the first cycle for the cells with no IL in the electrolyte. This result is expected as the unpassivated sodium metal is expected to vigorously and irreversibly react with liquid electrolyte during electrochemical cycling. The low CE is also consistent with previous reports by Yui et al. [129] and Seh et al.[110] in cycling experiments in carbonate electrolytes in which all of the plated sodium was stripped from the stainless steel electrode each cycle. Consistent with the discussion in the introduction, the authors explain the low CE for sodium metal anodes in terms of formation of non-uniform solid electrolyte interphase as well as dendritic growth.

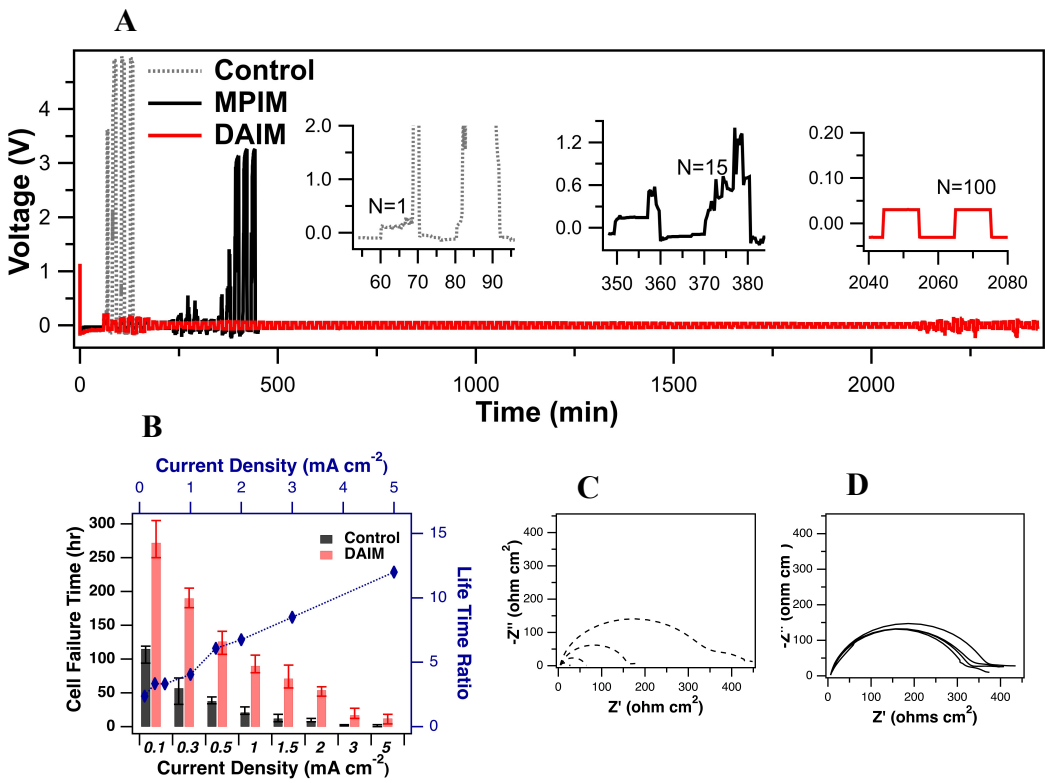

Figure 38: Electrochemical characterization of the stable SEI on the sodium metal anode. A. Voltage-time profiles of Na/Stainless Steel cells with different IL additives for the cycling efficiency calculation (the cells with DAIM can run stably for over 121 cycles). B. Cell failure time at various current densities derived from constant current polarization test of Na/Na symmetric cell with and without 20 wt% DAIM in the electrolyte. C and D, Nyquist plots for a Na symmetric cell after every 2-hour charging at 1 mA/cm^2 in the electrolyte without and with DAIM.

In contrast, electrolytes containing DAIM as an additive exhibit markedly improved Coulombic efficiency with values as high as 95.0 % measured at a current density of 1 mA/cm^2. Additionally, cells containing DAIM exhibit vastly improved stability in long-term cycling measurements and lower overpotential (Figure 39A) compared with those containing MPIM. It is important here to note that while MPIM additives in carbonate electrolytes were reported previously to prevent dendrite formation in lithium metal batteries[111], the material only has a limited effect in

improving the CE of the sodium metal anode, with only a 60 % CE being achieved. As the surface of the neat stainless steel electrode is relatively rough, this experiment tentatively confirms our previous argument that DAIM monomer helps form a uniform ion conducting polymeric membrane that not only protects the sodium metal surface, but facilitates transport at the anode.

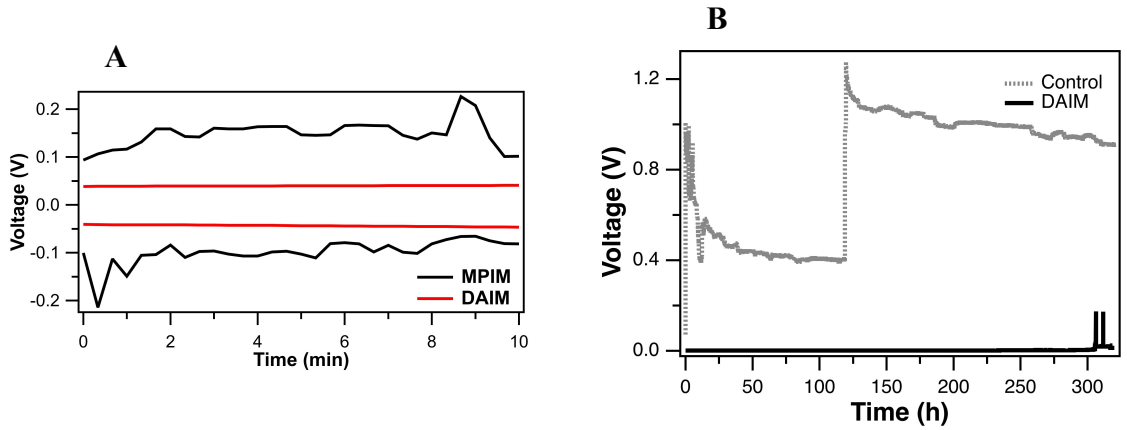

Figure 39: A. Voltage-time profile of a Na-stainless steel cell with 20 wt% DAIM and MPIM ionic liquid in electrolyte. B. Voltage-time profile of a Na symmetric cell with and without 20 wt% DAIM in electrolyte at a constant current of 0.1 mA/cm^2.

A more detailed assessment of the membranes was performed using an aggressive galvanostatic polarization experiment in Na/Na symmetric cells to study the role played by the as prepared membranes over a wider range of current densities. Figure 38B reports the cell lifetimes at various current densities in the two cases, with and without DAIM additive in the electrolyte. It is seen that the cell lifetime doubles at low current density and improves by at least a factor of three at higher current densities ($\geq$ 1 mA/cm^2). As important is our observation that unlike typical lithium metal anodes, wherein cell failure by internal short-circuit is evidenced by a large voltage drop during galvanostatic polarization,[90] failure of sodium anodes is almost always evidenced by a diverging voltage (Figure 39B), indicative of electrolyte degradation. Comparison of the voltage profiles at 0.1 mA/cm^2 (Figure 39B) shows a higher polarization voltage with fluctuations for the

cells in neat electrolyte, indicative of severe side reaction between sodium and electrolyte. The results reported here are to our knowledge the first to show that sodium metal cells are more likely to fail by electrolyte depletion than by dendrite-induced short circuits. This observation is thought to derive from the relative softness of metallic sodium (room-temperature hardness: 0.5 MPa & shear modulus: 3.3 GPa) relative to Li; [114, 130, 131]. It indicates that dendrite induced short-circuiting and associated phenomena such as thermal runaway is not as important for sodium metal battery technology as they are for Li metal cells, and provides insights into the role the IL membranes may play in stabilizing the sodium anode.

The stability of the Na/Na symmetric cell containing DAIM monomer additives in the electrolyte was also investigated by electrochemical impedance spectroscopy (EIS) experiments. To evaluate the interfacial reactivity of the sodium metal surface during polarization, impedance of the cells containing 0 or 20 wt% DAIM was measured as a function of time following intervals of two-hour charging at 1 mA/cm^2 (Figure 38C and D). The interfacial resistance was found to be unstable for the control cell, displaying erractic values and transients from measurement to measurement. In contrast, in the 20 wt% DAIM case, the interfacial resistance steadily increases, indicative the formation of a stable SEI layer. The electrochemical initiated polymerization process in the presence of sodium anode and electrolyte was further investigated by linear-sweep voltammetry (Figure 40). The oxidation currents after the breakdown voltage are seen to be much lower for IL containing electrolytes than for the control electrolyte, indicating that the IL containing electrolytes have better electrochemical stability than the neat liquid electrolytes.[132] It is also noted that small oxidization peaks were observed between 2 to 4 V for the electrolytes containing DAIM and AVIM, possibly indicative of an electron-transfer-induced polymerization process. The peak

current increases linearly with the increase of the root mean square of the scan rate, indicating a diffusion-limited controled polymerization process.[104]

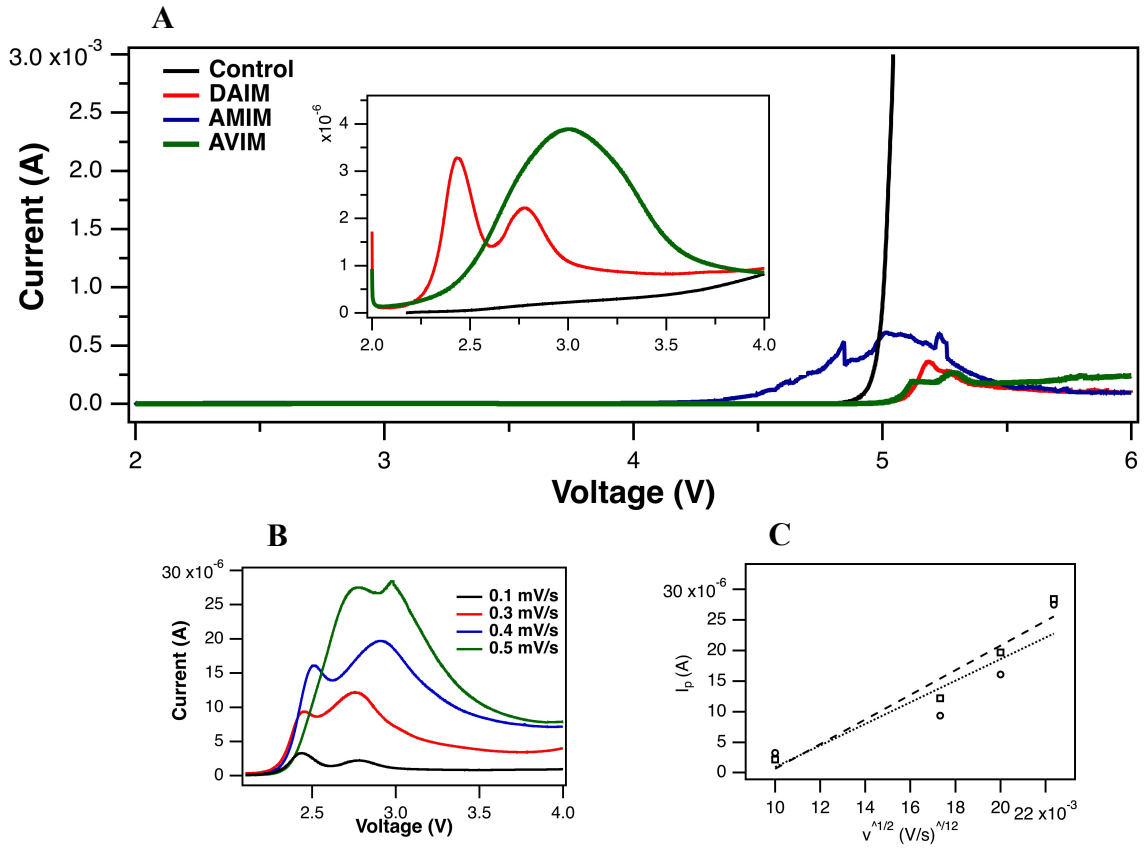

Figure 40: A. Linear scan voltammogram of the Na/Stainless Steel cell contain different types of IL additives in the electrolyte. Scan range: 2-6 V, scan rate: 0.1 mV/s. B. Linear scan voltammogram of the cell with DAIM additive in the electrolyte at different scan rate from 2 to 4 V. C. Peak current vs. root mean square of the scan rate derived from B.

4.2.3 Sodium surface characterization

To verify our hypothesis that polymeric IL film helps stabilize sodium metal and prevent side reaction between electrode and aprotic electrolyte, an in-situ optical microscopy technique was applied to directly visualize how sodium deposits in a quartz cuvette optical Na/Na symmetric cell (Figure 41A). A constant current of 1 mA/cm^2 was applied to polarize one electrode and we choose this current to make the study consistent with our previous test in coin cells. Figure 42A shows

light microscopic images of the sodium electrode at different deposition times in a 1M EC/PC-$NaClO_4$ electrolyte. Due to the softness of sodium metal, the pristine sodium electrode surface was not perfectly smooth. As the deposition process continued, the electrode was gradually covered by two types of deposits- thin fiber-like and bulky mushroom-like, which were formed in a dynamically swinging movement manner. Both types of deposits grow not in a specific direction but spark randomly, which probably dues to the unevenness and defects of the electrode surface. The shinning fiber-like deposit was discovered previously on sodium metal surface at a very low current density of 57 $\mu A/cm^2$ [129] and on lithium electrodeposition as well[133]. Importantly, the bulky black sodium deposit was first discovered to the best of our knowledge, we tentatively attribute its formation to the uncontrolled side reaction with electrolyte. This type of deposit grows faster and seems to be more detrimental to the electrode as it quickly withdraws from the electrodes and floats randomly in the electrolyte, eventually becomes 'dead sodium' which lowers the coulombic efficiency.[110, 115] When DAIM was added in the electrolyte, a big improvement was observed during sodium deposition at the same current density (Figure 42B). It is obvious that the big black mushroom-like deposit was eliminated during the whole process of deposition, which probably indicates that the in-situ formed polymeric ionic film can protect sodium and eliminate the side reaction with liquid electrolyte. Though the needle-like deposits still exist, it is seen that the quantity of this type of dendrite is much smaller than that of the control and the growth rate is less than half than that of the bulky dendrites (Figure 41B). The grows of the needle deposits may related to the effective pore size (~1 μm) of the polymer film, which was approximated from the storage modulus ($4.05*10^{-3}$ Pa) of the polymeric DAIM. As the effective pore is in the similar length scale to that of the needles and much smaller than mushroom deposits, it can successfully

block the growing pathway of the mushroom deposits while some of the needles may penetrate through the film and continue to grow.

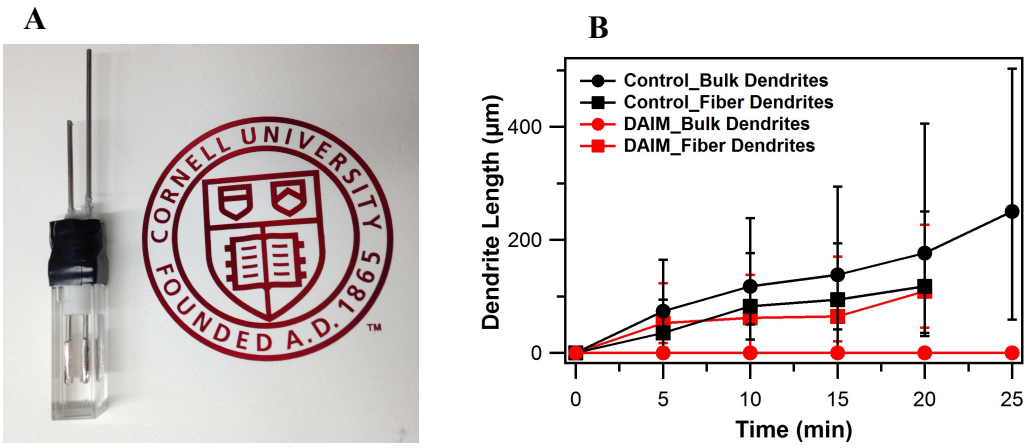

Figure 41: A. Photography image of the designed optical cell. B. Dendrite growth as a function of time in the optical cells with and without DAIM additive in the electrolyte.

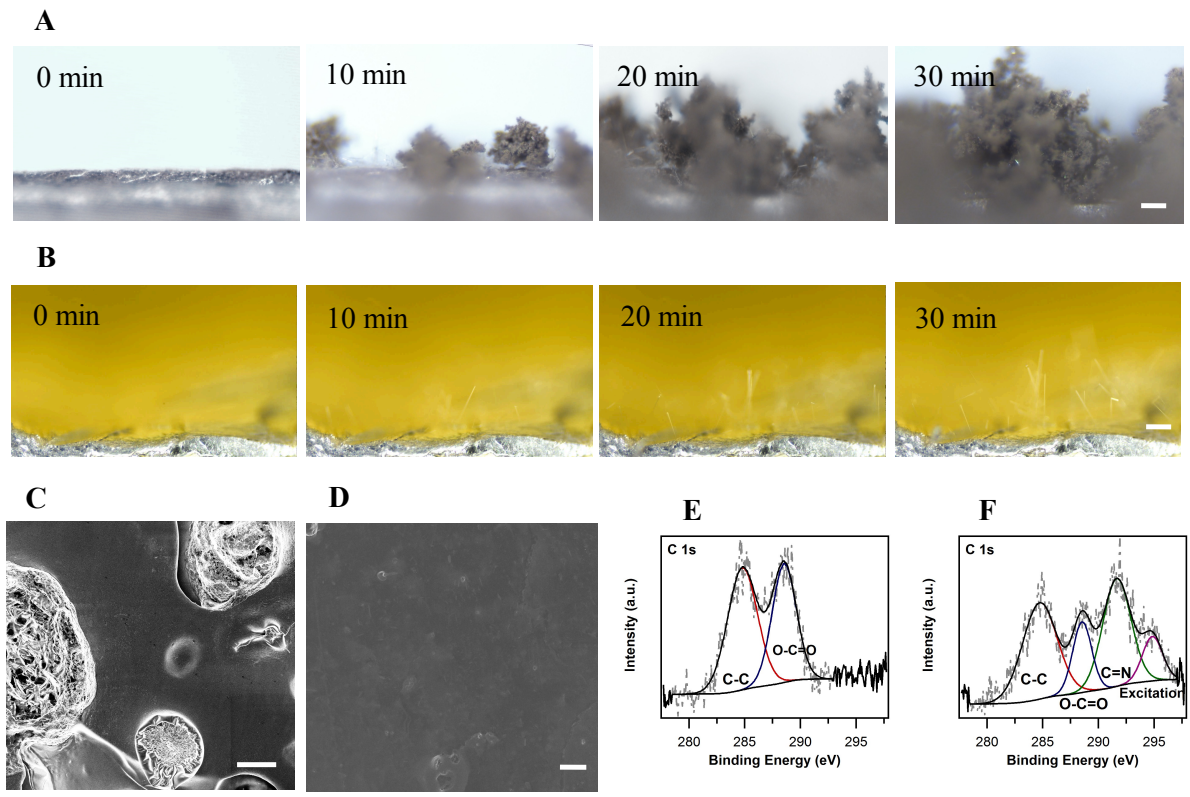

Figure 42: Visualization of the electrochemical sodium deposition. A. Light microscopy images of electrochemical sodium deposition on the sodium electrode in 1 M NaClO4 in EC/PC. The images were taken at sodium deposition at 0 min, 10 min, 20 min and 30 min at a current density of 1 mA/cm^2. B. Light microscopy images of the sodium deposition in the same conditions with A in1 M NaClO4 in EC/PC with 20 wt% DAIM as an additive (Scale bar: 50 µm). C and D. SEM images of the sodium metal surface after 10-hour electrodeposition in a symmetric coin cell without and with DAIM additive in the electrolyte (Scale bar: 20 µm). E and F, C 1s XPS analysis of the sodium metal surface in the same comdition with C and D respectively.

As the condition and environment are quite different between coin cells and optical cell due to assembling pressure and the existence of separators in the coin cells. We hypothesize with the help of mechanical pressure and separator, sodium can be engineered into an effective anode once the side reaction is eliminated and sodium surface is protected based on a recent theory study on lithium dendrite growth[114]. To verify our hypothesis, the morphology of the sodium metal anode after galvonastatic polarization and after 10 cycles of stripping and platting in coin cells were

examined by SEM (Figure 42C and D, and Figure 43). As we expected, sodium anode polarized in the existence of DAIM in electrolyte exhibits uniform and flat surface morphology with a film formed on top, indicative of dendrite free electrode deposition with the help of pressure and separator, however, the control sodium electrode was quickly oxidized when transferring it to the SEM sample holder. Though the MPIM and AVIM additives in the electrolyte seem to be beneficial compared with electrolyte no additive, they are not as effective as the DAIM additive which probably dues to the non-contact protection of the sodium metal and the reactivity of the vinyl group. C 1s based on X-ray photoelectron spectroscopy (XPS) analysis on the control sodium metal and sodium electrode deposited in the prescience of DAIM in the electrolyte verifies the existence of IL components on the sodium surface after one-minute sputtering on the sodium metal surface (Figure 42E and D).[134]

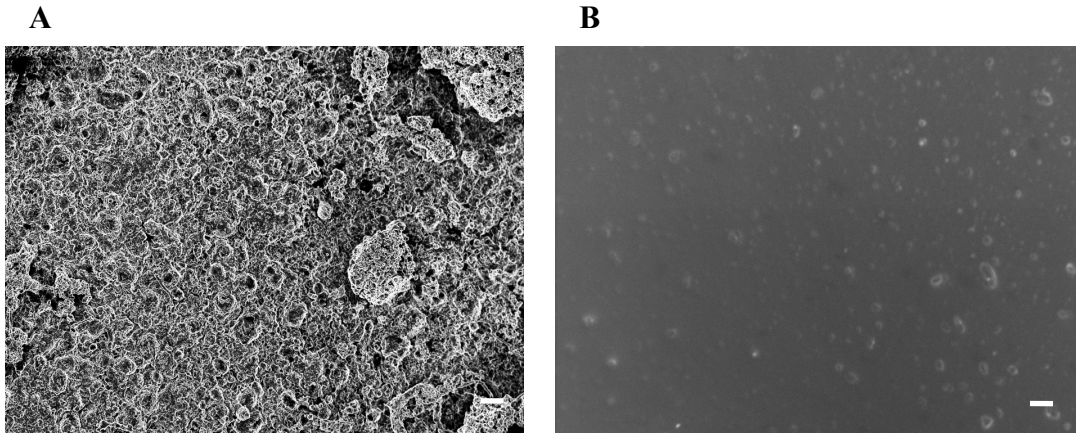

Figure 43: A and B. SEM images of the sodium metal surface after 10 cycles of stripping and platting in a symmetric coin cell without and with DAIM additive in the electrolyte (scale bar: 20 μm). In each cycle, the cell was charged and discharge at 1 mA/cm^2 for one hour in each step.

4.2.4 Electrochemical properties

To evaluate the suitability of the protected sodium anode for room-temperature sodium metal batteries, the sodium anode after 10 hour's deposition in the presence of 20 wt% DAIM in the electrolyte in Na/Na symmetric cell was investigated under galvanostatic conditions with $Na_3V_2(PO_4)_3$ and polyacrylonitrile-sulfur (SPAN) composite, respectively, as electrodes. $Na_3V_2(PO_4)_3$ is attractive because it exhibits high intercalation potential of around 3.4 V (vs Na^+ /Na), which makes $Na_3V_2(PO_4)_3$ a good candidate for next generation cathode materials for electrical energy storage, however, due to the larger ionic radius of sodium, it is a challenge to allow stable Na ion extraction and insertion.[135-139] Previous works usually applied fluoroethylene carbonate (FEC) as electrolyte additive to stabilize the passivation layer between electrode and electrolyte interphases[136, 137], however FEC is known to decompose and forms hazardous HF gas during electrochemical process[140, 141]. Therefore, it is urgent to develop alternative methods to stabilized this type of cell. SPAN composite cathode was capable of delivering high capacity and cycle stability in lithium metal batteries,[50, 142] and it is compatible with carbonate electrolyte. For these reasons, $Na_3V_2(PO_4)_3$ and SPAN serve as ideal candidates for investigating the electrochemical stability of the protected sodium anode in rechargeable batteries.

Figure 44A, B and C report the electrochemical characteristics of Na-$Na_3V_2(PO_4)_3$ cells based on the DAIM treated Na metal anodes. A floating-point test (Figure 44A) from 3 V to 5 V gives a time dependent current response for the cell with protected sodium electrode up to 4.8 V, while an irregular and noisy current response was observed for the control cell at almost entire voltage ranges. The improved cell stability over different voltage ranges directly relates to the reduced side reaction between sodium anode and aprotic electrolyte. This enhanced cell stability also

reduces the overpotential during galvanostatic cycling test (Figure 44B), which results in higher cycling stability and coulombic efficiency (Figure 44C). When the anode is protected by polymeric ion film, both the capacity and efficiency rise, with the coulombic efficiency exceeding 96 % and capacity maintaining at 97 mAh/g after 160 cycles, while the control cell exhibit a variation of coulombic efficiency and a quick decrease of discharge capacity to below 20 mAh/g in 30 cycles. We believe this direct benefit of dramatic improvements stems from the tethered and uniform polymeric film that continuous supply ions near the electrode and prevent sodium metal from reacting with liquid electrolyte.

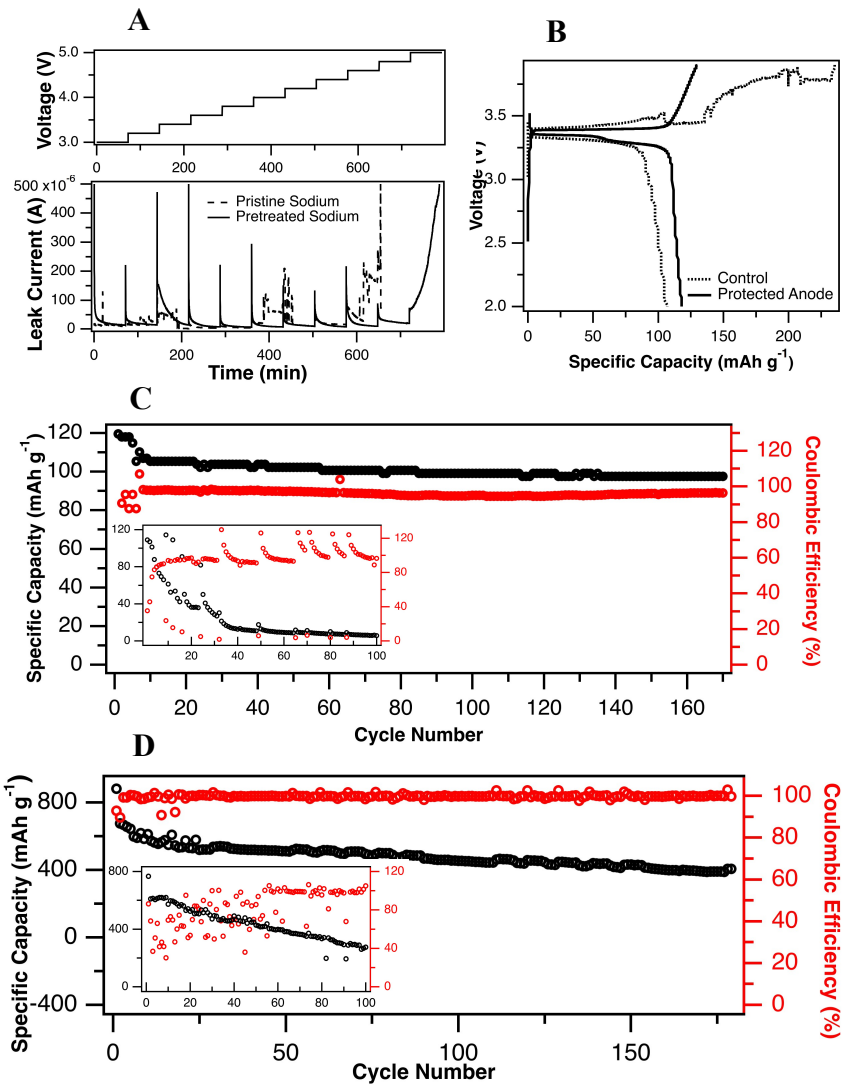

Figure 44: Full cell application for a high voltage $Na_3V_2(PO_4)_3$ sodium ion battery and high energy SPAN sodium metal battery. A. Constant voltage-charge profile of the Na-$Na_3V_2(PO_4)_3$ cells with pristine sodium anode and protected sodium anode in a carbonate electrolyte maintained at 3, 3.2, 3.4…5V for 2 hours at room temperature. B. The voltage profile and C. Cycling performance of the Na-$Na_3V_2(PO_4)_3$ cells with and without protected sodium metal anode (inset) at 100 mA/g of the active material in the cathode. D. Cycling performance of the Na-SPAN cells with and without protected sodium metal anode (inset) at 0.2 C (1C = 1675 mAh/g) based on sulfur in the cathode.

We also evaluate the application of the ion-rich sodium anode in Na-SPAN batteries. As SPAN has a high theoretical capacity, more coulombs will be applied to the cell during cycling. Therefore,

it is effective to evaluate the effect of the sodium anode protection in the system. As we expected, the protected cell gives rise to an almost 100 % coulombic efficiency and a reversible discharge capacity for over 100 cycles, however, the control cell bears random coulombic efficiency and the capacity drops to 200 mAh/g after 100 cycles (Figure 44D and Figure 45). The failure in the Na-SPAN cell, more likely be the same with the Na- $Na_3V_2(PO_4)_3$ cell, could be attributed to the side reaction with the electrolyte during cell charging, as the voltage profile is noisy and the efficiency is very low. Those results clearly indicate that the importance of protecting sodium anode in sodium metal batteries and their widely applications.

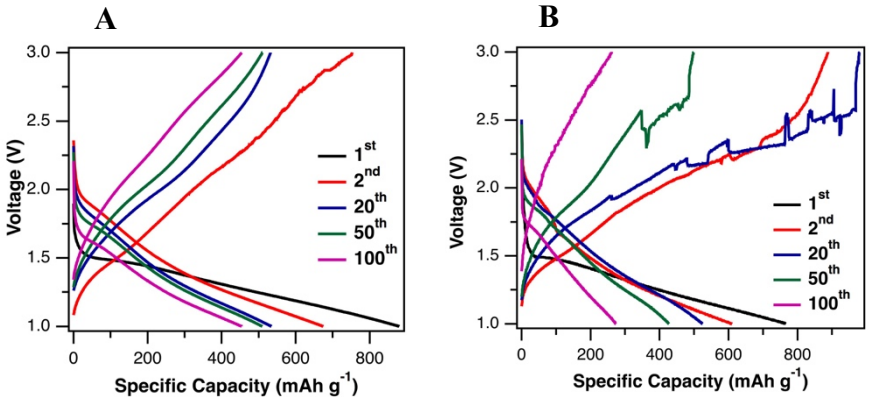

Figure 45: Voltage profile of the Na-SPAN batteries at various cycles with and without a protected sodium metal anode.

4.3 CONCLUSION

We report an example of fabricating polymeric IL protected sodium metal anode that can be cycled stably with high Coulombic efficiency at high current densities. The protected anode is developed by electroinitiated-polymerizing unsaturated functional IL monomer in electrolyte in-situ. We use both spectroscopic and analytical tools to show that polymeric IL film provide sufficient number

of immobile ions on the electrode surface to prevent sodium anode from reacting with aprotic electrolyte and reduce uneven sodium electrodeposition. Electron and optical microscopy as well as electrochemical analysis indicate that IL monomer form a protective film on the Na anode and stabilize deposition of sodium by at least two mechanisms. First, they form a polymeric SEI layer that protects sodium metal from parasitic side reactions with the liquid carbonate electrolyte. Second, they appear to utilize a previously reported tethered anion effect to stabilize deposition of Na. Our finding underscores the benefits of protecting sodium metal anode in the application of inexpensive rechargeable sodium metal batteries bearing high voltage or high specific capacity. Further investigations are needed to fully understand the effect of different tethered polymeric ions as well as the specific role that DAIM polymer film plays on metal anode protection. Moreover, the control process of the electroinitiated polymerization for protecting alkali metals is also worth studying.

4.4 MATERIALS AND METHODS

Materials Synthesis: Functional IL monomers AMIM, DAIM and AVIM bearing perchlorate anion were synthesized according to the previous methods with modifications [112]. In this work, $NaClO_4$ was used as the anion exchange source. The $Na_3V_2(PO_4)_3$ [135] and SPAN [142] cathode was synthesized based on the previous studies. The synthesized $Na_3V_2(PO_4)_3$ contains no graphene additive.

Material Characterization: The morphology of the sodium metals was studied by A LEO 1550 high resolution scanning electron microscopy (SEM), Olympus light microscope and Asylum MFP-3D atomic force microscopy(AFM). Waters Ambient-Temperature GPC was applied to analyze the molecular weight of the polymers. X-ray photoelectron spectroscopy (XPS)

measurements were performed with a Surface Science SSX-100 spectrometer using a monochromatic Al Kα source (1486.6 eV). Non-linear least squares curve fitting was applied to the high-resolution spectra, using CasaXPS software.

Electrochemical Characterization: Protected sodium metal anode was created by charging Na/Na symmetric cell at constant current of 1mA/cm^2 for 10 hours in a carbonate electrolyte containing 20 wt% IL monomers. 2032 coin-type cells were assembled using sodium metal (Sigma Aldrich) as the anode electrode, a microporous material, Celgard 3401, membranes as separator, a cathode with 80% active material, 10% Super-P Li carbon black from TIMCAL, and 10% poly (vinylidene difluoride) (PVDF, Sigma Aldrich) as binder in an excess of N-methyl-2-pyrrolidone in NMP, and electrolyte of 50uL 1M sodium perchlorate (NaClO4) in ethylene carbonate/propylene carbonate (EC/PC vol:vol=1:1) for each cell. Cell assembly was carried out in an argon-filled glove-box (MBraun Labmaster). The room-temperature cycling characteristics of the cells were evaluated under galvanostatic conditions using Neware CT-3008 battery testers and electrochemical processes in the cells were studied by cyclic voltammetry using a CHI600D potentiostat. Electrochemical impedance and floating tests were conducted by using a Solartron Cell Test System model 1470E potentiostat/galvanostat. For post-mortem studies, cells were disassembled in an argon-filled glove-box and the electrodes were harvested and rinsed thoroughly with the electrolyte solvent before analysis.

5 STABLE ELECTROCHEMICAL GROWTH ENABLED BY VISCOELASTIC FLOW

5.1INTRODUCTION

Electrodeposition is a popular electrochemical method used in various manufacturing processes for creating metals/alloys[143, 144], particulate[145, 146], and polymer material coatings[147]. The process also plays an important role in shorting of microcircuits and in electrochemical energy storage technologies based on batteries, where it must be carefully managed to facilitate stable and safe operations over a range of operating temperatures, current rates and over many cycles of charge and discharge[104, 115, 142, 148]. In simple liquid electrolytes, deposition is subject to hydrodynamic and morphological instabilities that drive strong convective processes near ion-selective interfaces, which have been studied intensively since the first reports of metal electroplating processes in the 1800s[114, 115, 118, 149-161]. These instabilities are in some cases beneficial because they promote mixing in slow, inertia-less flows, which reduces resistance to ion transport. This in turn enhances the efficiency of processes such as electrodyalysis that rely on fast ion transport to ion-exchange membranes[150, 152, 153, 156, 159-161] or battery electrodes[162], which requires large ionic currents to support high power operations. In many other situations, including electroplating and emergent secondary batteries that utilize reactive metals (e.g. lithium, sodium, and aluminum) as anodes the instabilities are problematic because they produce complex flows that cause formation of rough, ramified metal electrodeposits known as dendrites at planar interfaces[118, 151, 154, 155, 157]. As a result, context-appropriate strategies for selectively promoting/suppressing instability in any of these contexts has been of longstanding interest.

Unstable electrodeposition of metals that form chemically stable fluid-solid interfaces with liquid electrolytes (e.g. silver, copper, and zinc) originates from electro-hydrodynamic origins. In other metals such as lithium, sodium, and aluminum where the electrolyte react with the metal electrode to form a fragile interphase material, a combination of morphological and electro-hydrodynamic instabilities are responsible for unstable electrodeposition[118]. At low currents, dendrites arise naturally from non-uniform ionic conductivity of the heterogeneous interfaces electrolytes form in contact with many metals. Concentration of electric field lines on initial deposits/nucleates formed in high-conductivity regions of the interface promotes growth. Above a certain voltage, $V_c \approx 8RT/F$, the ionic current achieves a limiting value, $i_L = 4FcD_+/l$, which does not depend on applied voltage. At V_c, the ion migration rate exceeds that of diffusion and electroneutrality of the bulk electrolyte cannot be maintained at planar interfaces with an electrode or membrane that is impermeable to anions[118, 156, 159-161]. Here the expression for i_L assumes an electrolyte that is a dilute solution of a binary, monovalent salt; D_+ is the cation diffusivity; c the electrolyte concentration; l the inter-electrode spacing; and F Faraday's constant. A *space charge*, region is therefore formed at such interfaces that may extend many hundreds to thousands of ionic diameters into the electrolyte bulk (i.e. well beyond the quasi-equilibrium space-charge region that forms spontaneously at any charged substrate immersed in an electrolyte). At ionic currents above i_L, classical Nernst-Planck (*N-P*) theory predicts that the electric field near the electrodes diverge. In all self-consistent formulations of the governing electrokinetic field equations, a divergent electric field exerts a large electrical body force on fluid in the non-equilibrium space charge region, which drives a type of electro-osmotic flow termed electro-osmosis of the second kind to distinguish it

from normal electro-osmotic flow generated when an electric field tangent to a charged surface acts on the quasi-equilibrium space charge to produce convection.

A substantial body of work has confirmed these observations and shown that the instability plays a large role in both enhancing transport rates at ion-selective interfaces and in producing rough, dendritic deposition of metals in electroplating processes[114, 115, 118, 149-161, 163]. These studies indicate that the instability drives convective rolls that sweep ions away from regions surrounding a growing deposit and concentrate them on regions with the fastest growth rate[151, 164]. This enhances the rate of deposition of cations, but does so by promoting deposition at localized regions, leading to rough electrodeposits and tree-like dendritic structures in certain circumstances. In liquid electrolytes bounded by ion selective membranes, electroconvection has also been shown by means of theory[152, 153], experiment[160, 161], and numerical simulations[156] to produce ionic current densities above the limiting value predicted by *N-P* theory. It is noted that in all of these studies, the fluid is a simple Newtonian liquid in which the resistance to large-scale convective flow and small-scale ionic motions is the same.

5.2 RESULTS AND DISCUSSION

The linear stability analysis of electroconvection first discussed by Rubinstein and Zaltzman [152, 153]reveals that in an unsupported, symmetric, binary electrolyte, electro-osmosis of the second kind is unstable. This analysis can be extended to show that at currents near i_L, small perturbations to the fluid velocity grow at a dimensionless rate,

$$\sigma = (k/l)^2 V_0 [V_0 Pe/8 - \sqrt{Pe(1-t_+)}] \qquad (1)$$

for *k/l* >> 1. Here $2\pi / k$ is the wavelength of the perturbation; $\mathrm{Pe} \equiv Ul / D_+ = \varepsilon (RT / F)^2 / \eta D_+$ is a Peclet number based on a characteristic fluid velocity $U = \varepsilon (RT / F)^2 / \eta l$ that captures the relative importance of convention and diffusion; V_0 is the dimensionless voltage; and t_+ is the fraction of the ionic transport due to the cations. This expression shows that while the growth rate of the instability is largest on the smallest length scales (largest *k*), it is non-negligible on all length scales; meaning that the convective flow produced by the instability may extend to macroscopic length scales in an electrochemical cell. The expression also shows that marginal stability is achieved at a critical Peclet number $Pe_c = 64(1 - t_+) / V_0^2$, on all length scales. This condition leads to a viscosity requirement for stability in a Newtonian liquid electrolyte,

$$V_0 \leq 8 \frac{F}{RT} \sqrt{D_+ \eta (1 - t_+) / \varepsilon} \qquad (2)$$

This means that in an electrolyte where the mechanisms for ion transport (conductivity) and momentum transport (electroconvection) can be separated, the width of the limiting current regime, $\Delta V = \frac{RT}{F} V_0 - V_c$, can be extended indefinitely.

The main results of this report are summarized in Fig. 46, where it is shown that the limiting current regime can be markedly extended by introducing moderate amounts of an ultrahigh molecular weight soluble polymer to a liquid electrolyte solvent. By means of tracer particle velocimetry using neutral, micron-sized particles, we find that the source of enhanced limiting current regime is the suppression of electroconvective flows in viscoelastic liquid electrolytes. Extending these findings to electrodeposition of metals, we report that even small amounts of ultrahigh molecular weight polymers dissolved in conventional liquid electrolytes are effective in suppressing non-

uniform deposition, with the most dramatic effects apparent in softer metals, such as lithium and sodium, of contemporary interest for high-energy rechargeable batteries. The improved stability is discussed in terms of the polymer's ability to suppress unstable secondary flows, without compromising ionic mobility. The viscosity thresholds at which the polymer begins to have beneficial effects are nevertheless calculated to be orders of magnitude lower than expected based on any current analysis of electroconvective instability in Newtonian liquids, implying that other features of the electrolytes such as elasticity, particularly near the liquid-solid interface may play an important role. In this regard, our observations bear qualitative similarities to the better-known *Toms Effect*, in which small, even ppm, quantities of ultra-high molecular weight flexible polymer additives in Newtonian fluids undergoing unstable, turbulent flow produce large reductions in the frictional drag on surfaces wetted by the fluid[165, 166].

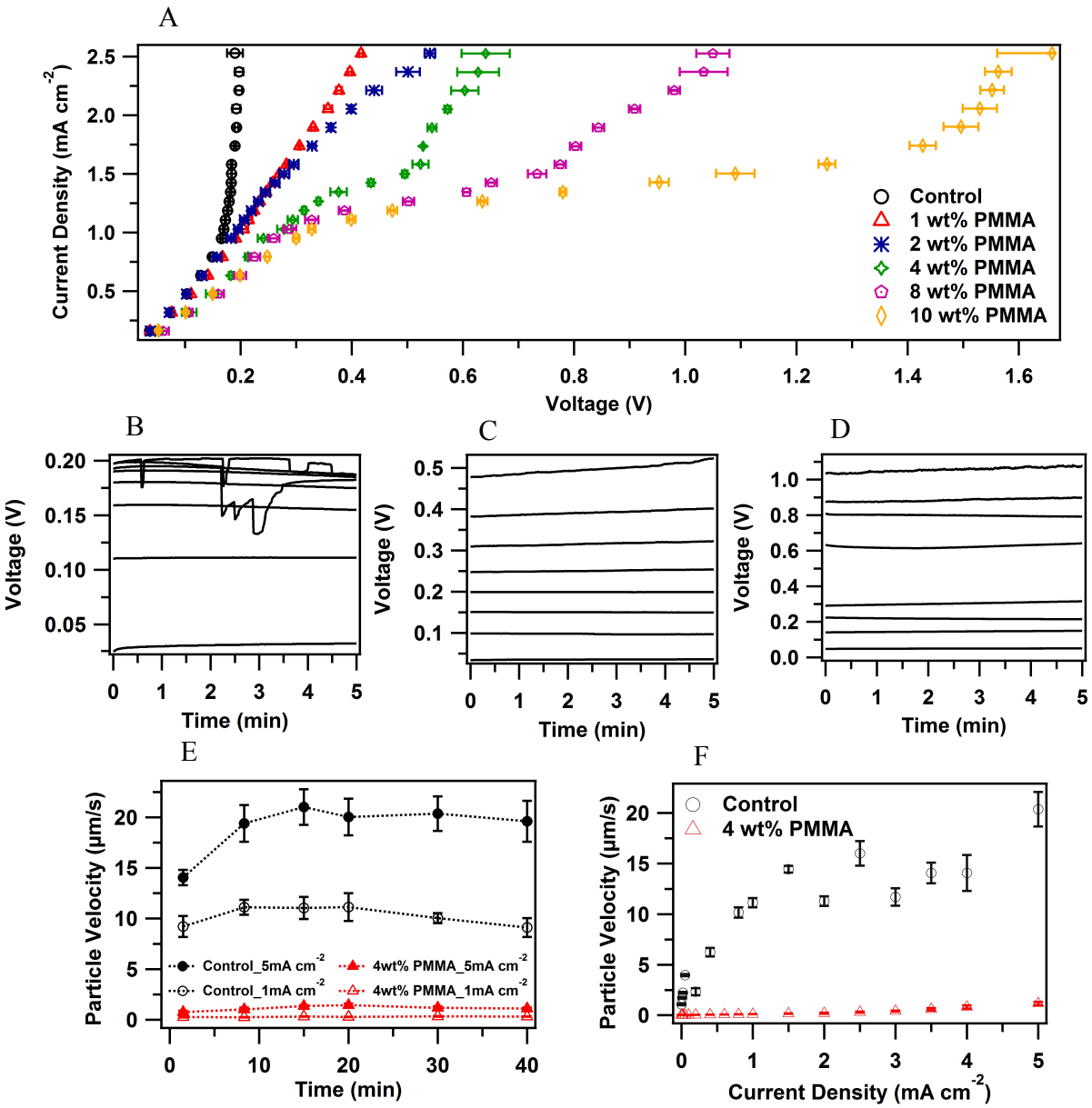

Figure 46: Electrochemical characteristics of the viscoelastic electrolytes. (A) Current-Voltage curves of the electrolytes with different PMMA concentrations. (B, C and D) Voltage versus time profiles of the cells with (C) no PMMA, (D) 2wt% PMMA and (E) 8wt% PMMA at different current densities (from 0.316 to 2.526 mA/cm^2 with an increase of 0.316 mA/cm^2 in each step). (E) Flow velocities of the electrolytes during the one hour lithium electrodeposition in an optical cell. (F) Flow velocities of the electrolytes during the lithium electrodeposition as a function of current densities.

To create electrolytes in which ion and momentum transport pathways are uncoupled, we use semidilute solutions of high molecular weight (M_w ~ 1.5 x 10^6 g/mol, M_w/M_n = 1.1), atactic poly(methyl methacrylate*)* (*PMMA*) (Agilent Technologies), dissolved in various solvents. High molecular weight PMMA is chosen for at least three reasons. First, it is soluble in a wide variety of non-aqueous, high-dielectric constant liquid electrolytes, including carbonates (ethylene carbonate (EC), ε = 89.8, propylene carbonate (PC), ε = 64.9) and dimethyl sulfoxide (DMSO), ε = 46.7. Second, the polymer has low electrochemical activity, low dielectric constant (ε = 2.6-3.6) and low affinity for the solvated metal cations we intend study, and Gel polymer electrolytes based on PMMA have been employed in secondary batteries[167, 168] and super capacitors[169] for several decades with little attention given to how the underlying physical properties of the electrolytes influence their function. Finally, for high molecular weight polymer, the critical concentration $c^* \sim M_w^{-4/5}$[170] at which swollen, polymer chains overlap and impart polymer-like physical properties to the electrolyte is low. This means that electrolytes with high levels of entanglements and high viscosity can be achieved in liquids with high, solvent-like ionic conductivity.

Results summarized in Fig. 46A report current-voltage (*i*-V) response of PMMA-EC/PC-1M bis(trifluoromethane) sulfonimide lithium (LiTFSI) electrolytes measured in the simple O-ring style symmetric Li/Li electrochemical cell depicted in Fig. 47 Current ramp measurements, wherein a current was imposed on the electrolyte for a fixed period of time and the voltage response recorded were used. By varying the measurement time at each current and ramping the measurement current through a range of values, it is possible to record the *i*-V curve in electrolytes with different polymer concentrations at conditions that approach steady-state (see Figs. 46B-D).

As shown in Table 5, the limiting current for the control (no PMMA additive) is estimated to be 2.95 mA/cm^2, in the dilute solution limit. Experiments show that the actual limiting current measured in dilute aqueous $CuSO_4$ solutions may be 1.5-4 times lower than theoretical estimates from Nernst-Planck theory[160, 161]. At low current densities, the figure shows that an Ohmic region observed in all cells and the slope of the *i*-V curve is a weak function of polymer concentration. This result means that in the concentration range studied, the polymer indeed has a minimal effect on electrolyte conductivity. In the control cells, the Ohmic region is immediately followed by a second regime in which current increases much faster than linear with V and, except for a slight change of slope at ca. $i \approx 1.6$mA/cm^2, i.e. around ½ the N-P estimate for i_L, there is no sign of the diffusion-limited transport regime. This stands in sharp contrast to the *i*-V curve obtained upon addition of just 1wt% of the polymer to the electrolyte, where it is seen that the Diffusion controlled Ohmic regime extends to voltages more than ten-times the thermal voltage (RT/F), behavior that is normally associated with overlimiting conduction. This association becomes stronger as the polymer concentration rises. At a PMMA concentration of 4wt% a clear plateau is observed over a range of voltages, indicative of diffusion limited ion transport. It is apparent nonetheless that even in these systems, significant conduction is seen above the limiting current density. At yet higher polymer concentration, the diffusion-limited transport regime extends further, becoming more than forty-times the thermal voltage at 10wt% polymer, and the high-voltage slope of the *i*-V curve is lower. If overlimiting conductance is the result of electroconvective instability, the results in Fig. 46A show that these instabilities are driven to progressively higher voltages as polymer concentration rises.

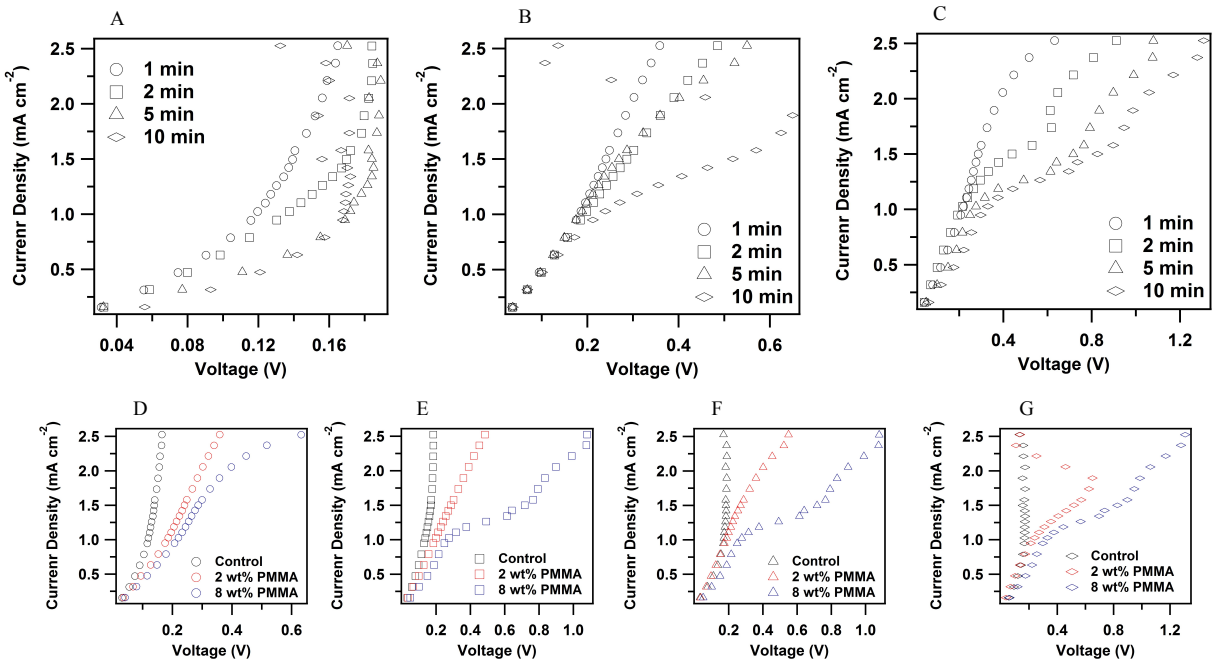

Figure 47: Electrochemical characteristics of the viscoelastic electrolytes at different time scales. (A, B and C) Current-voltage curves of the electrolytes with (A) no PMMA, (B) 2 wt% PMMA and (C) 8 wt% PMMA at different time scale for each current step. (D, E, F, G) Current-voltage curves of the electrolyte with different amount of PMMA kept for (D) 1min, (E) 2 min, (F) 5 min and (G) 10 min for each current step.

Table 5. Transference number of the lithium electrolytes and the approximated overlimiting current during lithium deposition in the optical cell (J_1) and O-ring coin cell (J_2).

	t^+	J_1* (mA/cm^2)	J_2* (mA/cm^2)
Control	0.428	1.50	2.95
1wt%	0.442	1.58	3.10
4wt%	0.396	1.32	2.59
8wt%	0.330	0.97	1.91

Time-dependent voltage profiles (Fig. 46B-46D) measured at current densities bracketing the current where the change of slope is observed show that, beginning at current densities of around 1.6 mA/cm^2, the voltage profiles for the control electrolyte do not reach a steady value and, at higher current densities, large random transient voltage excursions are observed. While these large transients are largely suppressed in electrolytes containing PMMA, there is a notable reappearance of a noise component at higher voltages where the overlimiting conductance reemerges. A similar result is reported in Fig 47 where we characterize the effect of the measurement time on the shape of the *i*-V curve. While it is plausible to attribute these behaviors to the increased noise associated in previous literature with overlimiting conductance and electroconvective instability, this designation is complicated in the present case by the fact that Linear sweep voltammograms obtained from slow voltage ramp measurements (Fig. 48), show that there is a current maximum near 0.2V, indicating that Faradaic processes associated with Li plating and stripping may play a role.

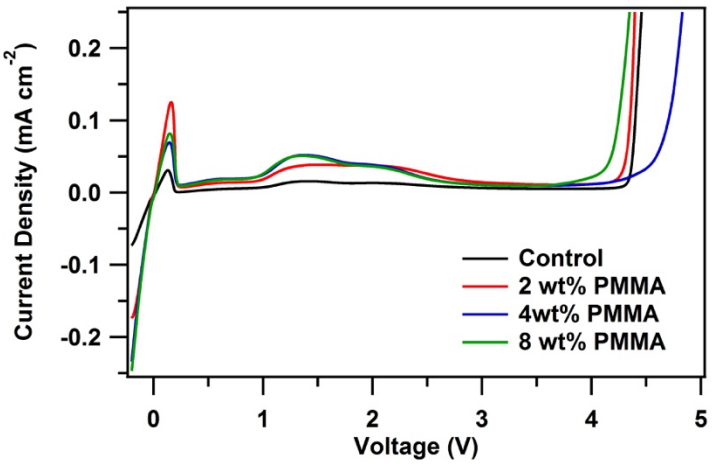

Figure 48: Linear scan voltammetry of the Li/stainless steel cell in the presence of different amount of PMMA in the electrolyte from -0.2 V to 5 V at a scan rate of 1 mV/s.

It is possible to gain more direct information about electroconvection in the electrolytes from tracer particle velocimetry experiments. These measurements were made by dispersing 10 μm uncharged polystyrene microparticles dyed blue in the electrolyte and tracking their time-dependent motions in an optical cell (Fig. 49) interfaced with an optical microscope outfitted with a video camera. *A* well-polished stainless steel electrode was used as the cathode for all experiments, while a range of anode materials (Li, Na, Zn, and Cu) were employed. As discussed later, this range of anode chemistries allowed us to establish the broad effectiveness of polymers in stabilizing electroconvection. A fixed electrode spacing of 1.5mm was maintained during all experiments. Videos were analyzed using the ImageJ-based FIJI package (National Institutes of Health) and particle motions tracked using the TrackMate plugin. Particles were identified by the Laplacian of Gaussian (LoG) detector, with an estimated blob diameter of 10μm. Trajectories of particles were generated using the simple linear assignment problem (LAP) tracker. Figs. 46E report time-dependent average velocities in stainless steel|Li cells measured at current densities slightly below and above the experimentally determined i_L value, and on timescales much larger than those probed in the *i*-V experiments discussed in the last section. It is seen that irrespective of the current density, tracer particles move far more slowly (by a factor of around 20) in the electrolyte containing PMMA than in the control. The results in Fig. 46F and Fig. 50 show that the polymer-induced slow-down of tracer motions is observed at all current densities flow and voltages, with the largest effect observed at voltages in the range 0.1-0.3V.

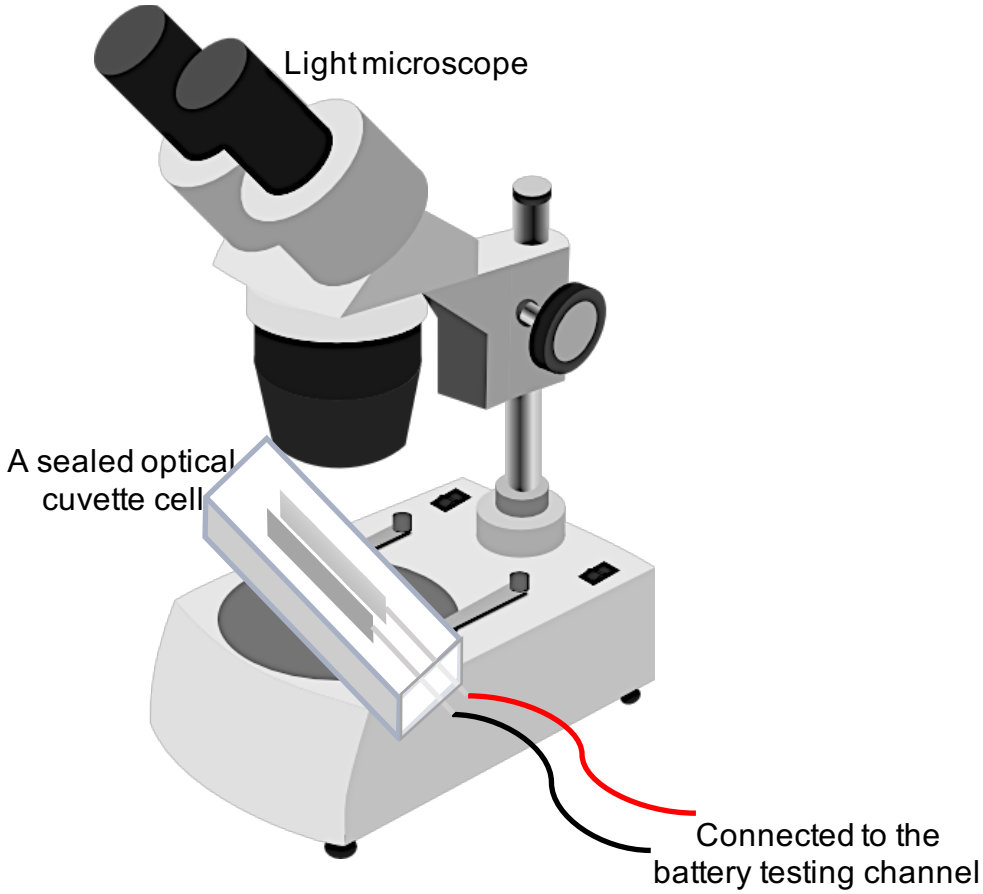

Figure 49: Schematic drawing of the experimental set up used to perform the visualization experiment for electrodeposition.

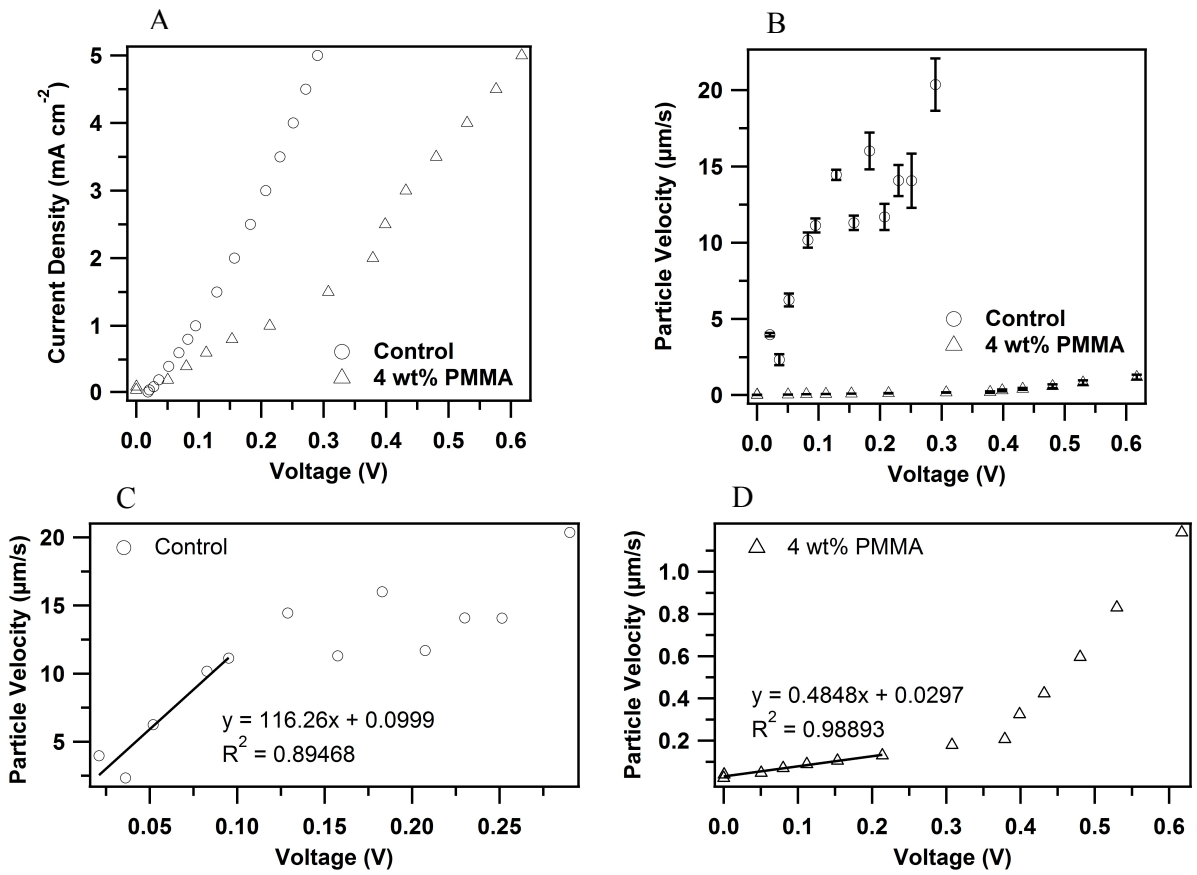

Figure 50: Flow velocities in the Newtonian liquid electrolyte (EC/PC-1M LiTFSI) and a representative viscoelastic electrolyte (4wt% PMMA in EC/PC-1 M LiTFSI) as a function of voltage. (A) Current-Voltage curves of the electrolytes with and without PMMA in the electrolyte. (B) Flow velocity as a function of voltage. (C), (D) Respective, linear analysis of the flow velocity at low current densities for the control (no PMMA) and viscoelastic liquid electrolytes.

Fig. 51A, B and Fig. 52 report the rheological properties of the electrolytes used in the study measured at 25°C. Oscillatory shear measurements on a Rheometrics Ares rheometer outfitted with cone-plate fixtures were used for these measurements. It is apparent from the figure that the electrolytes that produce the largest effects in both the particle tracking and electrokinetics measurements are viscoelastic liquids, displaying dominant elastic properties, $G' > G''$, over a range of timescales $t < 1/\omega_c$, where ω_c is the frequency at which $G' \approx G''$. Figure 51B reports the zero-shear rate, Newtonian (see Fig. 52) shear viscosity for the electrolytes over the full range of

PMMA concentrations studied. At the lowest polymer concentration, the electrolyte viscosity is already 20mPas, about twenty times that of the control electrolyte. And, at a concentration of 4wt%, it is already more than three orders of magnitude higher than the viscosity of the control electrolyte. It is also apparent from the results in Fig. 51B that beginning at a polymer concentration of around 3wt%, the polymer has a much larger effect on electrolyte viscosity. This transition is known to mark the onset of entanglement behavior in polymeric liquids and its association with the strong suppression of overlimiting conductance and tracer particle migration is consistent with our hypothesis that the onset of entanglements would decouple ion and momentum transport in the electrolytes, meaning that the variable $D_+\eta$ in *Eq*. (2) is not a constant. Under these conditions, this expression can be easily rearranged to show, $\Delta V : \sqrt{\eta}$ in for a Newtonian liquid electrolyte.

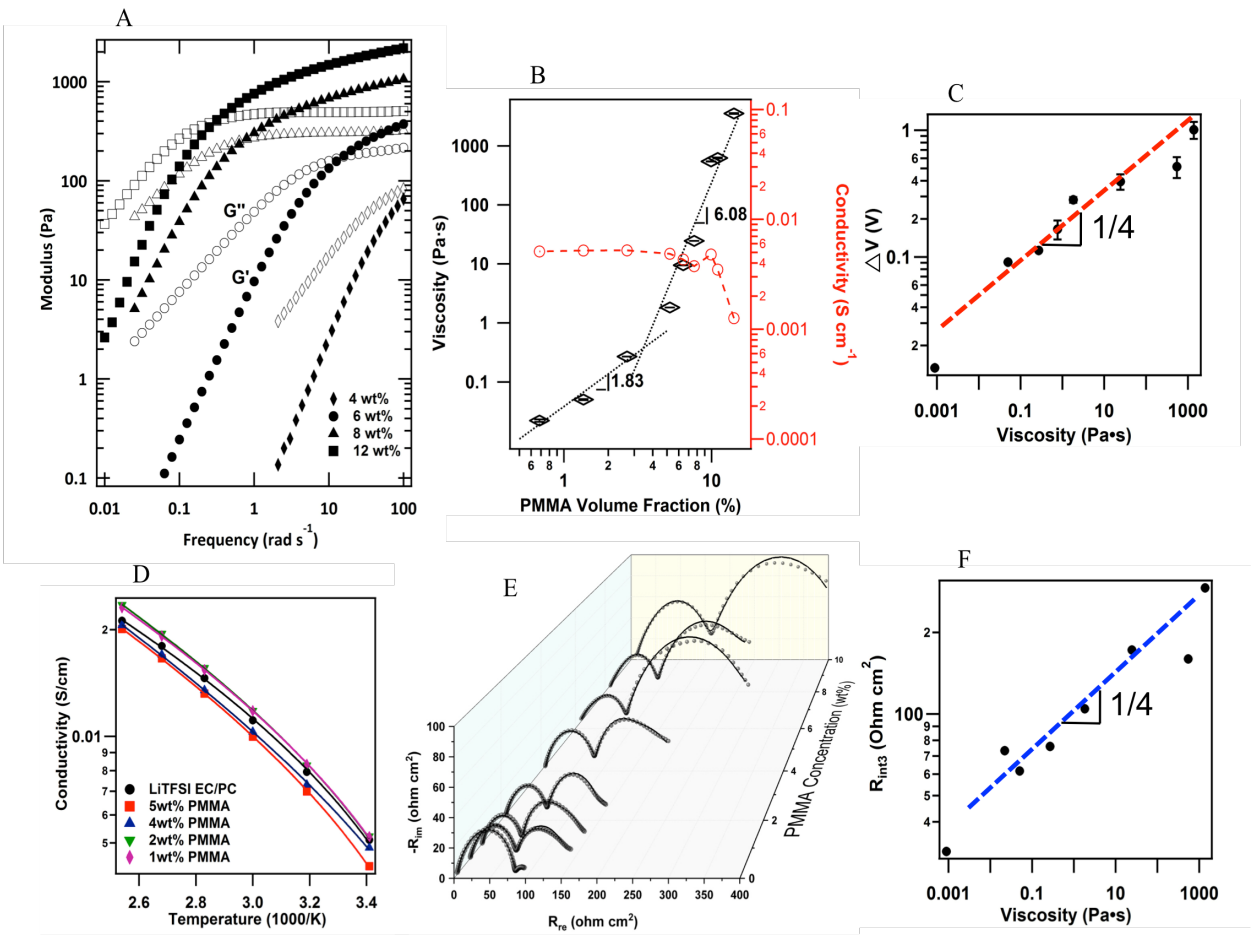

Figure 51: Physical characteristics of viscoelastic liquid electrolytes. (A) Frequency-dependent dynamic storage G' (filled symbols) and loss G'' moduli (open symbols) for PMMA-EC/PC (v/v 1:1)–1M LiTFSI electrolytes as a function of polymer concentration. (B) Concentration regimes of zero-shear viscosity and conductivity at 25 °C. (C) Extended stability regime (from Fig. 46A) in viscoelastic electrolytes as a function of electrolyte viscosity. The dashed line through the data shows that the experimental data can be approximated by the scaling relation, $\Delta V : \eta^{1/4}$. (D) DC ionic conductivity of the viscoelastic liquid electrolytes as a function of temperature. The solid lines are Vogel–Fulcher–Tammann (VFT) fits for the temperature-dependent ionic conductivity. (E) Nyquist plot obtained from EIS measurements in electrolytes with different polymer concentrations. The solid lines are fitted by an equivalent electrical circuit model shown in Fig. 53. (F) Polymer contribution to the area squared resistance of an electrolyte/Li interface as a function of electrolyte viscosity. The dashed line through the data shows that the experimental data obeys an approximate scaling relation, $R_{int3} : \eta^{1/4}$.

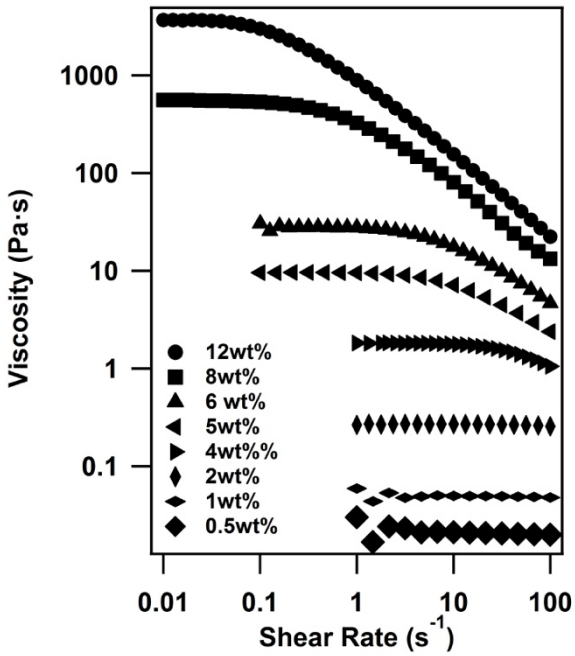

Figure 52: Steady shear viscosity for the PMMA electrolytes at 25°C.

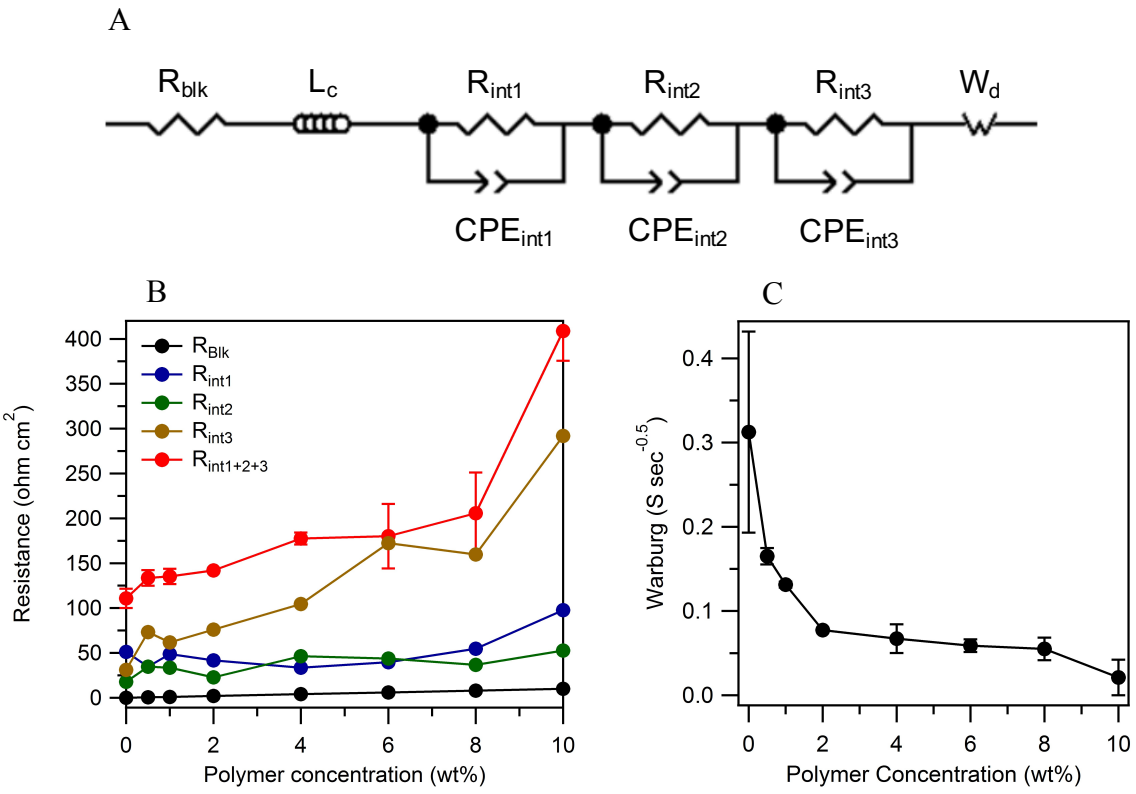

Figure 53: (**A**) Electrical model used to fit the Nyquist plot. (**B**) Bulk and interfacial resistance as a function of polymer concentration in the electrolytes obtained from the circuit fitting. (**C**) Warburg element as a function of polymer concentration.

The results in Fig. 51A show that at a PMMA concentration of around 4wt%, a significant elastic contribution is expected in electrolytes on timescales of order 10ms and at 8wt%, elastic effects are evident on timescales of seconds. Optical birefringence measurements performed using a polarization modulation approach reported elsewhere[171, 172] that allows both the orientation angle and birefringence of polymer chains to be quantified as a function of time show that the electrolytes are non-birefringent under the conditions of our polarization measurements. This means that PMMA molecules remain randomly oriented in the bulk electrolyte, indicating that the flow gradients in the bulk fluid are lower than the thresholds deduced from Fig. 51A. This behavior is quite different from what has been reported for drag reducing polymer solutions. Whereas the most effective turbulent drag reducing polymers have a very large effect on the extensional viscosity and almost no effect on the shear viscosity of the bulk fluid host, here we find that the most promising electrolytes for suppressing electroconvective instability have shear viscosites orders of magnitude higher than their Newtonian electrolyte host, but no noticeable signs of orientation in the bulk phase. As illustrated in Fig. 51C the polymer shear viscosity has a quite noticeable effect on ΔV . The dashed line fitted to the data shows that over the range of concentrations where a plateau in the *i*-*V* data can be defined with the greatest certainty, the experimental results can be approximated to a power-law scaling relation, $\Delta V : \eta^{1/4}$, i.e. substantially weaker than estimated from the marginal stability requirement for a simple, Newtonian liquid electrolyte. Additionally, by rearranging variables in *Eq* (2), the requirement for marginal stability for a Newtonian liquid electrolyte can be written in terms of the electrolyte

viscosity, $\eta \geq \varepsilon(V_0 RT/F)^2/(64D_+(1-t_+))$. Using typical values ($\varepsilon \approx 80; RT/F = 25.7mV; V_0 \approx 1; D_+ \approx 2\times10^{-9} m^2/s; t_+ \approx 0.5$), we estimate that for a Newtonian fluid electrolyte, a viscosity of at least 6.5×10^5 Pa.s would be required to stabilize electroconvection. This value is evidently three or more orders of magnitude higher than what is observed experimentally, meaning that other stabilizing processes are present in the electrolytes.

Fig. 51D reports temperature-dependent ionic conductivity of the electrolytes with various PMMA concentrations. These measurements were performed in symmetric stainless steel cells filled with the electrolytes and at temperatures in the range 20 to 70 °C. It is apparent that the DC ionic conductivity of the electrolytes changes little from the control (approx. 4×10^{-3} S cm^{-1} at 25^{o}C, see Fig. 51B)) over the range of polymer concentrations studied. Thus, the changes in conductivity produced by addition of the polymer are obviously negligible in comparison to the changes in electrolyte viscosity and elasticity imparted by the polymer. Ion transport properties at the electrolyte/electrode interface reveal different features. *I*mpedance spectroscopy was used to quantify the bulk and interfacial resistance in lithium symmetric cells. The resultant Nyquist plots are reported in Fig. 51E. It is apparent from the plots, that even at the lowest concentration, the polymer contributes a well-defined second interface at the electrode. The width of the second semicircle therefore appears to provide a rough measure of the resistance to interfacial ion transport imparted by the polymer. It is seen to remain essentially constant up to a bulk polymer concentration of around 2wt%, whereafter the contribution of the interfacial resistance from the second semicircle rises with polymer concentration. By fitting the equivalent circuit model illustrated in Fig. 53A[173, 174] to these plots, more quantitative information about the bulk and interfacial resistances can be obtained (see Figs. 53B & 53C). The area squared resistance (ASR),

R_3, for the second interface correlates with the bulk polymer viscosity and is reported in Fig. 51F, along with the interfacial resistance R_1 and R_2, which is insensitive to the polymer component. It is apparent from the figure that R_3 obeys a rough 1/4 power-law relationship with respect to η which is essentially identical to that found previously for ΔV. We conclude that the polymer's ability to stabilize electroconvection is principally through its effect on the interfacial resistance and the weaker than predicted dependence of ΔV on η reflects the weaker than expected effect of polymer viscosity on R_3. This conclusion is more important than it might at first appear because whereas the ΔV results are for electrolytes driven at high currents, where large levels of interfacial shear, orientation, and elastic effects are possible[171, 172], the EIS experiments are performed for systems near equilibrium. That both measurements reveal that the electrolyte viscosity exhibits the same, weak power law effect indicates that interfacial elasticity of the deformed electrolyte at the fluid/solid interface does not play a significant role in the stabilizing effect of viscoelastic electrolytes on electroconvective instability.

Our physical picture of the electrolyte/electrode interface is therefore of a stratified structure: a polymer-depleted layer in immediate contact with the electrode, overlayed by a polymer-rich bulk-like fluid layer. On reactive metal electrodes, such as lithium and sodium, the first layer is likely hosted in a nanoporous solid-electrolyte interphase (SEI) formed by chemical reaction of electrolyte components in contact with the electrode, the structure of which may be partly responsible for exclusion of the high molecular weight polymer. We believe that it is the viscosity mismatch at the interface between the two fluid layers that produces the dependence of R_2 on η, even though the bulk electrolyte conductivity is essentially independent of η. This perspective is supported by x-ray photoelectron spectroscopy (XPS) depth-profile analysis discussed in the

supporting materials section (Figs. 54A and 54B). In particular, we used XPS high resolution scan to analyze the composition profile of C 1s, O 1s, Li 1s and F 1s on the surface of electrodes harvested from cells used for the electrokinetic measurements. These measurements show that while the polymer component has an effect on the XPS spectra in the uppermost layer (associated with the bulk electrolyte), the electrolyte within a distance of 100 nm of the electrode shows essentially no chemical difference from the control (no PMMA) electrolyte by deconvoluting the C 1s and O 1s profiles[175, 176]. Moreover, lithium surface shows a major decomposition product of LiF in both electrolytes at a depth of 100nm as well. Previous studies have shown that unlike simple liquids, which obey the conventional no-slip condition at liquid/solid interfaces, entangled polymer solutions can slip relative to the surface by at least two processes. Stress-induced disentanglement of surface bound and free polymer chains may, for example, produce relative motion between the bulk polymer and an adsorbed layer at stresses above a critical value[177-179], around one tenth of the high-frequency elastic modulus reported in Fig. 51A. Depletion of polymer chains at a fluid/solid interface also produces a lower-viscosity, polymer-lean fluid phase in immediate contact with the solid, which interacts with the high viscosity bulk liquid. The viscosity difference between the two fluid layers can generate strong interfacial slip of magnitude comparable to the viscosity ratio[180] at essentially any stress. Interfacial slip by either mechanism would result in significantly smaller stresses at the interface than anticipated from the bulk electrolyte viscosity, which would weaken the boundary condition used in deriving *Eq.* 1 and would simultaneously weaken electroconvection and reduce the fluid's resistance. Slip by the first mechanism can be ruled out as the source of our observations on two grounds, first it would have no effect on transport in the equilibrium (unstressed) state probed in the EIS experiments and

second it would require strong polymer adsorption, which is not supported by the XPS data. Interfacial slip by the second mechanism is favored by the stratified fluid model that follows from the EIS and XPS experiments and could explain our observations. More work is clearly needed, however, to prove that this is the source of our observations and such studies are already underway using an experimental approach similar to that reported in reference[171, 172], with the aid of Direct numerical simulations of electroconvection[156] of viscoelastic liquids with no-slip and slip boundary conditions.

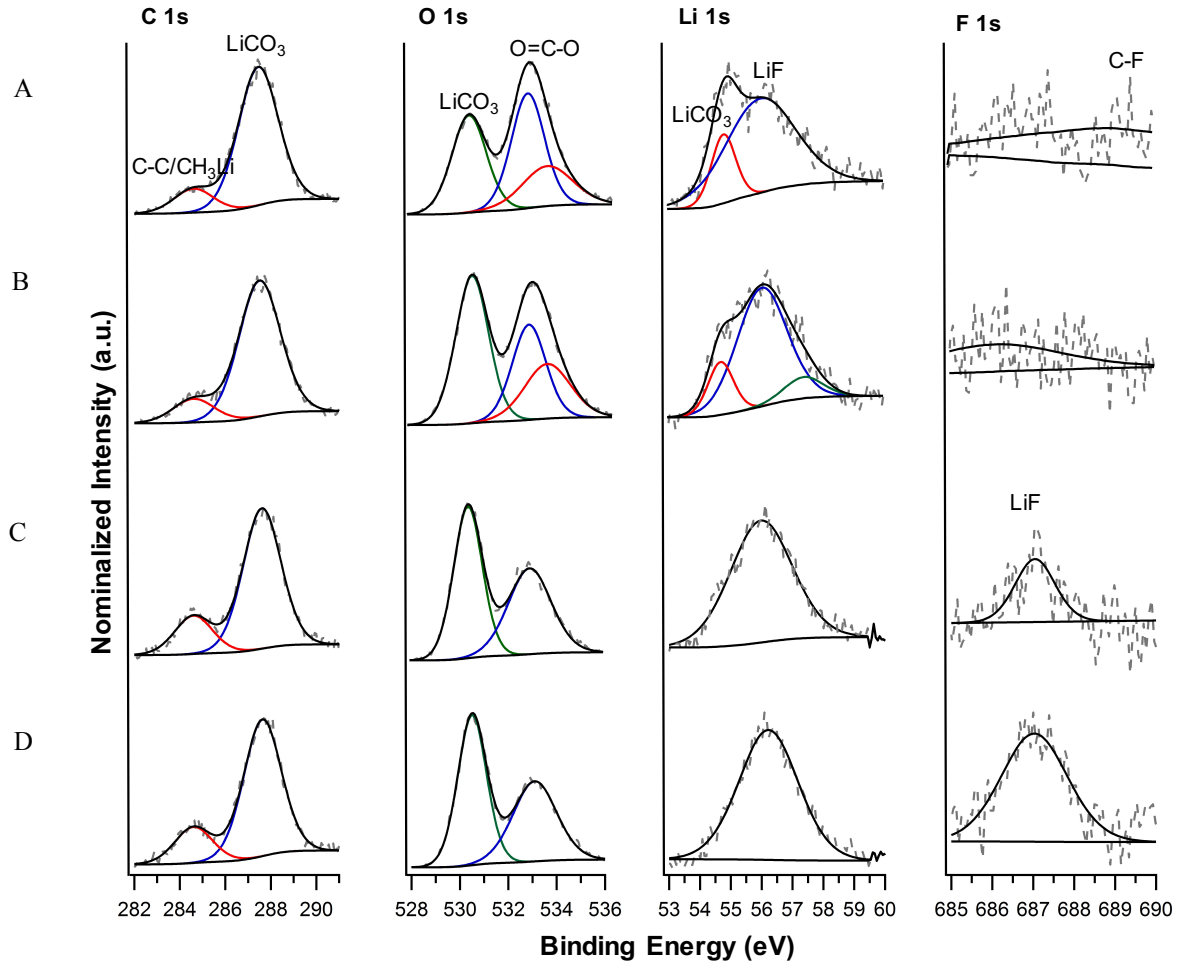

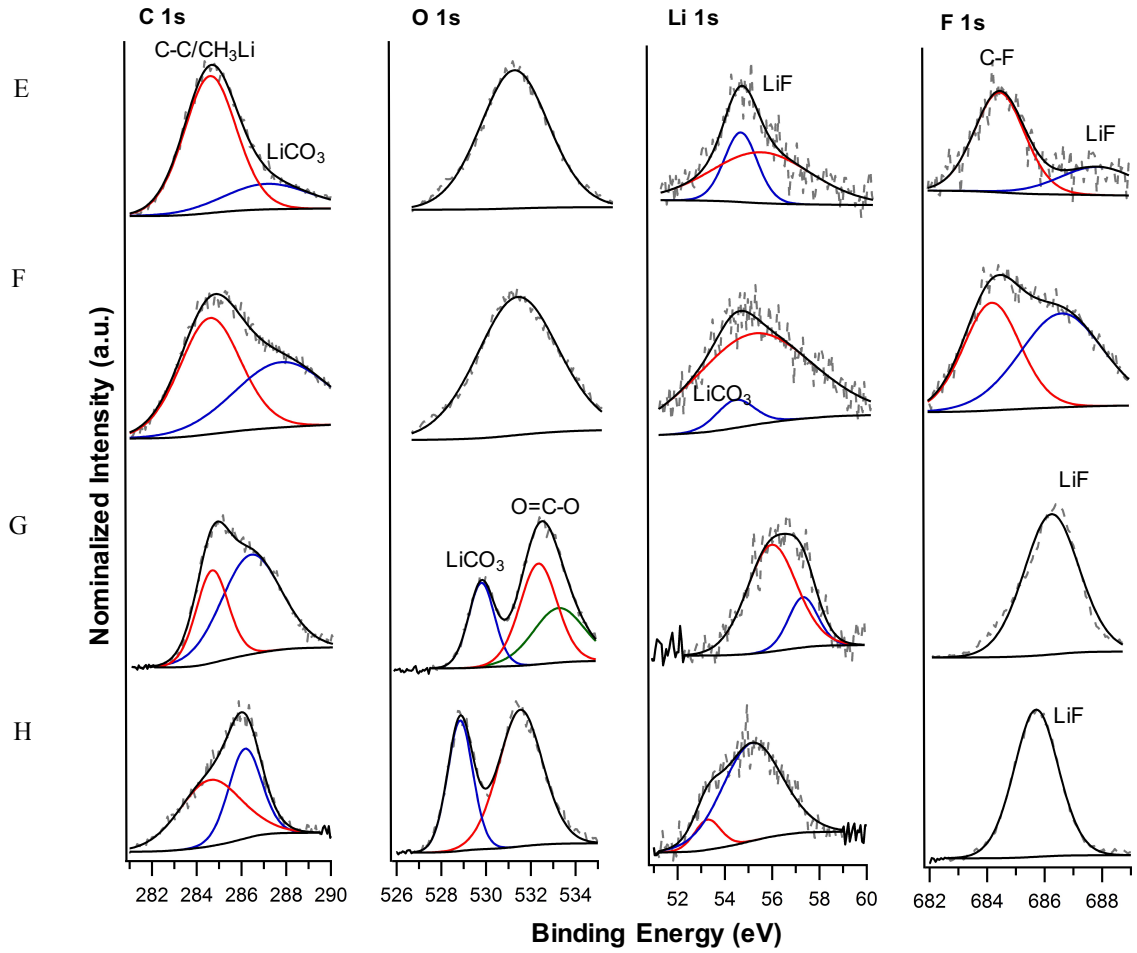

Figure 54: Depth-profiling XPS spectra of the lithium metal surface after the electrodeposition for one hour at a current density of 1 mA/cm^2. (A to D) High resolution scan of C 1s, O 1s, Li 1s and F 1s spectra after 0, 30, 1200, 6000s itching by argon with a pass energy of 2 kV and current of 2 μA in an area of 2x3 mm in the Newtonian liquid electrolyte (EC/PC-1M LiTFSI), indicating an approximate depth of 0 nm, 2.5 nm, 100 nm and 500 nm through the lithium surface. (E to F) High resolution scan of C 1s, O 1s, Li 1s and F 1s after 0, 30, 1200, 6000s itching in the viscoelastic electrolyte (4 wt% PMMA in EC/PC-1 M LiTFSI). The obtained XPS spectra were analyzed by CasaXPS software and calibrated with a hydrocarbon C 1s signal at 284.6 eV.

Fig. 55 studies consequences of suppressed electroconvective instability in viscoelastic liquid electrolytes on the stability of electrodepositon at an electrolyte electrode interface. The figure specifically compares stability of electrodeposition processes for Li and Na in control electrolytes and in electrolytes containing 4wt% PMMA at a fixed current density of 5 mA/cm^2; analogous results at a lower current density (1 mA/cm^2) are presented in the supporting materials section for

Li (Fig. 56), Na (Fig. 57), as well as for Zn and Cu (Fig. 58) anodes at 5 mA/cm^2. To facilitate these measurements, the sides and back of the cathode were covered by a polystyrene membrane to ensure that all the electrochemical processes occur on the anode-facing surface of the stainless-steel cathode. As in the tracer visualization experiments, a small amount of blue polystyrene microspheres was added in the electrolyte to interrogate fluid motions in the vicinity on the evolving metal/electrolyte interface. Results reported in Fig. 55A-D show that deposition in the control electrolyte quickly produces mossy and rough Li deposits at the stainless-steel cathode. In contrast, more controlled, denser deposition is observed in the viscoelastic electrolytes. The analogous results for Na deposition are shown in Fig. 55I-P where even more dramatic improvements in electrodeposit compactness and uniformity are observed. Similar observations of stabilized deposition in electrolytes containing 4wt% PMMA are reported for Li and Na at lower current densities, as well as for Zn and Cu. It is significant that the stabilizing effect of the polymer appears insensitive to either the chemistry of the electrolyte salt or solvent, and even to an extent the surface chemistry of the anode.

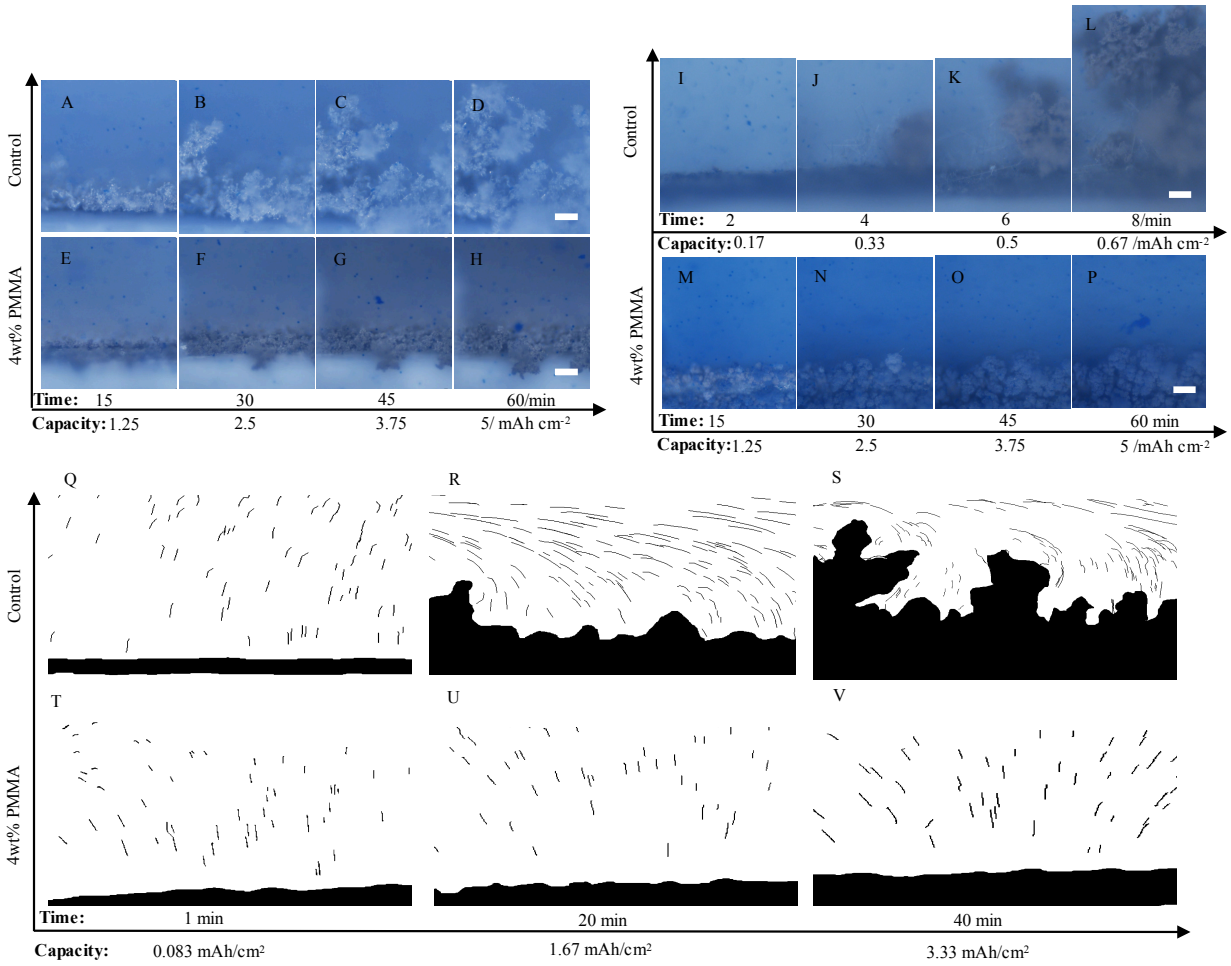

Figure 55: In situ snapshots of the electrodeposition above overlimiting current. (**A** to **D**) snapshots obtained in the Newtonian liquid electrolyte (EC/PC-1M LiTFSI) for lithium electrodeposition. (**E** to **H**) snapshots obtained in the viscoelastic electrolyte (4 wt% PMMA in EC/PC-1 M LiTFSI). (**I** to **L**) snapshots obtained in the Newtonian liquid electrolyte (EC/PC-1M $NaClO_4$) for sodium electrodeposition. (**M** to **P**) snapshots obtained in the viscoelastic electrolyte (4 wt% PMMA in EC/PC-1 M $NaClO_4$). Scale bar: 100 µm. (**Q** to **S**) Flow patterns obtained by tracking tracer particles at different stage of the lithium electrodeposition above overlimiting current in EC/PC-1M LiTFSI. (**T** to **V**) flow patterns obtained in the viscoelastic electrolyte (4 wt% PMMA in EC/PC-1 M LiTFSI).

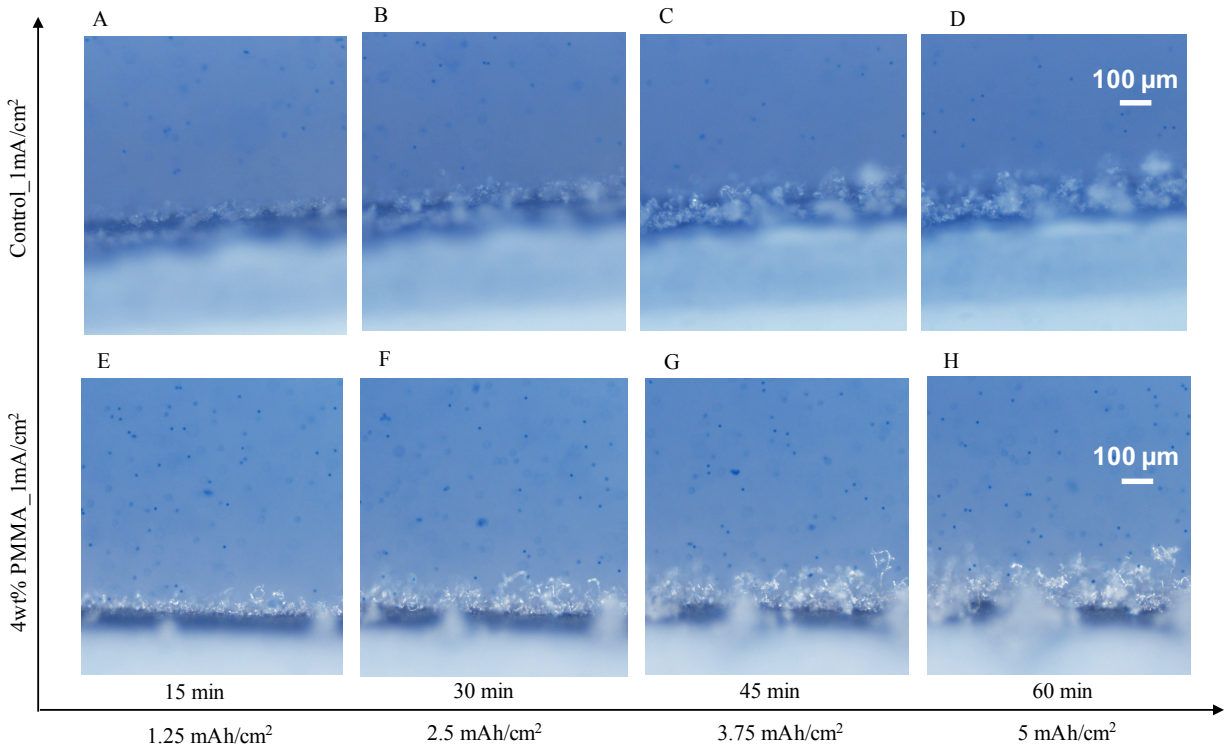

Figure 56: In situ snapshots of the growth of lithium during the electrodeposition at a low current density of 1 mA/cm^2. (**A** to **D**) snapshots obtained in the Newtonian liquid electrolyte (EC/PC-1M LiTFSI). (**E** to **H**) snapshots obtained in the viscoelastic electrolyte (4 wt% PMMA in EC/PC-1 M LiTFSI)

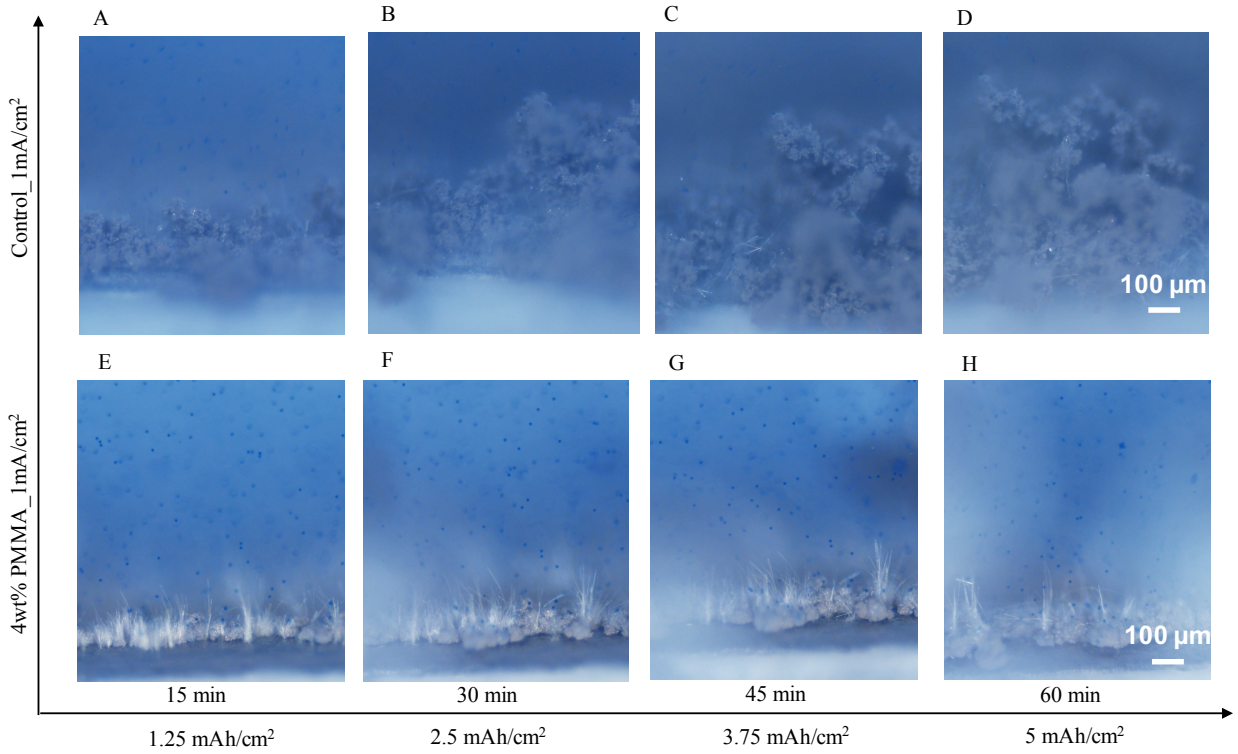

Figure 57: In situ snapshots of the growth of sodium during the electrodeposition at a low current density of 1 mA/cm^2. (**A** to **D**) snapshots obtained in the newtonian liquid electrolyte (EC/PC-1M $NaClO_4$). (**E** to **H**) snapshots obtained in the viscoelastic electrolyte (4 wt% PMMA in EC/PC-1 M $NaClO_4$).

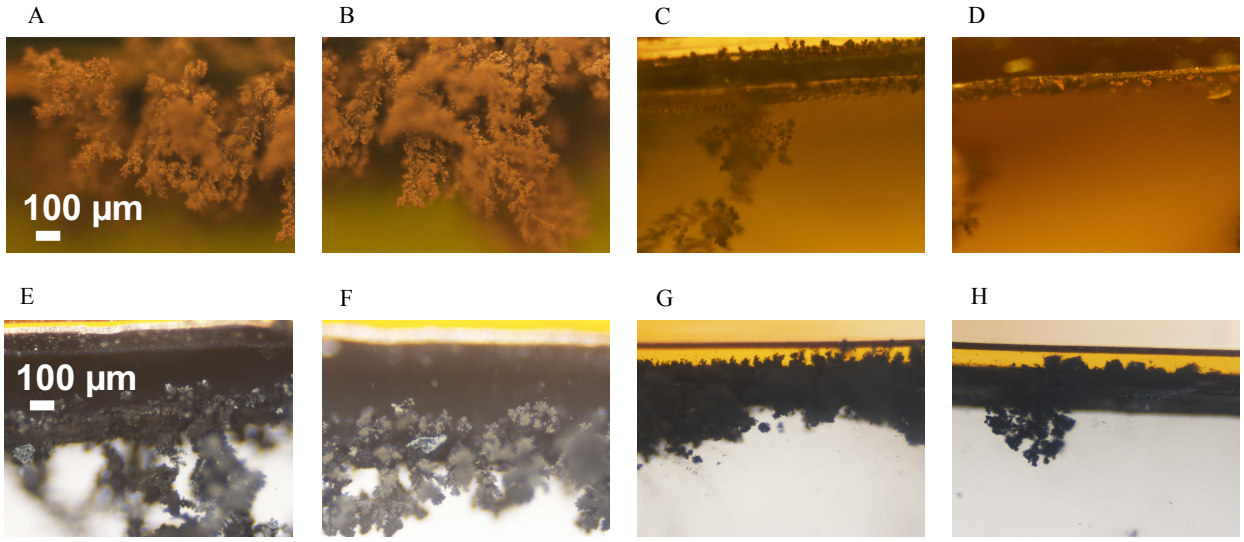

Figure 58: Photographic images of the electrodeposition of different metals. (**A** to **D**) electrodeposition of copper in (A and B) the newtonian liquid electrolyte (DMSO-0.12 M $CuCl_2$)

and (C and D) the viscoelastic electrolyte (4 wt% PMMA in DMSO-0.12 M $CuCl_2$) for one hour at 5 mA/cm^2. (**E** to **F**) electrodeposition of zinc in (E and F) the newtonian liquid electrolyte (DMSO-0.12 M $ZnCl_2$) and (G and H) the viscoelastic electrolyte (4 wt% PMMA in DMSO-0.12 M $ZnCl_2$) for one hour at 5 mA/cm^2.

Figure 55Q-V overlay evolution of the fluid velocity maps revealed by tracer particle motions with the evolution of the surface morphology in Li deposition. It is apparent from the figure that the particle trajectories for the control electrolyte evolve in an analogous manner as previously reported in the literature[164]. At short times following imposition of the current, tracer motion is slow and primarily normal to the cathode surface. At longer times and higher deposition capacities, the flow becomes more complex, and there is a substantial velocity component tangential to the electrode surface. This flow pattern simultaneously confirms the nonlinear nature of electroconvection and shows that instabilities in the process are correlated with unstable deposition. Contrary to the experiments reported by Argoul and co-workers [164], which show that streamlines always concentrate on dendrite tips, we find that tracer pathlines converge only on the fastest growing, largest dendrite tips, and may entirely bypass slow-growing dendrite tips in their vicinity. By promoting a run-away growth process for a few unstable growth modes, this observation could explain why dendritic growth results in rapid short-circuiting of lithium metal anodes. Fig. 55T-V shows that these processes are completely eliminated in electrolytes containing polymer and that tracer particles move much more slowly (see Fig. 46E) and travel primarily perpendicular to the electrode surface. In a closed cell, polymer chains near the interface are therefore subjected to a stagnation flow, which causes them to stretch and orient in the plane.

Concentration of electric field lines on fast growing dendrite tips means that analogous information about the stability of the electrodeposition process can be obtained by tracking time-dependent

growth of the dendrite front and thereby quantifying the growth rate under a range of conditions. The main results for Li and Na are summarized in Fig. 59A and B, respectively. It is seen that whereas the polymer has a very large effect on dendrite growth rate for Li at a current density above i_L, the effect is initially more modest at a current density of 1mA/cm^2, but grows with time. In contrast, for sodium electrodeposition at the same conditions, the polymer has a very noticeable and large effect on growth rate of the dendritic front at both current densities studied and at all times. Figure 59C compares the dendrite growth rates extracted from the slopes of growth versus time plots for Li, Na, Cu, and Zn electrodeposition. It is seen that in even at a concentration of 4wt% the polymer has a large and noticeable effect on dendritic growth, with the largest stabilization by far seen in Na deposition. This observation is significant because Na is commonly considered most prone to fail by dendritic deposition of all metals under consideration for energy storage in batteries both because the higher reactivity of sodium metal and the metals softness[148, 163]. The former feature makes it easier to create dendrite nuclei that grow as a result of morphological instability, while the latter makes the growing dendrite more prone to break away from the active electrode mass and to become electrochemically disconnected from the current collector in a battery. A viscoelastic liquid electrolyte may be more effective in stabilizing electrodeposition at a sodium/electrolyte interface because, in addition to the underlying ability to stabilize electroconvection, its elasticity may be beneficial for reducing the fragility of the formed SEI and for passivating the Na electrode.

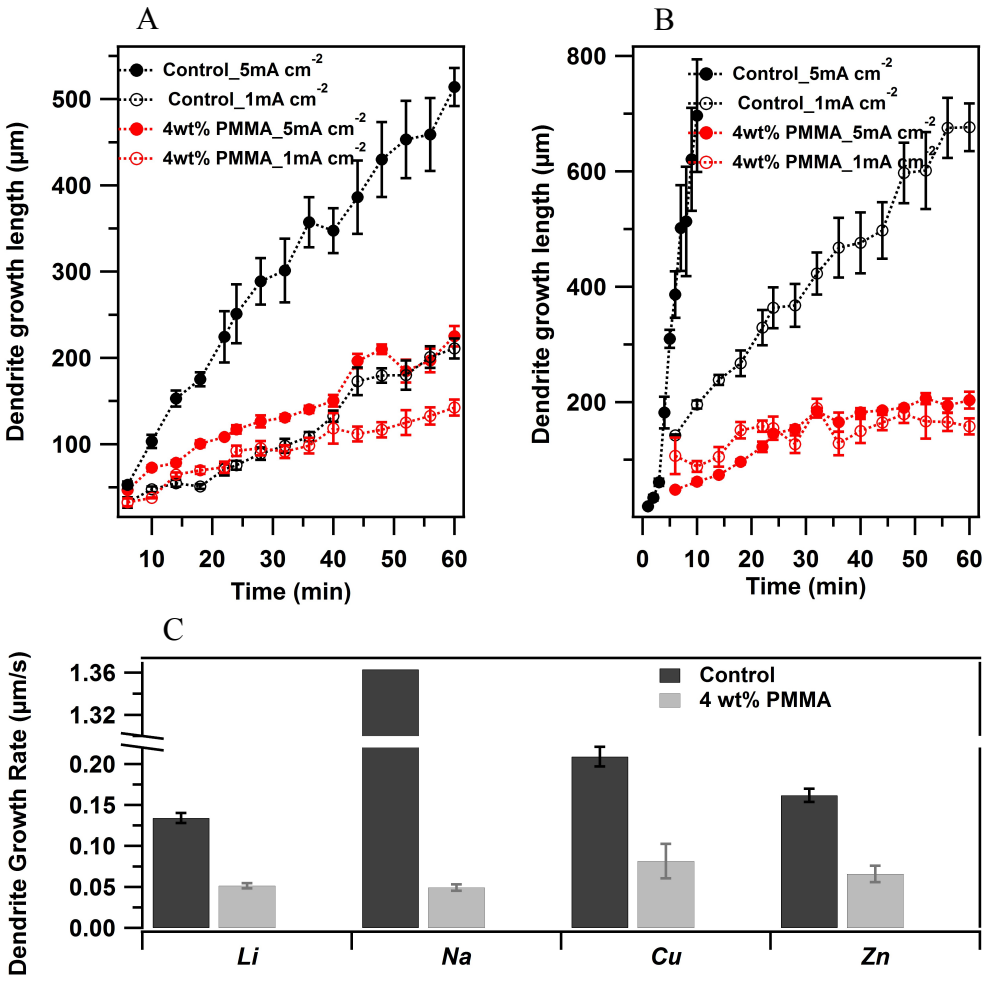

Figure 59: Analysis of the in-situ electrodepositions of different metals. (A) Lithium electrodeposition growth obtained in the Newtonian liquid electrolyte (EC/PC-1M LiTFSI) and viscoelastic electrolyte (4 wt% PMMA in EC/PC-1 M LiTFSI) at different current densities. (B) Flow velocities of the electrolytes during the lithium electrodeposition in (A). (C) Sodium electrodeposition growth obtained in the Newtonian liquid electrolyte (EC/PC-1M $NaClO_4$ and viscoelastic electrolyte (4 wt% PMMA in EC/PC-1 M $NaClO_4$) at different current densities. (D) Dendrite growth rate of different metals in the Newtonian liquid electrolyte and viscoelastic electrolyte at a current density above the overlimiting (5 mA/cm^2).

5.3 MATERIALS AND METHODS

Materials and Methods

Electrolyte preparation: All chemicals were purchased from Sigma-Aldrich unless otherwise specified and used without purification. Desired amount of polymethylmethacrylate (PMMA) (Agilent Technologies, Mp=1,568,000, M_w/M_n=1.07) was dissolved in a mixture of ethylene carbonate and propylene carbonate (EC/PC, v:v = 1 :1) with 1 M bis(trifluoromethylsulfonyl)amine lithium salt (LiTFSI) for studying lithium electrodeposition or with 1 M sodium perchlorate ($NaClO_4$) for studying sodium electrodeposition. 4 wtwt% of PMMA was dissolved in dry dimethyl sulfoxide (DMSO) with 0.12 M copper (II) chloride or zinc chloride for studying copper and zinc deposition respectively. All electrolyte preparations were performed in an argon-filled glove-box (MBraun Labmaster) and dried vigorously before using.

Electrolyte characterization: The thermal stability of the electrolytes was determined by TGA (Q5000 IR Thermogravimetric Analyzer). Ionic conductivities were measured using a Novocontrol N40 broadband dielectric spectrometer. Both Rheometrics Ares and Physica MCR501 rheometers were used to measure rheological properties of the electrolytes at room temperature. XPS measurements were performed with a Surface Science SSX-100 spectrometer using a monochromatic Al Kα source (1486.6 eV).

In-situ visualization experiment: Visualization experiments were carried out in an air-tight optical cuvette cell with two planar electrodes arranged parallel to each other. Metal ions were deposited at a constant current density on stainless steel (for lithium/sodium electrodeposition) or the metals themselves (for copper/zinc electrodeposition). Deposition was monitored in real-time by imaging the interface using an optical microscope outfitted with a video recorder.

Particle tracking: Electrodes were outlined in black against the electrolyte background via thresholding. Flow maps were formed by superimposing tracer particle trajectories on the images. *Electrochemical Measurements:* Cell assembly was carried out in an argon-filled glove-box (MBraun Labmaster) by using coin cell 2032 type. The room-temperature current-voltage characteristics of the cells were evaluated under galvanostatic conditions using Neware CT-3008 battery testers. Electrochemical impedance and lithium transference number measurement were conducted by using a Solartron Cell Test System model 1470E potentiostat/galvanostat.

6 CONCLUSION AND OUTLOOK

The author dedicatedly investigated all the components of the metal-sulfur batteries in different cell configurations during her graduate study, and made progresses on solving problems fundamentally related to both sulfur cathode dissolution and unstable electrodeposition for the metal anodes. On the cathode side, the author proposed and studied a solid-state reaction mechanism that either uses sulfur-PAN composite or sulfur-microporous carbon composite cathode and a carbonate based electrolyte. This combination allows sulfur to be reduced to solid sulfide species without formation of intermediate soluble polysulfides. This is an important improvement compared to the conventional soluble polysulfide electrochemistry because the reaction mechanism can avoid polysulfides dissolution completely, opening an opportunity for practical application of the metal-sulfur batteries. On the anode side, the author synthesized and studied different electrolyte additives as deposition stabilizer based on the stability analysis theories for the electrodepositions. The ionic liquid tethered silica nanoparticle can form an ion conducting film on the reactive metal surface that can protect metal anode and provide extra anions. Likewise, the functional ionic liquid monomers with unsaturated bonds can form polymeric film on the metal surface simultaneously during charging via electro-initiate polymerization process that can stabilized electrodeposition. Moreover, the author also fundamentally studied the hydrodynamic effects that lead to unstable electroconvection during the electrodeposition. With the addition of very small amount of extremely high molecular weight polymers like PMMA, the viscosity of the electrolyte changes greatly without obvious change in the ionic conductivity. High viscous electrolyte help slow down flow motion and decrease overlimiting conductance which proved to reduce unstable electroconvection. The author also

designed contemporary in-situ investigation methods both electrochemically and optically that allow us to make through and convincing conclusions for the phenomena and observations in the experiments.

Metal-sulfur batteries are undoubtedly the future energy storage techniques and to replace current lithium-ion batteries. Right now, there are several start-up companies tried to commercialize lithium-sulfur batteries, therefore, it is a very promising energy storage system owing to its great advantages. The future research on metal-sulfur batteries should focus on understanding the fundamental reaction mechanism and solve the drawbacks for the system not only in lab-based coin cells but also in scaled-up pouch cells. The solid-state reaction mechanism open opportunities for developing all solid-state metal sulfur batteries even with a solid gel/ceramic electrolyte, that is safer and nonflammable. Furthermore, cost analysis related to all components of the metal-sulfur batteries from synthesizing to manufacturing should be taken into consideration when developing these types of batteries.

7 REFERENCES

1. Bruce, P.G., et al., *Li-O2 and Li-S batteries with high energy storage.* Nat Mater, 2012. **11**(1): p. 19-29.
2. Dunn, B., H. Kamath, and J.-M. Tarascon, *Electrical Energy Storage for the Grid: A Battery of Choices.* Science, 2011. **334**(6058): p. 928-935.
3. Tarascon, J.M. and M. Armand, *Issues and challenges facing rechargeable lithium batteries.* Nature, 2001. **414**(6861): p. 359-367.
4. Jiang, C., E. Hosono, and H. Zhou, *Nanomaterials for lithium ion batteries.* Nano Today, 2006. **1**(4): p. 28-33.
5. Lee, K.T. and J. Cho, *Roles of nanosize in lithium reactive nanomaterials for lithium ion batteries.* Nano Today, 2011. **6**(1): p. 28-41.
6. Hassoun, J. and B. Scrosati, *Moving to a solid-state configuration: a valid approach to making lithium-sulfur batteries viable for practical applications.* Adv Mater, 2010. **22**(45): p. 5198-201.
7. Yang, Z., et al., *In situ synthesis of lithium sulfide–carbon composites as cathode materials for rechargeable lithium batteries.* Journal of Materials Chemistry A, 2013. **1**(4): p. 1433.
8. Miller TJ (2009) Electrical Energy Storage for Vehicles: Targets and Metrics, Ford Motor Company

9. Gao, J. and H.D. Abruña, *Key Parameters Governing the Energy Density of Rechargeable Li/S Batteries.* The Journal of Physical Chemistry Letters, 2014. **5**(5): p. 882-885.

10. Meyer, B., *Solid Allotropes of Sulfur.* Chemical Reviews, 1964. **64**(4): p. 429-451.

11. Akridge, J.R., Y.V. Mikhaylik, and N. White, *Li/S fundamental chemistry and application to high-performance rechargeable batteries.* Solid State Ionics, 2004. **175**(1-4): p. 243-245.

12. Wang, J., *Sulfur-mesoporous carbon composites in conjunction with a novel ionic liquid electrolyte for lithium rechargeable batteries.* Carbon, 2008. **46**: p. 229-235.

13. Jayaprakash, N., et al., *Porous Hollow Carbon@Sulfur Composites for High-Power Lithium–Sulfur Batteries.* Angewandte Chemie International Edition, 2011. **50**(26): p. 5904-5908.

14. Zeng, Q., et al., *Synergy of nanoconfinement and surface oxygen in recrystallization of sulfur melt in carbon nanocapsules and the related Li–S cathode properties.* Journal of Materials Chemistry A, 2014. **2**(18): p. 6439.

15. Cunningham, P.T., S.A. Johnson, and E.J. Cairns, *Phase equilibria in lithium-chalcogen systems: Lithium-sulfur.* J. Electrochem. Soc., 1972. **119**: p. 1448-1450.

16. Choi, J.W., *Rechargeable lithium/sulfur battery with suitable mixed liquid electrolytes.* Electrochim. Acta, 2007. **52**: p. 2075-2082.

17. Li, Z., et al., *A Highly Ordered Meso@Microporous Carbon-Supported Sulfur@Smaller Sulfur Core–Shell Structured Cathode for Li–S Batteries.* ACS Nano, 2014. **8**(9): p. 9295-9303.

18. Zhang, X.-Q., et al., *Synthesis of superior carbon nanofibers with large aspect ratio and tunable porosity for electrochemical energy storage.* Journal of Materials Chemistry A, 2013. **1**(33): p. 9449-9455.

19. Wu, H.B., et al., *Embedding Sulfur in MOF-Derived Microporous Carbon Polyhedrons for Lithium–Sulfur Batteries.* Chemistry – A European Journal, 2013. **19**(33): p. 10804-10808.

20. Xin, S., et al., *Smaller sulfur molecules promise better lithium-sulfur batteries.* J Am Chem Soc, 2012. **134**(45): p. 18510-3.

21. Bruce, P.G., *Energy storage beyond the horizon: Rechargeable lithium batteries.* Solid State Ionics, 2008. **179**(21–26): p. 752-760.

22. Zhang, B., et al., *Enhancement of long stability of sulfur cathode by encapsulating sulfur into micropores of carbon spheres.* Energy & Environmental Science, 2010. **3**(10): p. 1531-1537.

23. Zheng, G., et al., *Interconnected hollow carbon nanospheres for stable lithium metal anodes.* Nat Nano, 2014. **9**(8): p. 618-623.

24. Tao, X., et al., *Highly mesoporous carbon foams synthesized by a facile, cost-effective and template-free Pechini method for advanced lithium-sulfur batteries.* Journal of Materials Chemistry A, 2013. **1**(10): p. 3295-3301.

25. Schuster, J., et al., *Spherical Ordered Mesoporous Carbon Nanoparticles with High Porosity for Lithium–Sulfur Batteries.* Angewandte Chemie International Edition, 2012. **51**(15): p. 3591-3595.

26. Liang, X., et al., *A nano-structured and highly ordered polypyrrole-sulfur cathode for lithium–sulfur batteries.* Journal of Power Sources, 2011. **196**(16): p. 6951-6955.

27. Wang, J.L., et al., *Sulfur–carbon nano-composite as cathode for rechargeable lithium battery based on gel electrolyte.* Electrochemistry Communications, 2002. **4**(6): p. 499-502.

28. Wang, J., et al., *Polymer lithium cells with sulfur composites as cathode materials.* Electrochimica Acta, 2003. **48**(13): p. 1861-1867.

29. Lai, C., et al., *Synthesis and Electrochemical Performance of Sulfur/Highly Porous Carbon Composites.* The Journal of Physical Chemistry C, 2009. **113**(11): p. 4712-4716.

30. Kittel, C., *Introduction to solid state physics*. 2005, Wiley: Hoboken, NJ :.

31. Guo, J., Y. Xu, and C. Wang, *Sulfur-Impregnated Disordered Carbon Nanotubes Cathode for Lithium–Sulfur Batteries.* Nano Letters, 2011. **11**(10): p. 4288-4294.

32. Sun, L., et al., *Sulfur Nanocrystals Confined in Carbon Nanotube Network As a Binder-Free Electrode for High-Performance Lithium Sulfur Batteries.* Nano Letters, 2014. **14**(7): p. 4044-4049.

33. Zhao, Y., et al., *Encapsulating MWNTs into Hollow Porous Carbon Nanotubes: A Tube-in-Tube Carbon Nanostructure for High-Performance Lithium-Sulfur Batteries.* Advanced Materials, 2014. **26**(30): p. 5113-5118.

34. Zheng, G., et al., *Amphiphilic Surface Modification of Hollow Carbon Nanofibers for Improved Cycle Life of Lithium Sulfur Batteries.* Nano Letters, 2013. **13**(3): p. 1265-1270.

35. Xiao, L., et al., *A Soft Approach to Encapsulate Sulfur: Polyaniline Nanotubes for Lithium-Sulfur Batteries with Long Cycle Life.* Advanced Materials, 2012. **24**(9): p. 1176-1181.

36. Fu, Y. and A. Manthiram, *Enhanced Cyclability of Lithium–Sulfur Batteries by a Polymer Acid-Doped Polypyrrole Mixed Ionic–Electronic Conductor.* Chemistry of Materials, 2012. **24**(15): p. 3081-3087.

37. Wu, F., et al., *Sulfur/Polythiophene with a Core/Shell Structure: Synthesis and Electrochemical Properties of the Cathode for Rechargeable Lithium Batteries.* The Journal of Physical Chemistry C, 2011. **115**(13): p. 6057-6063.

38. Fanous, J., et al., *Structure-Related Electrochemistry of Sulfur-Poly(acrylonitrile) Composite Cathode Materials for Rechargeable Lithium Batteries.* Chemistry of Materials, 2011. **23**(22): p. 5024-5028.

39. Li, W., et al., *High-performance hollow sulfur nanostructured battery cathode through a scalable, room temperature, one-step, bottom-up approach.* Proceedings of the National Academy of Sciences, 2013. **110**(18): p. 7148-7153.

40. Yang, Y., et al., *Improving the Performance of Lithium-Sulfur Batteries by Conductive Polymer Coating.* ACS NANO, 2011. **5**(11): p. 9187-9193.

41. Fu, Y. and A. Manthiram, *Orthorhombic Bipyramidal Sulfur Coated with Polypyrrole Nanolayers As a Cathode Material for Lithium–Sulfur Batteries.* The Journal of Physical Chemistry C, 2012. **116**(16): p. 8910-8915.

42. Zhang, Y., et al., *One-step synthesis of branched sulfur/polypyrrole nanocomposite cathode for lithium rechargeable batteries.* Journal of Power Sources, 2012. **208**: p. 1-8.

43. Liang, X., et al., *A composite of sulfur and polypyrrole–multi walled carbon combinatorial nanotube as cathode for Li/S battery.* Journal of Power Sources, 2012. **206**: p. 409-413.

44. Qiu, L., et al., *Preparation and enhanced electrochemical properties of nano-sulfur/poly(pyrrole-co-aniline) cathode material for lithium/sulfur batteries.* Electrochimica Acta, 2010. **55**(15): p. 4632-4636.

45. Ji, X., K.T. Lee, and L.F. Nazar, *A highly ordered nanostructured carbon-sulphur cathode for lithium-sulphur batteries.* Nat Mater, 2009. **8**(6): p. 500-506.

46. Hueso, K.B., M. Armand, and T. Rojo, *High temperature sodium batteries: status, challenges and future trends.* Energy & Environmental Science, 2013. **6**(3): p. 734-749.

47. Sudworth, J.L., *The sodium sulfur battery*, A.R. Tilley, Editor. 1985, Chapman & Hall: London ;.

48. Xin, S., et al., *A High-Energy Room-Temperature Sodium-Sulfur Battery.* Advanced Materials, 2014. **26**(8): p. 1261-1265.

49. Xin, S., et al., *Smaller Sulfur Molecules Promise Better Lithium–Sulfur Batteries.* Journal of the American Chemical Society, 2012. **134**(45): p. 18510-18513.

50. Wang, J., et al., *A Novel Conductive Polymer–Sulfur Composite Cathode Material for Rechargeable Lithium Batteries.* Advanced Materials, 2002. **14**(13-14): p. 963-965.

51. Yu, X.-g., et al., *Lithium storage in conductive sulfur-containing polymers.* Journal of Electroanalytical Chemistry, 2004. **573**(1): p. 121-128.

52. Liu, Z., et al., *Lyotropic Liquid Crystal of Polyacrylonitrile-Grafted Graphene Oxide and Its Assembled Continuous Strong Nacre-Mimetic Fibers.* Macromolecules, 2013. **46**(17): p. 6931-6941.

53. Burkhardt, S.E., et al., *Towards organic energy storage: characterization of 2,5-bis(methylthio)thieno[3,2-b]thiophene.* Journal of Materials Chemistry, 2011. **21**(26): p. 9553-9563.

54. Evers, S., T. Yim, and L.F. Nazar, *Understanding the Nature of Absorption/Adsorption in Nanoporous Polysulfide Sorbents for the Li–S Battery.* The Journal of Physical Chemistry C, 2012. **116**(37): p. 19653-19658.

55. Hwang, D., *Positive electrode for lithium-sulfur battery and lithium-sulfur battery comprising same*. 2004, Google Patents.

56. Li, J., et al., *A sulfur–polyacrylonitrile/graphene composite cathode for lithium batteries with excellent cyclability.* Journal of Power Sources, 2014. **252**(0): p. 107-112.

57. Zhang, Y.Z., et al., *Sulfur/polyacrylonitrile/carbon multi-composites as cathode materials for lithium/sulfur battery in the concentrated electrolyte.* Journal of Materials Chemistry A, 2014. **2**(13): p. 4652-4659.

58. Guo, J., et al., *Lithium–Sulfur Battery Cathode Enabled by Lithium–Nitrile Interaction.* Journal of the American Chemical Society, 2013. **135**(2): p. 763-767.

59. Ma, L., et al., *Tethered Molecular Sorbents: Enabling Metal-Sulfur Battery Cathodes.* Advanced Energy Materials, 2014. **4**(17): p. n/a-n/a.

60. Hwang, T.H., et al., *One-Dimensional Carbon–Sulfur Composite Fibers for Na–S Rechargeable Batteries Operating at Room Temperature.* Nano Letters, 2013. **13**(9): p. 4532-4538.

61. Yu, X., et al., *Stable-cycle and high-capacity conductive sulfur-containing cathode materials for rechargeable lithium batteries.* Journal of Power Sources, 2005. **146**(1–2): p. 335-339.

62. Yin, L., et al., *Polyacrylonitrile/graphene composite as a precursor to a sulfur-based cathode material for high-rate rechargeable Li-S batteries.* Energy & Environmental Science, 2012. **5**(5): p. 6966-6972.

63. Mo, Y., et al., *Preparation and tribological performance of chemically-modified reduced graphene oxide/polyacrylonitrile composites.* Composites Part A: Applied Science and Manufacturing, 2013. **54**(0): p. 153-158.

64. Luo, C., et al., *Carbonized Polyacrylonitrile-Stabilized SeSx Cathodes for Long Cycle Life and High Power Density Lithium Ion Batteries.* Advanced Functional Materials, 2014. **24**(26): p. 4082-4089.

65. Ye, J., et al., *Sulfur/carbon nanocomposite-filled polyacrylonitrile nanofibers as a long life and high capacity cathode for lithium-sulfur batteries.* Journal of Materials Chemistry A, 2015. **3**(14): p. 7406-7412.

66. Ji, L., et al., *Graphene oxide as a sulfur immobilizer in high performance lithium/sulfur cells.* J Am Chem Soc, 2011. **133**(46): p. 18522-5.

67. Sun, H., et al., *A composite material of uniformly dispersed sulfur on reduced graphene oxide: Aqueous one-pot synthesis, characterization and excellent performance as the*

cathode in rechargeable lithium-sulfur batteries. Nano Research, 2012. **5**(10): p. 726-738.

68. Zhang, F.-f., et al., *Facile and effective synthesis of reduced graphene oxide encapsulated sulfur via oil/water system for high performance lithium sulfur cells.* Journal of Materials Chemistry, 2012. **22**(23): p. 11452.

69. Zhang, L., et al., *Electronic structure and chemical bonding of a graphene oxide-sulfur nanocomposite for use in superior performance lithium-sulfur cells.* Phys Chem Chem Phys, 2012. **14**(39): p. 13670-5.

70. Wang, Z., et al., *Enhancing lithium–sulphur battery performance by strongly binding the discharge products on amino-functionalized reduced graphene oxide.* Nat Commun, 2014. **5**.

71. Moon, S., et al., *Encapsulated Monoclinic Sulfur for Stable Cycling of Li–S Rechargeable Batteries.* Advanced Materials, 2013. **25**(45): p. 6547-6553.

72. Guo, J., et al., *Lithium–Sulfur Battery Cathode Enabled by Lithium–Nitrile Interaction.* Journal of the American Chemical Society, 2012. **135**(2): p. 763-767.

73. Ma, L., et al., *Nanomaterials: Science and applications in the lithium–sulfur battery.* Nano Today, 2015. **10**(3): p. 315-338.

74. Armand, M. and J.M. Tarascon, *Building better batteries.* Nature, 2008. **451**(7179): p. 652-657.

75. WHITTINGHAM, M.S., *Electrical Energy Storage and Intercalation Chemistry.* Science, 1976. **192**(4244): p. 1126-1127.

76. Bruce, P.G., et al., *Li-O2 and Li-S batteries with high energy storage.* Nat Mater, 2012. **11**(1): p. 19-29.

77. Manthiram, A., S.-H. Chung, and C. Zu, *Lithium–Sulfur Batteries: Progress and Prospects.* Advanced Materials, 2015. **27**(12): p. 1980-2006.

78. Zhao, Q., et al., *Sulfur Nanodots Electrodeposited on Ni Foam as High-Performance Cathode for Li–S Batteries.* Nano Letters, 2015. **15**(1): p. 721-726.

79. Aurbach, D., et al., *Prototype systems for rechargeable magnesium batteries.* Nature, 2000. **407**(6805): p. 724-727.

80. Lin, M.-C., et al., *An ultrafast rechargeable aluminium-ion battery.* Nature, 2015. **520**(7547): p. 324-328.

81. Yabuuchi, N., et al., *P2-type Nax[Fe1/2Mn1/2]O2 made from earth-abundant elements for rechargeable Na batteries.* Nat Mater, 2012. **11**(6): p. 512-517.

82. Manthiram, A. and X. Yu, *Ambient Temperature Sodium–Sulfur Batteries.* Small, 2015. **11**(18): p. 2108-2114.

83. Adelhelm, P., et al., *From lithium to sodium: cell chemistry of room temperature sodium–air and sodium–sulfur batteries.* Beilstein Journal of Nanotechnology, 2015. **6**: p. 1016-1055.

84. Yang, Y., G. Zheng, and Y. Cui, *Nanostructured sulfur cathodes.* Chemical Society Reviews, 2013. **42**(7): p. 3018-3032.

85. Manthiram, A., et al., *Rechargeable Lithium–Sulfur Batteries.* Chemical Reviews, 2014. **114**(23): p. 11751-11787.

86. Yin, Y.-X., et al., *Lithium–Sulfur Batteries: Electrochemistry, Materials, and Prospects.* Angewandte Chemie International Edition, 2013. **52**(50): p. 13186-13200.

87. Hartmann, P., et al., *A rechargeable room-temperature sodium superoxide (NaO2) battery.* Nat Mater, 2013. **12**(3): p. 228-232.

88. Yang, C.-P., et al., *Electrochemical (De)Lithiation of 1D Sulfur Chains in Li–S Batteries: A Model System Study.* Journal of the American Chemical Society, 2015. **137**(6): p. 2215-2218.

89. Zhang, S., et al., *Recent Advances in Electrolytes for Lithium–Sulfur Batteries.* Advanced Energy Materials, 2015: p. n/a-n/a.

90. Lu, Y., et al., *Ionic-Liquid–Nanoparticle Hybrid Electrolytes: Applications in Lithium Metal Batteries.* Angewandte Chemie International Edition, 2014. **53**(2): p. 488-492.

91. Lu, Y., et al., *Ionic liquid-nanoparticle hybrid electrolytes and their application in secondary lithium-metal batteries.* Adv Mater, 2012. **24**(32): p. 4430-5.

92. Lu, Y., Z. Tu, and L.A. Archer, *Stable lithium electrodeposition in liquid and nanoporous solid electrolytes.* Nat Mater, 2014. **13**(10): p. 961-969.

93. Slater, A.G. and A.I. Cooper, *Function-led design of new porous materials.* Science, 2015. **348**(6238).

94. Cravillon, J., et al., *Controlling Zeolitic Imidazolate Framework Nano- and Microcrystal Formation: Insight into Crystal Growth by Time-Resolved In Situ Static Light Scattering.* Chemistry of Materials, 2011. **23**(8): p. 2130-2141.

95. Erlich, R.H. and A.I. Popov, *Spectroscopic studies of ionic solvation. X. Study of the solvation of sodium ions in nonaqueous solvents by sodium-23 nuclear magnetic resonance.* Journal of the American Chemical Society, 1971. **93**(22): p. 5620-5623.

96. Ong, S.P., et al., *Voltage, stability and diffusion barrier differences between sodium-ion and lithium-ion intercalation materials.* Energy & Environmental Science, 2011. **4**(9): p. 3680-3688.

97. Cohn, G., L. Ma, and L.A. Archer, *A novel non-aqueous aluminum sulfur battery.* Journal of Power Sources, 2015. **283**: p. 416-422.

98. Liang, X., et al., *A highly efficient polysulfide mediator for lithium–sulfur batteries.* Nat Commun, 2015. **6**.

99. Manan, N.S.A., et al., *Electrochemistry of Sulfur and Polysulfides in Ionic Liquids.* The Journal of Physical Chemistry B, 2011. **115**(47): p. 13873-13879.

100. Weppner, W. and R.A. Huggins, *Determination of the Kinetic Parameters of Mixed - Conducting Electrodes and Application to the System Li3Sb.* Journal of The Electrochemical Society, 1977. **124**(10): p. 1569-1578.

101. Kamlet, M.J., et al., *Linear solvation energy relationships. 13. Relationship between the Hildebrand solubility parameter, .delta.H, and the solvatochromic parameter, .pi.*.* Journal of the American Chemical Society, 1981. **103**(20): p. 6062-6066.

102. Lu, Y., et al., *Ionic liquid-nanoparticle hybrid electrolytes.* Journal of Materials Chemistry, 2012. **22**(9): p. 4066-4072.

103. Wu, X., et al., *Unraveling the storage mechanism in organic carbonyl electrodes for sodium-ion batteries.* Science Advances, 2015. **1**(8).

104. Wei, S., et al., *A stable room-temperature sodium-sulfur battery.* Nat Commun, 2016. **7**.

105. Slater, M.D., et al., *Sodium-Ion Batteries.* Advanced Functional Materials, 2013. **23**(8): p. 947-958.

106. Kundu, D., et al., *The Emerging Chemistry of Sodium Ion Batteries for Electrochemical Energy Storage.* Angewandte Chemie International Edition, 2015. **54**(11): p. 3431-3448.

107. Kim, S.-W., et al., *Electrode Materials for Rechargeable Sodium-Ion Batteries: Potential Alternatives to Current Lithium-Ion Batteries.* Advanced Energy Materials, 2012. **2**(7): p. 710-721.

108. Xu, S., et al., *The Sodium–Oxygen/Carbon Dioxide Electrochemical Cell.* ChemSusChem, 2016: p. n/a-n/a.

109. Yu, X. and A. Manthiram, *Ambient-Temperature Sodium–Sulfur Batteries with a Sodiated Nafion Membrane and a Carbon Nanofiber-Activated Carbon Composite Electrode.* Advanced Energy Materials, 2015. **5**(12): p. n/a-n/a.

110. Seh, Z.W., et al., *A Highly Reversible Room-Temperature Sodium Metal Anode.* ACS Central Science, 2015. **1**(8): p. 449-455.

111. Basile, A., A.I. Bhatt, and A.P. O/'Mullane, *Stabilizing lithium metal using ionic liquids for long-lived batteries.* Nat Commun, 2016. **7**.

112. Wang, Z., et al., *Vinyl-functionalized imidazolium ionic liquids as new electrolyte additives for high-voltage Li-ion batteries.* Journal of Solid State Electrochemistry, 2013. **17**(11): p. 2839-2848.

113. Rogers, R.D. and K.R. Seddon, *Ionic Liquids--Solvents of the Future?* Science, 2003. **302**(5646): p. 792-793.

114. Tikekar, M.D., L.A. Archer, and D.L. Koch, *Stabilizing electrodeposition in elastic solid electrolytes containing immobilized anions.* Science Advances, 2016. **2**(7).

115. Tu, Z., et al., *Nanostructured Electrolytes for Stable Lithium Electrodeposition in Secondary Batteries.* Accounts of Chemical Research, 2015. **48**(11): p. 2947-2956.

116. Khurana, R., et al., *Suppression of Lithium Dendrite Growth Using Cross-Linked Polyethylene/Poly(ethylene oxide) Electrolytes: A New Approach for Practical Lithium-Metal Polymer Batteries.* Journal of the American Chemical Society, 2014. **136**(20): p. 7395-7402.

117. Cheng, X.-B., et al., *Dendrite-Free Lithium Deposition Induced by Uniformly Distributed Lithium Ions for Efficient Lithium Metal Batteries.* Advanced Materials, 2016. **28**(15): p. 2888-2895.

118. Tikekar, M.D., et al., *Design principles for electrolytes and interfaces for stable lithium-metal batteries.* Nature Energy, 2016. **1**: p. 16114.

119. Tikekar, M.D., L.A. Archer, and D.L. Koch, *Stability Analysis of Electrodeposition across a Structured Electrolyte with Immobilized Anions.* Journal of The Electrochemical Society, 2014. **161**(6): p. A847-A855.

120. Si, P., et al., *Functional Polythiophene Nanoparticles: Size-Controlled Electropolymerization and Ion Selective Response.* Journal of the American Chemical Society, 2007. **129**(13): p. 3888-3896.

121. Lee, S., et al., *Electropolymerization of a Bifunctional Ionic Liquid Monomer Yields an Electroactive Liquid-Crystalline Polymer.* Advanced Functional Materials, 2010. **20**(13): p. 2063-2070.

122. Susan, M.A.B.H., et al., *Ion Gels Prepared by in Situ Radical Polymerization of Vinyl Monomers in an Ionic Liquid and Their Characterization as Polymer Electrolytes.* Journal of the American Chemical Society, 2005. **127**(13): p. 4976-4983.

123. Hulvat, J.F. and S.I. Stupp, *Liquid-Crystal Templating of Conducting Polymers.* Angewandte Chemie International Edition, 2003. **42**(7): p. 778-781.

124. Ohno, H., *Functional Design of Ionic Liquids.* Bulletin of the Chemical Society of Japan, 2006. **79**(11): p. 1665-1680.

125. Ohno, H., *Design of Ion Conductive Polymers Based on Ionic Liquids.* Macromolecular Symposia, 2007. **249-250**(1): p. 551-556.

126. Jimenez-Solomon, M.F., et al., *Polymer nanofilms with enhanced microporosity by interfacial polymerization.* Nat Mater, 2016. **advance online publication**.

127. Fréchet, J.M.J., et al., *Self-Condensing Vinyl Polymerization: An Approach to Dendritic Materials.* Science, 1995. **269**(5227): p. 1080-1083.

128. Aurbach, D., Y. Gofer, and J. Langzam, *The Correlation Between Surface Chemistry, Surface Morphology, and Cycling Efficiency of Lithium Electrodes in a Few Polar Aprotic Systems.* Journal of The Electrochemical Society, 1989. **136**(11): p. 3198-3205.

129. Yui, Y., M. Hayashi, and J. Nakamura, *In situ Microscopic Observation of Sodium Deposition/Dissolution on Sodium Electrode.* Scientific Reports, 2016. **6**: p. 22406.

130. Tu, Z., et al., *Nanoporous Polymer-Ceramic Composite Electrolytes for Lithium Metal Batteries.* Advanced Energy Materials, 2014. **4**(2): p. n/a-n/a.

131. Monroe, C. and J. Newman, *The Impact of Elastic Deformation on Deposition Kinetics at Lithium/Polymer Interfaces.* Journal of The Electrochemical Society, 2005. **152**(2): p. A396-A404.

132. Gao, H., et al., *A Composite Gel–Polymer/Glass–Fiber Electrolyte for Sodium-Ion Batteries.* Advanced Energy Materials, 2015. **5**(9): p. n/a-n/a.

133. Nishikawa, K., et al., *In Situ Observation of Dendrite Growth of Electrodeposited Li Metal.* Journal of The Electrochemical Society, 2010. **157**(11): p. A1212-A1217.

134. Men, S., K.R.J. Lovelock, and P. Licence, *X-ray photoelectron spectroscopy of pyrrolidinium-based ionic liquids: cation-anion interactions and a comparison to imidazolium-based analogues.* Physical Chemistry Chemical Physics, 2011. **13**(33): p. 15244-15255.

135. Fang, Y., et al., *Hierarchical Carbon Framework Wrapped Na3V2(PO4)3 as a Superior High-Rate and Extended Lifespan Cathode for Sodium-Ion Batteries.* Advanced Materials, 2015. **27**(39): p. 5895-5900.

136. Ren, W., et al., *Self-sacrificed synthesis of three-dimensional Na3V2(PO4)3 nanofiber network for high-rate sodium–ion full batteries.* Nano Energy, 2016. **25**: p. 145-153.

137. Zhu, C., et al., *High Power–High Energy Sodium Battery Based on Threefold Interpenetrating Network.* Advanced Materials, 2016. **28**(12): p. 2409-2416.

138. Hung, T.-F., et al., *Ascorbic Acid-Assisted Synthesis of Mesoporous Sodium Vanadium Phosphate Nanoparticles with Highly sp2-Coordinated Carbon Coatings as Efficient Cathode Materials for Rechargeable Sodium-Ion Batteries.* Chemistry – A European Journal, 2016. **22**(30): p. 10620-10626.

139. Chotard, J.-N., et al., *Discovery of a Sodium-Ordered Form of Na3V2(PO4)3 below Ambient Temperature.* Chemistry of Materials, 2015. **27**(17): p. 5982-5987.

140. Etacheri, V., et al., *Effect of Fluoroethylene Carbonate (FEC) on the Performance and Surface Chemistry of Si-Nanowire Li-Ion Battery Anodes.* Langmuir, 2012. **28**(1): p. 965-976.

141. Nakai, H., et al., *Investigation of the Solid Electrolyte Interphase Formed by Fluoroethylene Carbonate on Si Electrodes.* Journal of The Electrochemical Society, 2011. **158**(7): p. A798-A801.

142. Wei, S., et al., *Metal–Sulfur Battery Cathodes Based on PAN–Sulfur Composites.* Journal of the American Chemical Society, 2015. **137**(37): p. 12143-12152.

143. Schlesinger, M., *Electroless and Electrodeposition of Silver*, in *Modern Electroplating*. 2010, John Wiley & Sons, Inc. p. 131-138.

144. *Electrodeposition of Alloys: PRINCIPLES and PRACTICE A2 - Brenner, Abner*, in *Electrodeposition of Alloys*. 1963, Academic Press. p. ii.

145. Trau, M., D.A. Saville, and I.A. Aksay, *Field-Induced Layering of Colloidal Crystals.* Science, 1996. **272**(5262): p. 706-709.

146. Low, C.T.J., R.G.A. Wills, and F.C. Walsh, *Electrodeposition of composite coatings containing nanoparticles in a metal deposit.* Surface and Coatings Technology, 2006. **201**(1): p. 371-383.

147. Beck, F., *Electrodeposition of polymer coatings.* Electrochimica Acta, 1988. **33**(7): p. 839-850.

148. Wei, S., et al., *Highly Stable Sodium Batteries Enabled by Functional Ionic Polymer Membranes.* Advanced Materials, 2017. **29**(12): p. 1605512-1605519.

149. Aogaki, R. and T. Makino, *Theory of powdered metal formation in electrochemistry—morphological instability in galvanostatic crystal growth under diffusion control*. Vol. 26. 1981. 1509-1517.

150. Cowan, D.A. and J.H. Brown, *Effect of Turbulence on Limiting Current in Electrodialysis Cells.* Industrial & Engineering Chemistry, 1959. **51**(12): p. 1445-1448.

151. Fleury, V., *Branched fractal patterns in non-equilibrium electrochemical deposition from oscillatory nucleation and growth.* Nature, 1997. **390**(6656): p. 145-148.

152. Rubinstein, I. and B. Zaltzman, *Electro-osmotically induced convection at a permselective membrane.* Physical Review E, 2000. **62**(2): p. 2238-2251.

153. Zaltzman, B. and I. Rubinstein, *Electro-osmotic slip and electroconvective instability.* Journal of Fluid Mechanics, 2007. **579**: p. 173-226.

154. Chazalviel, J.N., *Electrochemical aspects of the generation of ramified metallic electrodeposits.* Physical Review A, 1990. **42**(12): p. 7355-7367.

155. Rosso, M., J.N. Chazalviel, and E. Chassaing, *Calculation of the space charge in electrodeposition from a binary electrolyte.* Journal of Electroanalytical Chemistry, 2006. **587**(2): p. 323-328.

156. Druzgalski, C.L., M.B. Andersen, and A. Mani, *Direct numerical simulation of electroconvective instability and hydrodynamic chaos near an ion-selective surface.* Physics of Fluids, 2013. **25**(11): p. 110804.

157. Bai, P., et al., *Transition of lithium growth mechanisms in liquid electrolytes.* Energy & Environmental Science, 2016. **9**(10): p. 3221-3229.

158. Wang, M., et al., *Formation of a mesh-like electrodeposit induced by electroconvection.* Nature, 1994. **367**(6462): p. 438-441.

159. Rubinstein, I., E. Staude, and O. Kedem, *Role of the membrane surface in concentration polarization at ion-exchange membrane.* Desalination, 1988. **69**(2): p. 101-114.

160. Maletzki, F., H.W. Rösler, and E. Staude, *Ion transfer across electrodialysis membranes in the overlimiting current range: stationary voltage current characteristics and current noise power spectra under different conditions of free convection.* Journal of Membrane Science, 1992. **71**(1): p. 105-116.

161. Rubinshtein, I., et al., *Experimental Verification of the Electroosmotic Mechanism of Overlimiting Conductance Through a Cation Exchange Electrodialysis Membrane.* Russian Journal of Electrochemistry, 2002. **38**(8): p. 853-863.

162. Kang, K., et al., *Electrodes with High Power and High Capacity for Rechargeable Lithium Batteries.* Science, 2006. **311**(5763): p. 977-980.

163. Wei, S., et al., *A stable room-temperature sodium–sulfur battery.* Nature Communications, 2016. **7**: p. 11722.

164. Huth, J.M., et al., *Role of convection in thin-layer electrodeposition.* Physical Review E, 1995. **51**(4): p. 3444-3458.

165. Lumley, J.L., *Drag reduction in turbulent flow by polymer additives.* Journal of Polymer Science: Macromolecular Reviews, 1973. **7**(1): p. 263-290.

166. White, C.M. and M.G. Mungal, *Mechanics and Prediction of Turbulent Drag Reduction with Polymer Additives.* Annual Review of Fluid Mechanics, 2008. **40**(1): p. 235-256.

167. Manuel Stephan, A., *Review on gel polymer electrolytes for lithium batteries.* European Polymer Journal, 2006. **42**(1): p. 21-42.

168. Croce, F., et al., *Nanocomposite polymer electrolytes for lithium batteries.* Nature, 1998. **394**(6692): p. 456-458.

169. Le Thai, M., et al., *100k Cycles and Beyond: Extraordinary Cycle Stability for MnO2 Nanowires Imparted by a Gel Electrolyte.* ACS Energy Letters, 2016. **1**(1): p. 57-63.

170. Rubinstein, M. and R.H. Colby, *Polymer Physics*. 2003: OUP Oxford.

171. Saha, S. and L.A. Archer, *Electric Birefringence of Electrolytes near Charged Surfaces, II: Effect of Polymeric Additives.* The Journal of Physical Chemistry C, 2007. **111**(39): p. 14365-14370.

172. Saha, S. and L.A. Archer, *Electric Birefringence of Electrolytes near Charged Surfaces, I.* The Journal of Physical Chemistry C, 2007. **111**(39): p. 14358-14364.

173. Bouchet, R., S. Lascaud, and M. Rosso, *An EIS Study of the Anode Li/PEO-LiTFSI of a Li Polymer Battery.* Journal of The Electrochemical Society, 2003. **150**(10): p. A1385-A1389.

174. Wong, D.H.C., et al., *Nonflammable perfluoropolyether-based electrolytes for lithium batteries.* Proceedings of the National Academy of Sciences, 2014. **111**(9): p. 3327-3331.

175. Edström, K., T. Gustafsson, and J.O. Thomas, *The cathode–electrolyte interface in the Li-ion battery.* Electrochimica Acta, 2004. **50**(2): p. 397-403.

176. Xu, C., et al., *Interface layer formation in solid polymer electrolyte lithium batteries: an XPS study.* Journal of Materials Chemistry A, 2014. **2**(20): p. 7256-7264.

177. Brochard-Wyart, F., C. Gay, and P.G. de Gennes, *Slippage of Polymer Melts on Grafted Surfaces.* Macromolecules, 1996. **29**(1): p. 377-382.

178. Mhetar, V. and L.A. Archer, *Slip in Entangled Polymer Melts. 1. General Features.* Macromolecules, 1998. **31**(24): p. 8607-8616.

179. Mhetar, V. and L.A. Archer, *Slip in Entangled Polymer Melts. 2. Effect of Surface Treatment.* Macromolecules, 1998. **31**(24): p. 8617-8622.

180. Barnes, H.A., *A review of the slip (wall depletion) of polymer solutions, emulsions and particle suspensions in viscometers: its cause, character, and cure.* Journal of Non-Newtonian Fluid Mechanics, 1995. **56**(3): p. 221-251.